CHARACTERIZATION OF THE VITREORETINAL INTERFACE AND VITREOUS IN THE PORCINE EYE AS IT CHANGES WITH AGE

by

Patrick Ryan Moran

A thesis submitted to the faculty of
The University of Utah
in partial fulfillment of the requirements for the degree of

Master of Science

Department of Mechanical Engineering

The University of Utah

December 2012

The University of Utah Graduate School

STATEMENT OF THESIS APPROVAL

The thesis of **Patrick Moran**

has been approved by the following supervisory committee members:

Brittany Coats	, Chair	**05/24/2012** Date Approved
Bart Raeymaekers	, Member	**05/24/2012** Date Approved
Kenneth L. DeVries	, Member	**05/24/2012** Date Approved

and by **Timothy Ameel** , Chair of

the Department of **Mechanical Engineering**

and by Charles A. Wight, Dean of The Graduate School.

ABSTRACT

Cases of child abuse, specifically abusive head trauma (AHT) or shaken-baby syndrome (SBS), have long been associated clinically with retinal hemorrhages (RH). Previous research has shown that the vast majority (~85%) of AHT cases present with some type of RH. Traumatic RH is initiated by an external application of forces and accelerations to the head, but the mechanism by which this causes RH in infants is still unknown. The most prominent theory suggests that collagen-mediated adhesion between the vitreous and retina causes traction on the retina during rapid head rotation, damaging retinal blood vessels. To date, this theory has never been proven.

In order to better understand the mechanisms of traumatic RH in infants, age-related changes of the vitreous and vitreoretinal interface were investigated. First, dynamic shear tests were conducted using a novel rheological interconversion technique to characterize the changes in material properties with developmental age of porcine vitreous. Next, scanning electron microscopy (SEM) and energy dispersive X-Ray spectroscopy (EDS) studies were performed on specimens from the vitreoretinal interface to quantitatively evaluate changes in collagen with age and in different regions of the eye.

In dynamic shear, there was a statistically significant difference among the three age groups at varying shear rates (frequencies) for both storage (G') and loss (G'') shear modulus. In particular, younger porcine vitreous had significantly higher (G') and (G'') than vitreous from older animals. Given the unavoidable time degradation of vitreous,

the interconversion technique used to characterize the porcine vitreous dynamic properties provided more reliable data over a wider range of frequencies (0.01 Hz - 1 Hz) than previous studies.

SEM image analysis of the vitreoretinal interface resulted in a significantly higher percent collagen in eyes from 3- to 5-day-old piglets compared to 4-week-old piglets ($p=0.002$). Statistically significant regional differences were hindered by large variances due to charging artifacts and extraneous collagen from the vitreous body. The EDS analysis resulted in significant differences in carbon ($p=0.009$), nitrogen ($p=0.025$), silicon ($p\leq0.001$), and sulfur ($p=0.007$) with respect to age. Regional significant differences were also found for sulfur ($p=0.002$).

TABLE OF CONTENTS

LIST OF FIGURES

LIST OF TABLES

ACKNOWLEDGEMENTS

I owe a huge debt of gratitude to my advisor, Dr. Brittany Coats, for her academic and career guidance over the past two years. She has been a great mentor and friend, and I am forever grateful for her diligent work and positive attitude not to mention her phenomenal editing skills. I also want to thank my Injury Biomechanics lab members for the many hours of hard work and fond memories. Also, I would like to acknowledge the Micron Microscopy Core Facilities, HSC Core Research Facilities, and Dixon Laser Institute for their guidance and technical expertise.

To my parents, thank you for the many years of love and support you have shown me throughout my academic career. I only hope that you are as proud of me as I am blessed to have such wonderful role models. Finally, I would like to dedicate this thesis in loving memory of my grandfather, Col. Elwood Mathison.

INTRODUCTION

Abusive Head Trauma (AHT) is one of the leading causes of child abuse related fatalities in the United States [6]. Patients may present with a wide range of symptoms making diagnosing AHT very challenging for clinicians. AHT cases have a high incidence of eye and brain injury, but it is unclear what types of accidental scenarios in children also result in similar injuries. Differences between accidental and inflicted trauma could be better identified if the mechanisms of each injury were known.

One injury in particular, retinal hemorrhage, is common in AHT and has also been reported in accidental trauma [1]. While it is generally understood that large angular accelerations of the head can lead to RH, the mechanisms are unknown. One prominent theory is that during head rotation, the vitreous pulls on the retina in regions of the eye with strong vitreoretinal adhesion and causes damage to the retinal vessels. The adhesion between the vitreous and retina is thought to be mediated by collagen fibers spanning the vitreoretinal interface. To better understand the potential mechanisms of RH, and expand our understanding of the biomechanics of the pediatric eye, we investigated the age dependent changes in vitreous material properties as well as the associated structural changes in collagen content at the vitreoretinal interface.

Rheological studies have demonstrated that the material properties of vitreous vary between species [7] and region [8]; however, no studies have quantified how the vitreous properties change with age. Similarly, the amount of collagen in the vitreous

and at the vitreoretinal interface has never been quantified to identify changes with age or region [9] [10] [11]. To fill these gaps in the literature, dynamic shear moduli of vitreous were calculated at various stages of early development using an advanced rheological technique known as interconversion. Scanning electron microscopy (SEM) was then used to analyze the vitreoretinal interface, specifically the quantity of collagen fibers. Due to the limited availability of human eyes for testing, we decided to refine our techniques and initiate the analysis using formalin fixed pig eyes. Pig eyes have similar anatomical characteristics such as a multilayered retina, well-defined vascular arcade, and a vessel-free zone similar to the human macula [12]. Additionally, changes in pig collagen content in vitreous and at the vitreoretinal interface with age appear to parallel human changes with age [10]. Eyes from three age groups were selected for analysis based on their relative brain development to humans: 5-day-old (infant), 4-week-old (toddler), and 2-month-old (adolescent).

CHAPTER 1

AGE DEPENDENT MATERIAL PROPERTIES OF PORCINE VITREOUS

1.1 Abstract

It has been shown that vitreous material properties significantly affect finite element modeling predictions of retinal stress during repetitive head rotation in infants [1]. However, no material property data for pediatric vitreous exists. Therefore, we sought to identify the age-dependent material properties of porcine vitreous during dynamic oscillatory (shear) loading. As with most biological tissues, the pediatric vitreous exhibited a viscoelastic material response which was characterized by a storage modulus (G′) and loss modulus (G″) representing the elastic and viscous behavior, respectively. These moduli were extremely difficult to characterize at high shear rates due to inertial effects, so an advanced rheological interconversion technique was used to extract high frequency moduli from creep data. Verification of the technique was performed with synthetic materials that span the viscous and elastic behavior spectrum. The technique was then used to characterize the dynamic material properties of vitreous in 3- to 5-day, 4-week, and 2-month-old porcine eyes. The interconversion technique resulted in a good approximation of G' for all materials, but the accuracy of G″ was reduced in materials with a predominantly elastic response ($\tan\delta << 1$). Storage and loss

modulus of vitreous from 5-day-old pigs were significantly greater than the moduli of vitreous from 2-month-old pigs. Significant differences were also found between the vitreous from 5-day and 4-week-old pigs, but only for two of the frequencies examined. Vitreous from 4-week and 2-month-old pigs also had significant differences in the storage and loss modulus, but only over some frequencies. The age dependent changes in material properties of porcine vitreous validate the need for future rheological studies on the material properties of human infant eyes to determine if the biomechanical changes in the pediatric eye contribute to the presence of retinal hemorrhages caused by AHT.

1.2 Introduction

Vitreous is a transparent gel-like substance located between the retina and lens in the eye. It is composed of a heterogeneous network consisting of 99 wt% water, 0.9 wt% salts, 0.1 wt% heterotypic collagen fibrils (collagen type II,V/XI and IX), and a hyaluronan network [5]. Characterizing the viscoelastic moduli of such a complex fluid with oscillation testing is a significant rheological challenge as it is susceptible to low signal-to-noise ratios at low frequencies, resonant effects, and tool inertial effects at the higher frequencies (1-10Hz). To overcome these obstacles and obtain data over a spectrum of clinically relevant frequencies, we converted time-dependent (TD) data from creep testing to estimate the frequency-dependent (FD) data typically measured with oscillation testing. A polystyrene-toluene solution (PS), agarose mixture, and Matrigel® were selected to verify the interconversion technique because their viscous and elastic characteristics encapsulate the viscoelastic response of vitreous. Once verified, the interconversion technique was applied to porcine vitreous at different stages of

development (5-day, 4-week, and 2-months old) to identify the age-dependent viscoelastic response of vitreous.

1.3 Methods and Materials

To identify the frequency dependent response of vitreous, time domain data from creep tests were converted to frequency domain using a specialized spectral conversion technique (described in detail in section 3.1). To validate this technique we tested three synthetic materials (PS, agarose, and Matrigel) in creep and dynamic oscillation to compare the dynamic moduli from both methods. The rheological characterization was conducted by dynamic shear tests on the samples using an AR-G2 rheometer (TA Instruments, New Castle, DE).

1.3.1 *Polystyrene-Toluene Solution (PS)*

Polystyrene atactic flakes (Polysciences, Inc., Warrington, PA) with a molecular weight of 50,000 Da were dissolved in Toluene to a final concentration of approximately 60% by mass. Small volumes ($0.6cm^3$-$2.5cm^3$) of the solution were placed on the rheometer plates and maintained at a temperature of 20° C for testing.

1.3.2 Agarose

Dry agarose (Sigma-Aldrich, St. Louis, MO) was mixed with deionized water to a concentration of 1% by volume. After thoroughly mixing, the agarose was heated in the microwave until it began to boil. The mixture was stirred a second time and poured into a Petri dish, covered, and immediately cooled in a fridge at 9°C for at least 12 hours to

gel completely. Using a 20 mm trephine, agarose samples were delicately removed from the Petri dish and placed on the rheometer parallel plates maintained at 20°C for testing.

1.3.3 Matrigel

Matrigel (BD Biosciences, Bedford, MA) is a basement membrane matrix primarily composed of laminin and collagen type IV. Matrigel is stored frozen between -10°C and -20°C. Heating it to ~4°C liquefies the Matrigel. Increasing the temperature to 22-35°C will initiate cross-linking and result in a semisolid gel. For this analysis, Matrigel was initially thawed and liquefied by placing it on ice in a refrigerator and maintaining a temperature range of 2-6° C for 24 hours. Once liquid, the Matrigel (100% concentration) was divided into 0.25 mL aliquots and refrozen until testing. Extra care was taken during the aliquot process to ensure that nothing above 10° C came into contact with the Matrigel as this could cause premature gelation. To create uniformly sized gel samples for rheometry testing, a steel washer (thickness=2mm, ID=13.7mm) was used as a mold. The washer was placed on the rheometer plates preset to a temperature of 8°C. Dow Corning high vacuum grease (Auburn, MI) was used on the underside of the washer to prevent leaking. Aliquotted Matrigel samples were re-thawed by placing on ice in the refrigerator for 24 hours. Once liquid, the Matrigel was transferred (0.15 mL to 0.25 mL) into the center of the washer using a 200 μL pipeteman (VWRbrand, Radnor, PA) with a chilled pipette tip. The temperature of the rheometer plates was increased to 37.5°C to initiate gel formation and then held constant for 30 minutes. Once completely gelled, the washer was carefully lifted off of the parallel plates leaving the cylindrical Matrigel specimen intact. Testing was performed at 37.5°C.

1.3.4 Synthetic Material Mechanical Testing

To characterize the dynamic material properties using oscillation testing methods and the interconversion technique, each sample (n=6 for each material) was subjected to the following tests: dynamic strain sweep, dynamic frequency sweep (forced oscillation), and creep-recovery. The order of the frequency and creep testing was rotated (i.e. frequency/creep, creep/frequency) from one sample to the next to account for carryover effects due to the dependent testing. Strains sweeps were performed over three decades (0.1-100% strain) at 1 Hz to establish the linear viscoelastic region (LVR). Forced oscillations were swept over three decades from 0.1-100 radians per second with a 1% (PS, agarose) or 20% (Matrigel) strain amplitude that was previously found to lie within in the LVR of these materials. For creep testing, PS, agarose, and Matrigel were subjected to a torque of 35 μNm, 15 μNm, and 5 μNm, respectively, and held for 90 seconds. The stresses resulting from these torques were found to lie in the LVR for each material.

Early in testing it became apparent that the forced oscillation tests were susceptible to slipping at the boundary of the parallel plates and the sample. To eliminate these effects, commercial cross-hatched parallel plate geometries (C1) and in-house custom parallel plate geometries (C2, C3) were designed to better grip the samples during testing (Fig. 1). Development and verification of the custom parallel plate geometries can be found in Appendix A. PS and agarose testing were completed using the C1 geometry; Matrigel testing was performed using the C3 geometry for the top plate and the C1 geometry for the bottom plate.

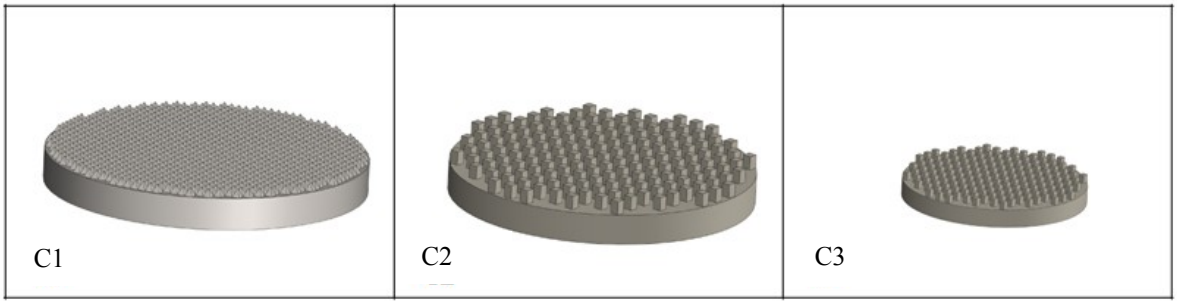

Figure 1: Various plate geometries were used to reduce wall slip between sample and rheometer. C1) Cleat geometry sold commercially by TA Instruments: 90o x 0.5mm deep, apex to apex, steel. C2) Custom built geometry for large samples: 0.6mm x0.6mm x0.9mm (LxWxH) 20 mm and 24 mm diameter ABS. C3) Custom built geometry for small samples; 0.6mm x0.6mm x0.9mm (LxWxH) 13.70mm diameter ABS.

1.3.5 Porcine Vitreous Preparation and Testing

Eyes from 3-to 5-day-old (n=8), 4-week-old (n=8) and 2-month-old (n=6) old pigs were fixed in 10% formalin at the conclusion of nonocular related animal studies and transferred to phosphate buffered saline (PBS) for storage until testing. On the date of testing, the extraocular tissue (muscle, fat, etc.) was removed using forceps, and the optic nerve was transected at the sclera and optic nerve junction to allow direct access to the peripapillary sclera. The sclera and choroid were dissected up to the corneoscleral junction by accessing the small cavity between the choroid and retina and bluntly dissecting with forceps. The retina was then carefully peeled away from the vitreous leaving only the vitreous and hyaloid membrane. The entire vitreous and hyaloid membrane was placed onto the C2 custom rheometer plates maintained at 37.5°C. A solvent trap covered the specimen to maintain a humid environment.

Two vitreous samples (5-day-old and 4-week-old) were subjected to a time sweep for 12 minutes at 0.1 Hz and 1% strain to identify how the dynamic shear moduli change

with time. Three additional samples (5-day, 4-week, and 2-month) were subjected to a strain sweep over three decades (0.1-100% strain) at 0.1 Hz to identify the linear viscoelastic region of vitreous. The remaining 17 samples (3-to 5-day, n=6; 4-week, n=6; 2-month, n=5) underwent creep testing (0.25 □Nm torque) to determine their shear moduli using the interconversion technique.

1.4 Data Analysis

1.4.1 Interconversion Technique

All creep tests were converted post hoc to FD data using a previously developed interconversion technique [13] composed of three steps. First, TD creep data are fit to an intermediate material function known as the retardation spectrum (Fig.2). This retardation spectrum is then interconverted to another material function, the relaxation spectrum. Finally, the relaxation spectrum is used to produce FD oscillation data. This final step requires an input of the frequency range over which to convert the creep data. The lower limit of the converted frequency data must correspond to the reciprocal of the total time for the creep data. For example, one creep test ran for 100 seconds, so the lower limit of the frequency range input for our data was 0.01 Hz or 0.1 rad/s. Similarly, the upper limit of the converted frequency data must correspond to the reciprocal of the lowest value resolvable from the creep tests. This value can vary depending on the material response, the sensitivity of the load cell, and the presence and duration of a toe region. The three-step interconversion process was performed using the *Advanced Polymer Library* software (TA Instruments, New Castle, DE). A more in depth description of interconversion theory is provided in Appendix B.

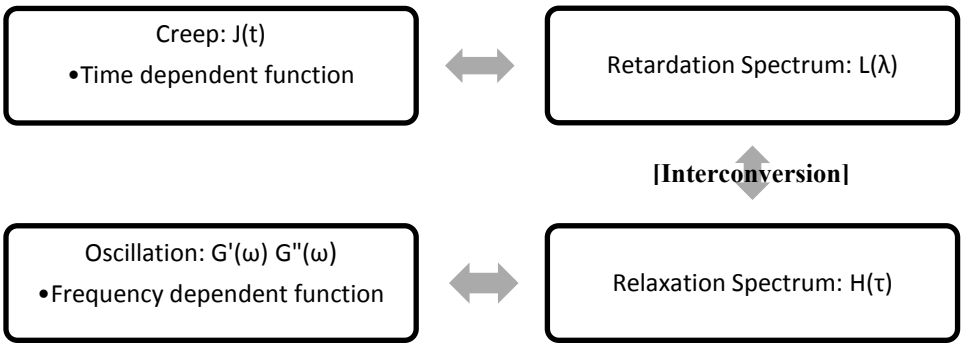

Figure 2: Interconversion technique used to calculate frequency dependent material properties of vitreous from creep testing.

Creep ringing is a phenomenon that results from the coupling of the sample's inertia with the rheometer's inertia [14] and has an appearance of an under-damped system. Interconversion of data with creep ringing can cause large amounts of error. In order to remove this potential error, an averaging technique was developed using MATLAB (Mathworks, Inc. v. 7.9.0) in which the ringing was damped by averaging the peak-to-valley distances. All the peak and valley data points were selected for averaging with the origin included as a valley. By averaging the peak-to-valley data, the system was effectively critically damped and noise was removed from the system.

1.4.2 Statistics

Statistical analysis was performed on PS, Matrigel, and agarose using SPSS PASW 18 (IBM, Armonk, NY). Paired samples t-test (α=0.05) was used at each frequency of the interconverted spectrum to test for significant differences between G′ and G″ obtained from forced oscillation versus G′ and G″ calculated from interconverted

creep test data. The interconverted frequency spectrum was defined by the upper and lower frequency limits input during step 3 of the interconversion process.

Material property differences among porcine vitreous at different ages (section 3.1) were analyzed using a univariate one-way ANOVA test. The null hypothesis (H0) statement was as follows: $\mu_{5day} = \mu_{4week} = \mu_{2months}$ for both G′ and G″. The alternative hypothesis (HA) was: $\mu_{5day} \neq \mu_{4week} \neq \mu_{2months}$ for both G′ and G″. A 95% confidence interval (α=0.05) was used and independence was assumed since only the interconverted data was used in the age comparison.

1.5 Results

1.5.1 Polystyrene-Toluene Solution

The dynamic moduli of polystyrene-toluene solution were initially difficult to calculate due to memory effects. This was corrected by preconditioning the PS with a single oscillation test and creep test prior to collecting data for analysis. The creep test of the predominantly viscous PS solution resulted in little to no creep ringing (Fig. 3). Therefore, the interconversion of this data was completed without averaging any data points. The paired t-tests indicated that only the last two frequencies of G′ and last frequency of G″ calculated from the creep data were statistically different from G′ and G″ calculated from oscillation data. The deviations at these higher frequencies were most likely caused by the presence of a slight toe region and some minor noise in the PS creep data for the first ~0.1 seconds. Therefore, interconversion was identified as a valid method of analysis for PS up to approximately 10 Hz (Fig. 4-5).

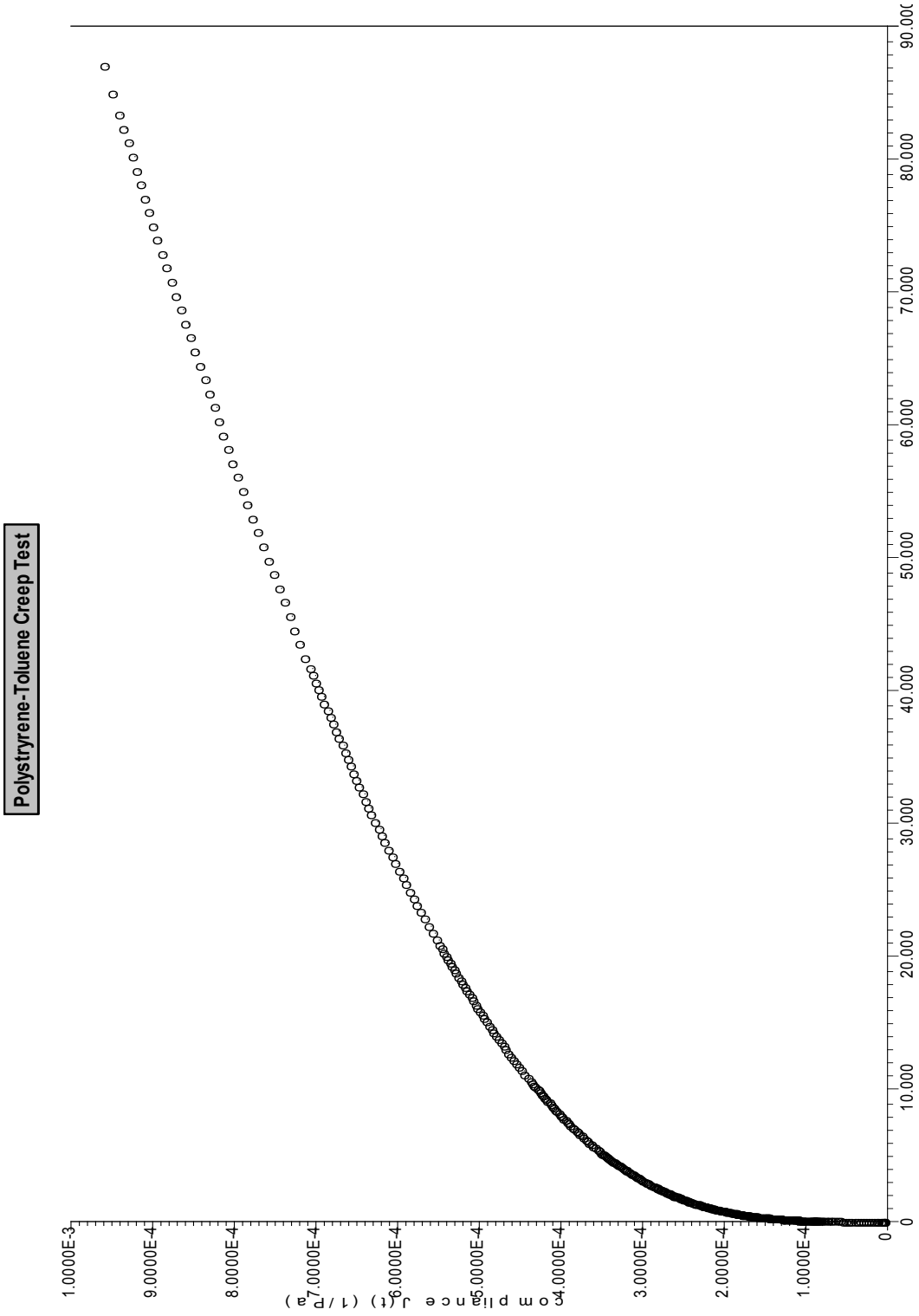

Figure 3: Representative creep compliance curve for polystyrene-toluene

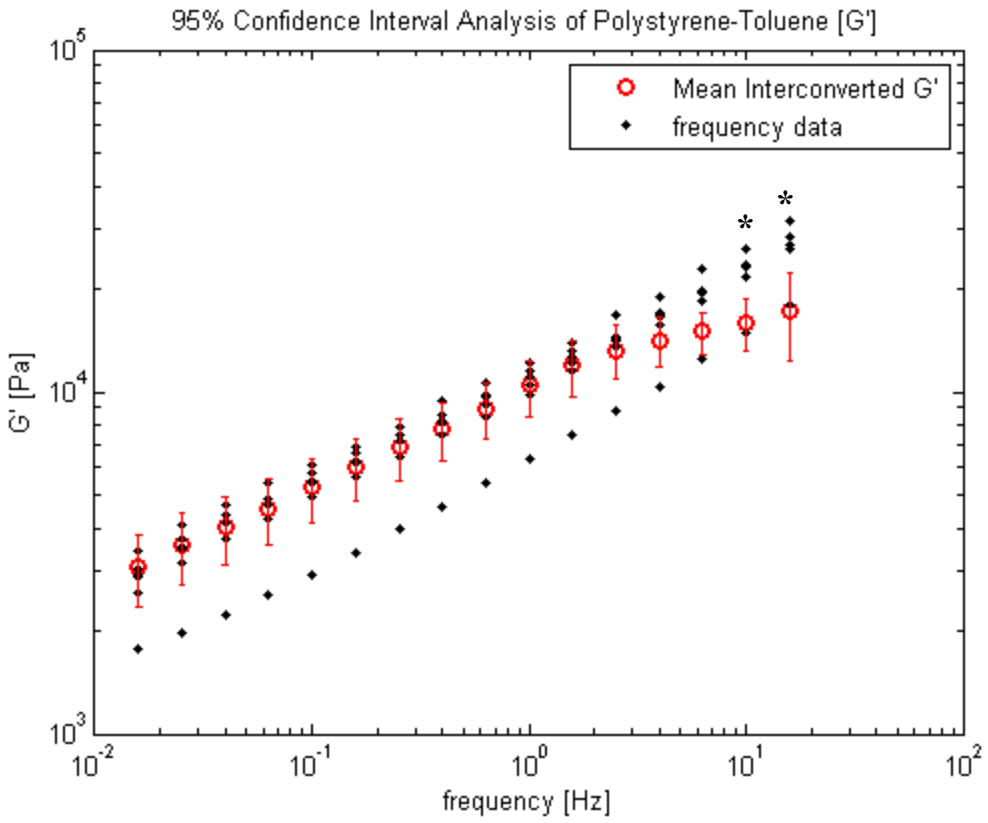

Figure 4: Verification of the interconverted storage modulus for polystyrene solution. The interconverted G′ PS data were not statistically different from the oscillation G′ data up to 10 Hz frequency range (*p<0.05).

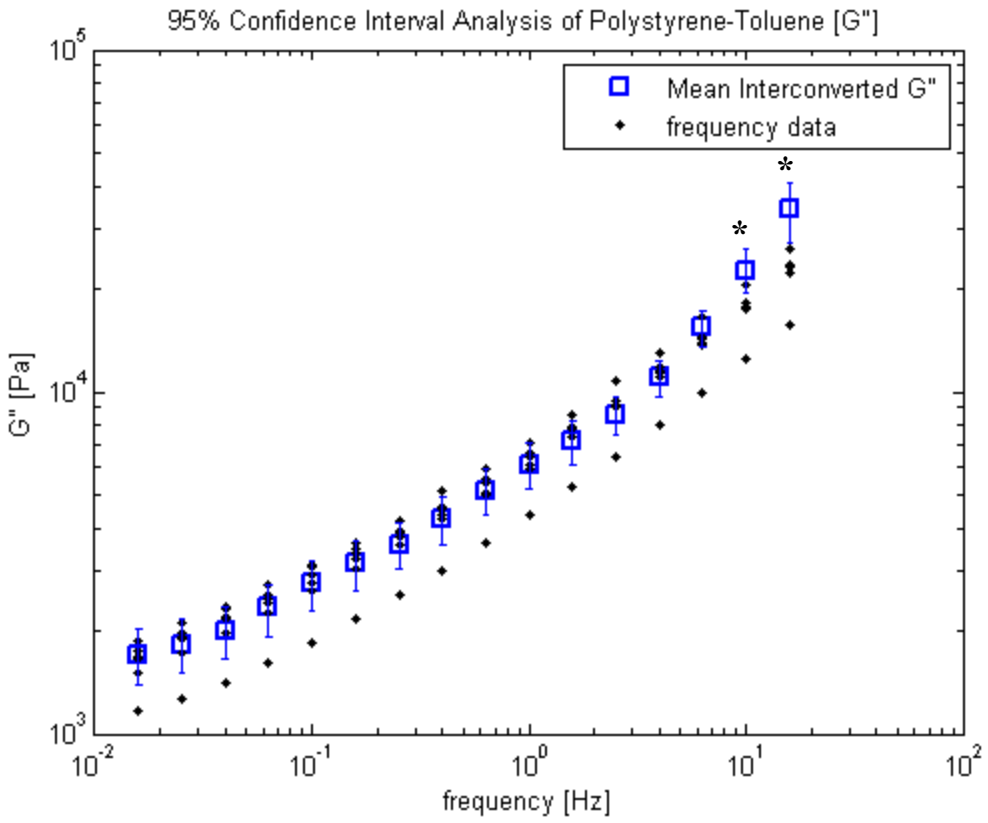

Figure 5: Verification of the interconverted loss modulus for polystyrene solution. The interconverted G″ data became significantly different from the oscillation G″ data around 10 Hz (*p<0.05).

1.5.2 Agarose

Performing a creep test on this elastic dominant material resulted in significant free oscillations (e.g., creep-ringing) for the initial 5 to 7 seconds of the test (Fig. 6). The ringing was eliminated by using the averaging technique described earlier. The interconversion technique resulted in a good approximation of G′ for the entire interconverted frequency spectrum (Fig. 7), but the interconverted G″ showed less agreement with the oscillation data (Fig. 8). Specifically, the interconverted G″ was significantly different from the oscillation G″ between 0.04 – 0.63 Hz (Fig. 8). The

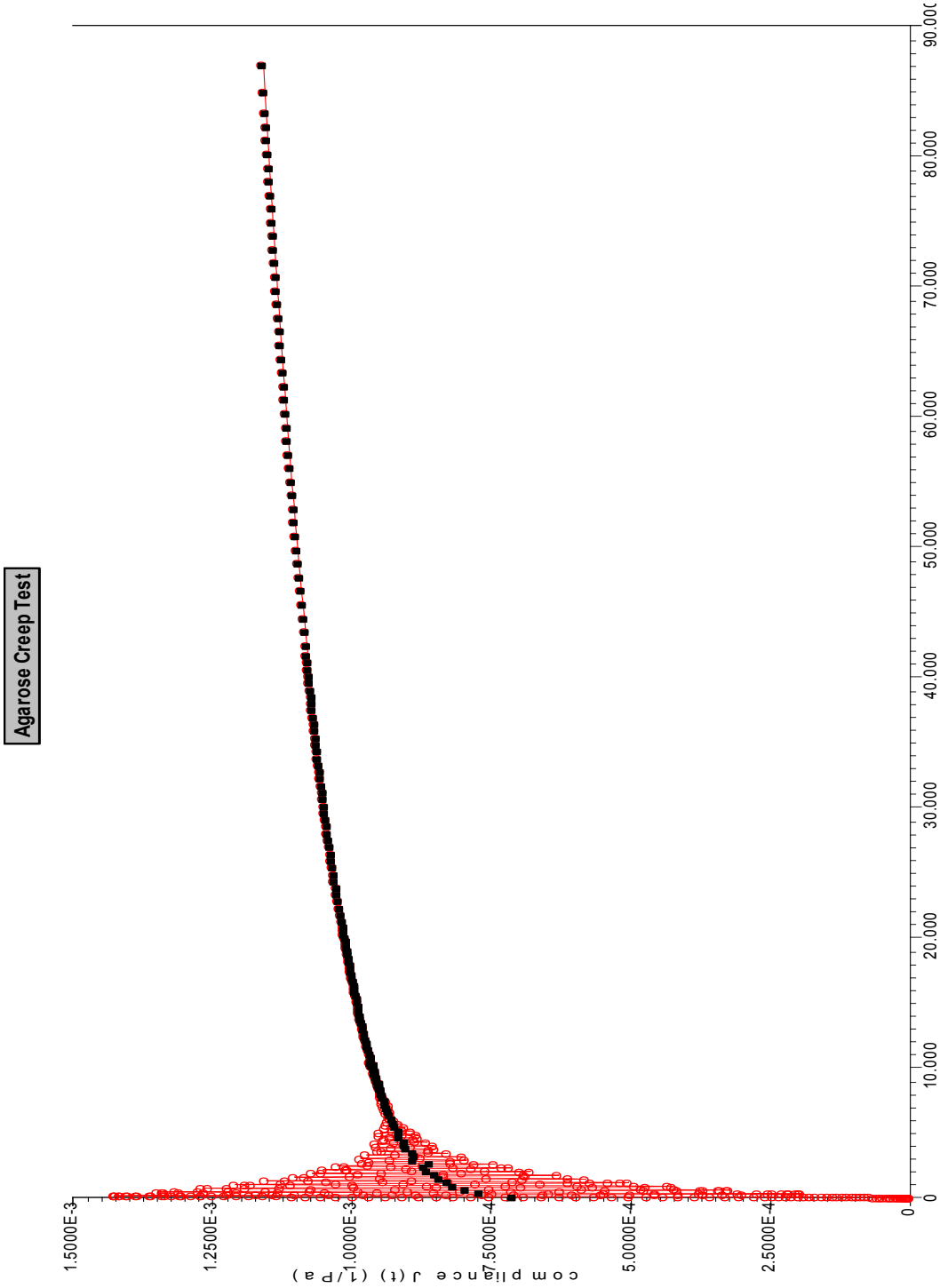

Figure 6: Representative creep compliance curve for Agarose (○). Averaging this original creep-ringing region resulted in a damped compliance curve (■).

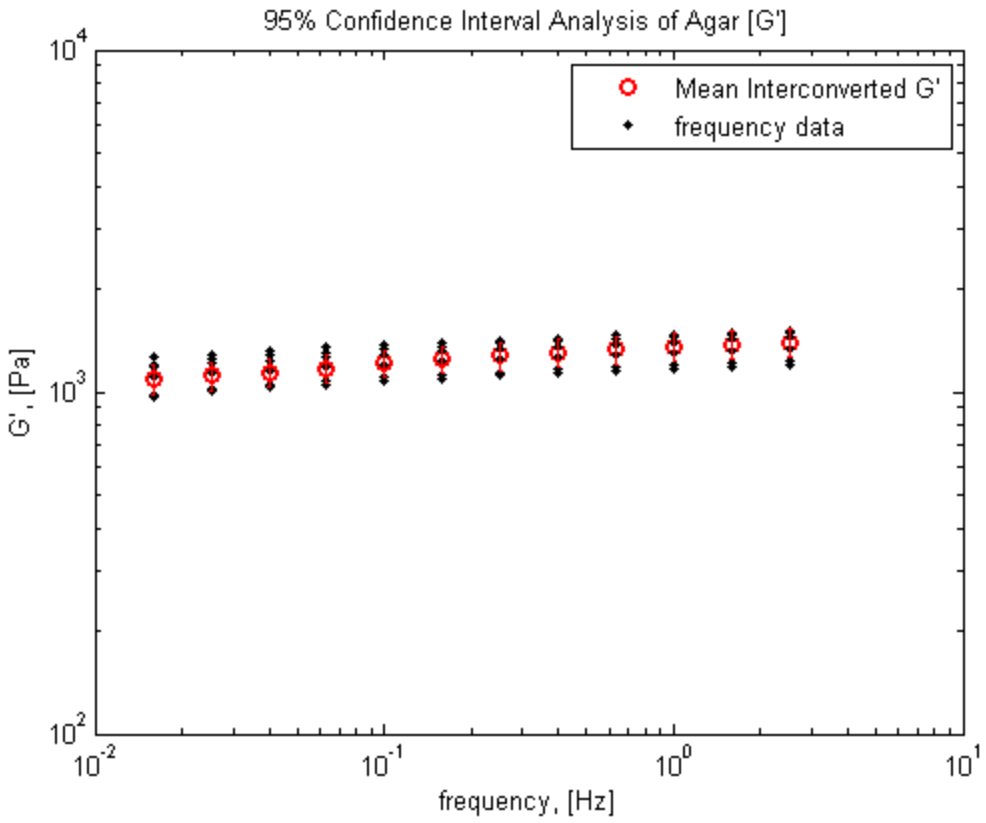

Figure 7: Verification of the interconverted storage modulus for agarose. The interconverted G′ was not statistically different from the oscillation G′ data over the entire interconverted frequency spectrum.

maximum error was 38.5% at 0.1Hz. The minimum error was 4% at 1.6Hz as seen in Table 1.

1.5.3 Matrigel

The Matrigel samples demonstrated ringing effects for the longest duration (approx. 20 to 40 seconds) during the creep tests (Fig. 9). These effects were removed by using the aforementioned averaging technique. As shown in Fig. 10, the interconversion technique resulted in nearly identical G′ values for the entire interconverted frequency

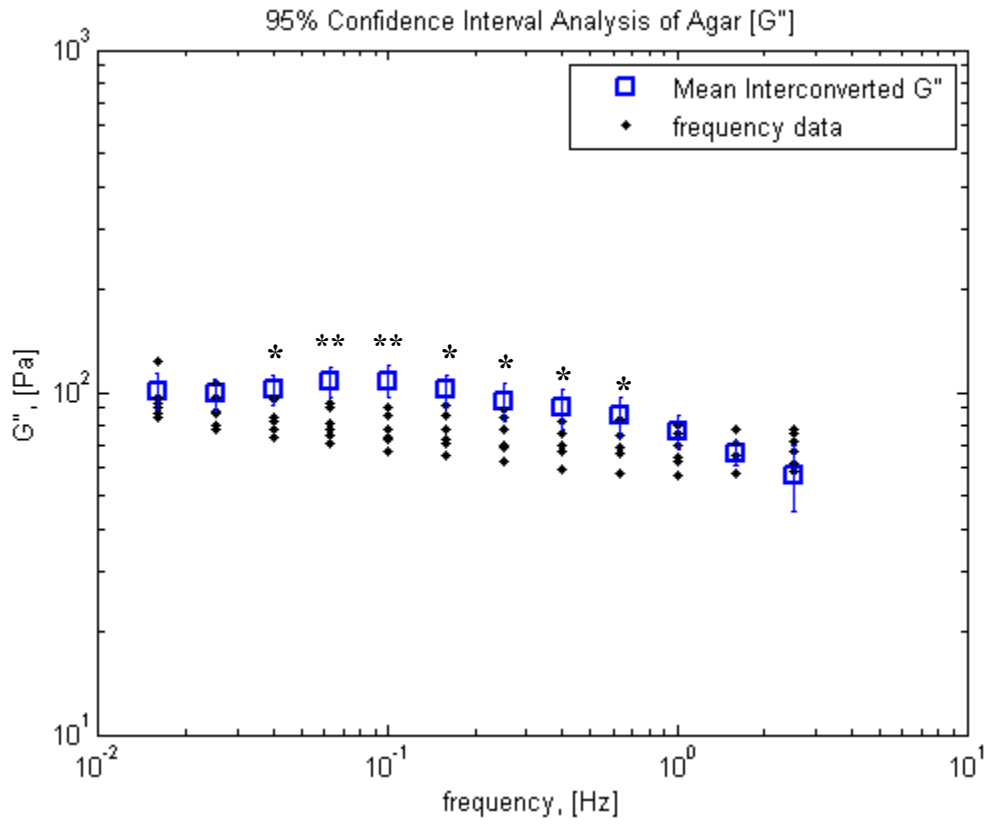

Figure 8: Verification of the interconverted loss modulus for agarose. Compared to the G″ from forced oscillation tests, the interconverted G″ was statistically different for seven of the 12 frequencies in the interconverted frequency spectrum (*p<0.05, **p<0.005).

spectrum. The interconverted G″, however, was only valid to about 0.1 Hz (Fig. 11). The maximum error (194%) occurred at the endpoint of the interconverted frequency spectrum. Both agarose and Matrigel had limited high frequency ranges due to tool inertial effects. This occurred around 4 Hz for agarose and 0.5 Hz for Matrigel. The interconverted data were able to extend the reliable frequency range for G′ of agarose and Matrigel to 13 Hz and 2 Hz, respectively (Table 2).

Table 1: Agarose statistical p-values comparing shear moduli that correspond to the G′ and G″ plots above.

Frequency (Hz)												
2.5	*1.6*	*1*	*0.63*	*0.4*	*0.25*	*0.16*	*0.1*	*0.063*	*0.04*	*0.025*	*0.015*	
p=.683	p=.626	p=.649	p=.756	p=.852	p=.985	p=.906	p=.672	p=.449	p=.382	p=.424	p=.559	**G′**
p=.175	p=.594	p=.171	**p=.045**	**p=.023**	**p=.030**	**p=.010**	**p=.003**	**p=.004**	**p=.020**	p=.125	p=.437	**G″**

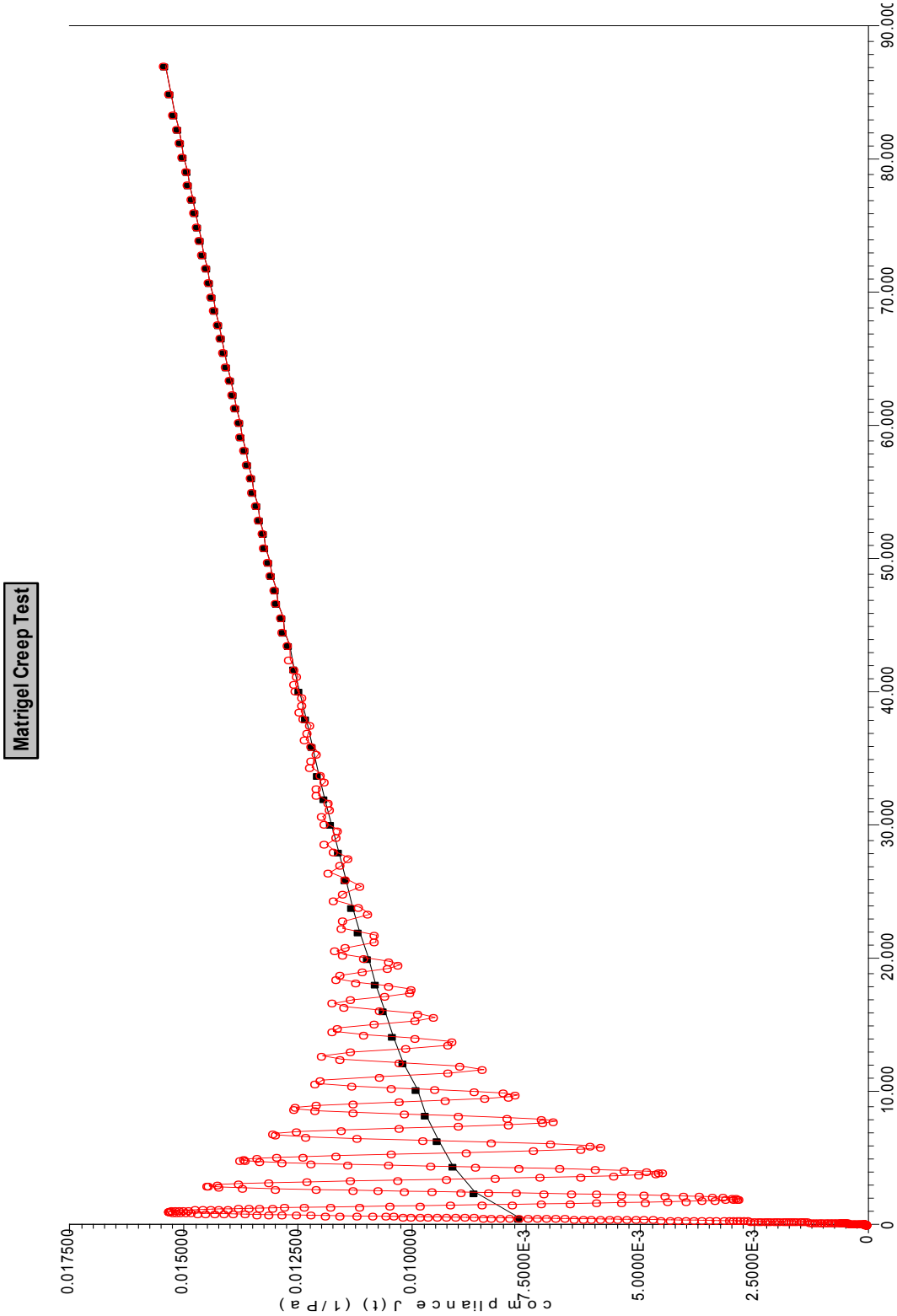

Figure 9: Representative creep compliance curve for Matrigel (○). Averaging this original creep-ringing region resulted in a damped compliance curve (■).

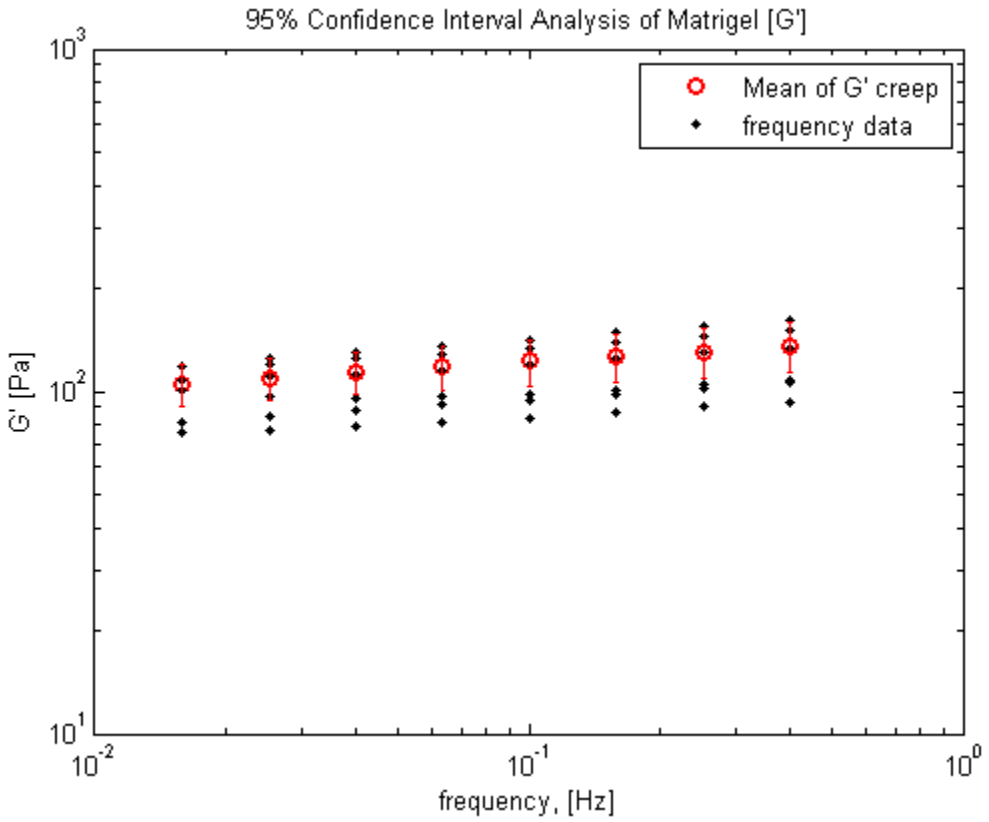

Figure 10: Verification of the interconverted storage modulus for Matrigel. The interconverted G′ was not statistically different from the forced oscillation G′ over the entire interconverted frequency spectrum.

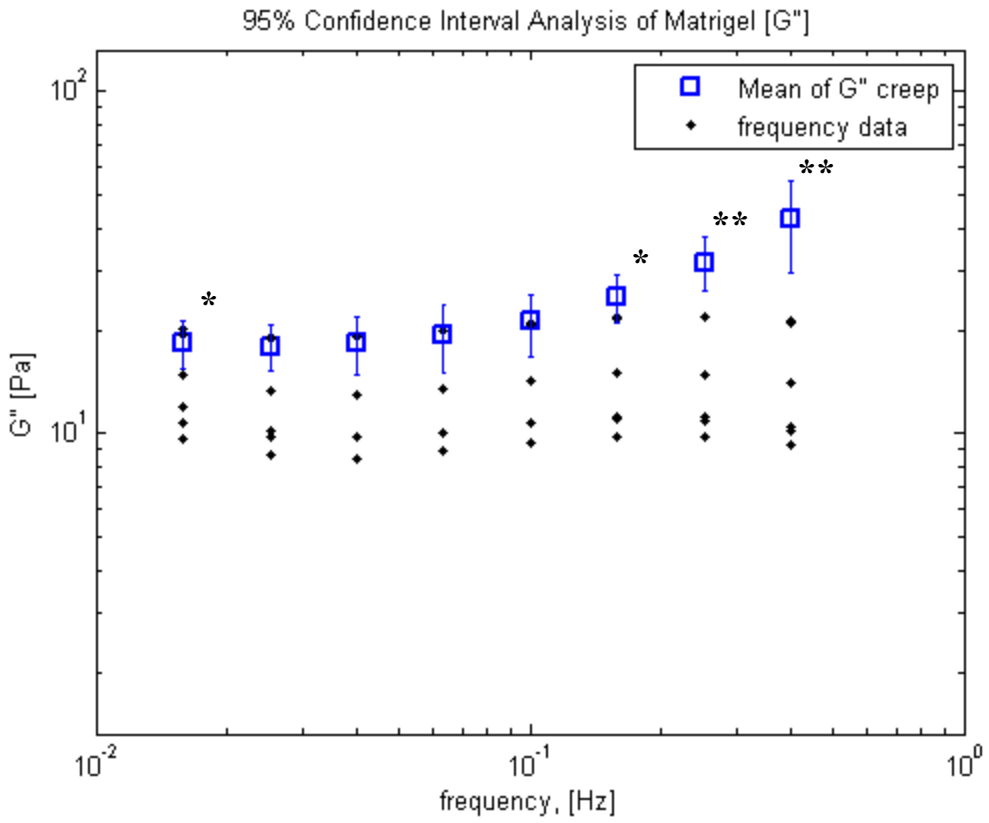

Figure 11: Verification of the interconverted loss modulus for Matrigel. Compared to the oscillation G″ data, the interconverted G″ was statistically different for four frequencies (*p<0.05, **p<0.005).

Table 2: Matrigel statistical p-values comparing shear moduli that correspond to the G′ and G″ plots above.

	Frequency (Hz)							
	0.015	*0.025*	*0.040*	*0.063*	*0.10*	*0.16*	*0.25*	*0.40*
G′	p=.410	p=.286	p=.234	p=.200	p=.117	p=.163	p=.158	p=.150
G″	**p=.039**	p=.118	p=.135	p=.102	p=.065	**p=.014**	**p=.002**	**p=.003**

1.5.4 Porcine Vitreous

The creep response of the porcine eyes appeared to be predominantly more viscous, similar to the PS, but creep ringing was observed for the initial ten seconds of the test at a relatively low ringing frequency (Fig. 12). The ringing was corrected using the same protocol used for agarose and Matrigel. Low ringing frequencies in the creep tests and a relatively long toe region restricted the resolvable upper limit of the interconverted frequency spectrum to 1 Hz. This was still better than our early forced oscillation tests of vitreous which had an upper limit of 0.3 Hz due to tool inertial effects. In general, storage and loss modulus calculated from the interconverted creep data decreased with age, but this was only significant between the 3- to 5-day-old eyes and the 2-month-old eyes. Further examination using a Games-Howell means comparison found significant differences with age across the entire frequency range for the storage modulus (G′) comparing 5-day-old vitreous to 2-month-old vitreous, but only one frequency (0.25 Hz) for the loss modulus (G″) was significantly different between the two ages. The storage modulus of the 5-day-old vitreous was significantly different from the 4-week-old porcine vitreous for only two frequencies. Loss modulus (G″) comparisons between the 5-day to 4-week-old porcine vitreous and 4-week to 2-month-old porcine vitreous were statistically significant for four and two frequencies, respectively (Table 3). Based on the earlier validation tests with synthetic materials, the evaluation of the interconversion likely resulted in more error for G″ values than G′.

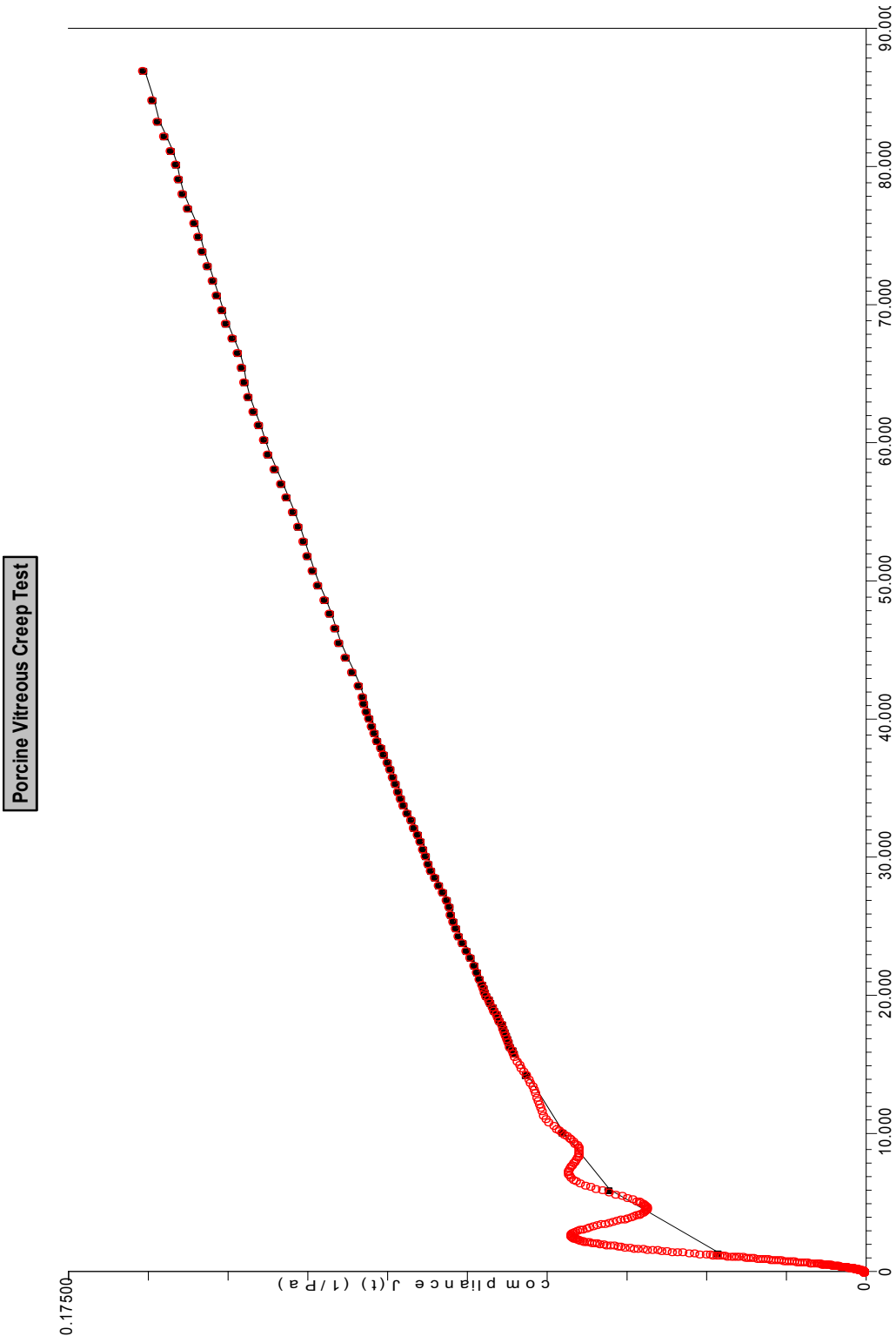

Figure 12: Representative porcine vitreous creep compliance curve (○). Averaging this original creep-ringing region resulted in a damped compliance curve (■).

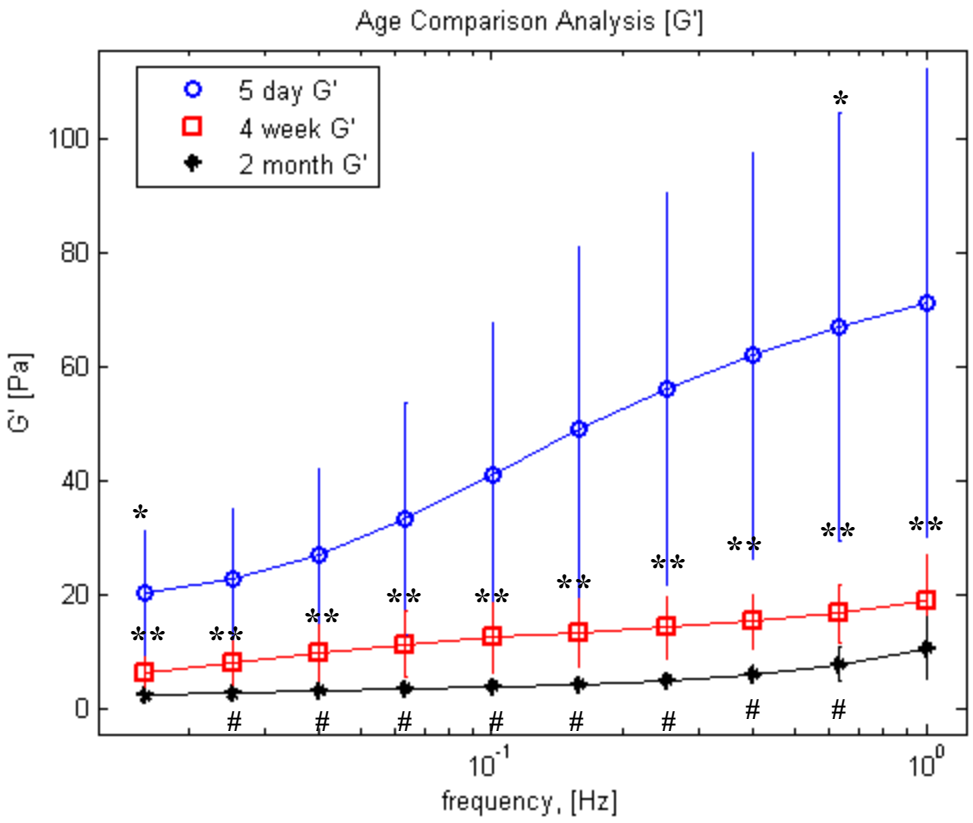

Figure 13: Mean ± SD of storage modulus of porcine vitreous at three stages of development. Statistical differences ($p<0.05$) between the 5-day-old porcine vitreous and 4-week-old porcine vitreous are indicated by (*). In comparison to the 2-month-old vitreous, the 5-day-old porcine vitreous was significantly different ($p<0.05$) at frequencies represented by (**) . The 4-week-old porcine vitreous was significantly different from the 2-month-old porcine vitreous ($p<0.05$) for nearly the entire frequency range (#).

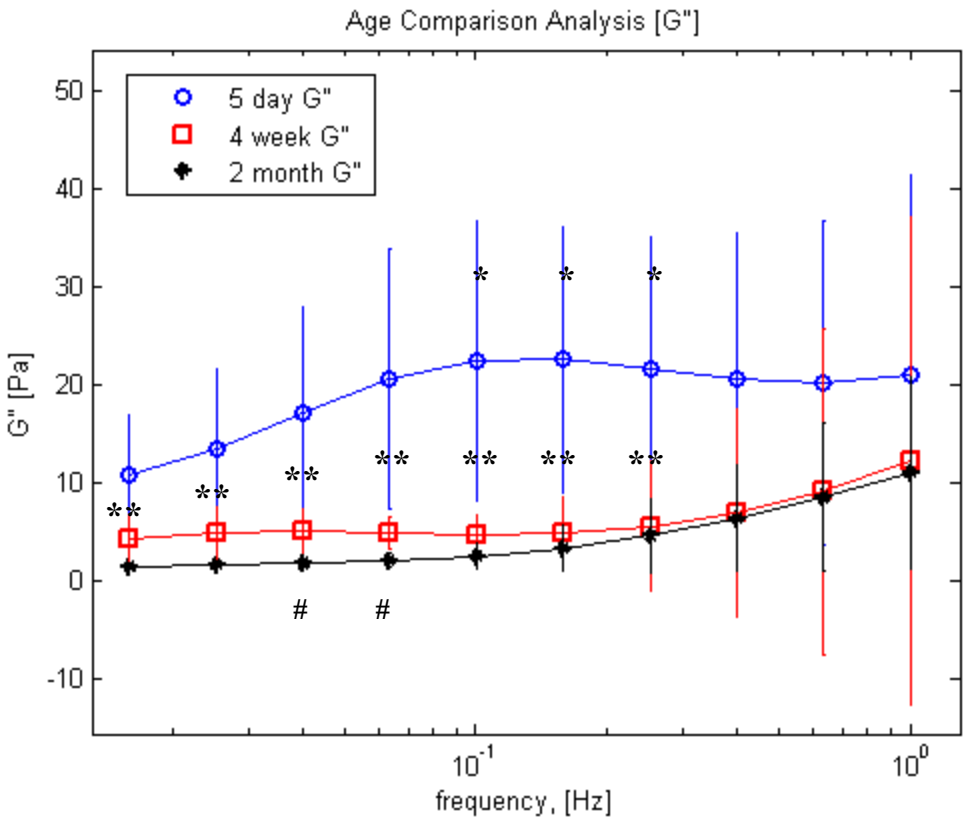

Figure 14: Age-dependent loss modulus of porcine vitreous. Statistical differences ($p<0.05$) between the 5-day-old and 4-week-old porcine vitreous are indicated by (*). In comparison to the 2-month-old vitreous, the 5-day-old porcine vitreous was significantly different ($p<0.05$) at frequencies represented by(**) . The 4-week-old porcine vitreous was not significantly different from the 2-month-old porcine vitreous ($p<0.05$) for nearly the entire frequency range (#).

Table 3: Significance level testing of G′ and G″ between age groups of porcine vitreous from 0.015 – 1.0 Hz.

		Frequency (Hz)									
Comparisons		*0.015*	*0.025*	*0.040*	*0.063*	*0.10*	*0.16*	*0.25*	*0.40*	*0.63*	*1.0*
5 dy vs. 4 wk	**G′**	**p=.010**	p=.071	p=.086	p=.099	p=.099	p=.086	p=.067	p=.052	**p=.048**	p=.057
	G″	p=.114	p=.108	p=.087	p=.073	**p=.008**	**p=.007**	**p=.023**	p=.212	p=.407	p=.731
5 dy vs. 2 mo	**G′**	**p=.002**	**p=.024**	**p=.028**	**p=.035**	**p=.041**	**p=.040**	**p=.034**	**p=.027**	**p=.026**	**p=.033**
	G″	**p=.030**	**p=.036**	**p=.039**	**p=.042**	**p=.005**	**p=.006**	**p=.022**	p=.146	p=.404	p=.691
4 wk vs. 2 mo	**G′**	p=.598	**p=.043**	**p=.050**	**p=.047**	**p=.039**	**p=.029**	**p=.019**	**p=.011**	**p=.016**	p=.154
	G″	p=.072	p=.063	**p=.038**	**p=.018**	p=.914	p=.956	p=.984	p=.992	p=.998	p=.994

1.6 Discussion

The results of this study show that the process of converting creep compliance TD data to FD data, G′ (ω) and G″ (ω), is successful but has some limitations. Viscous dominant materials, such as the PS solution, can be directly interconverted without any additional data analysis (e.g., averaging) and with good accuracy for predicting G′ and G″ up to 10 Hz. However, with elastic dominant materials, such as agarose and Matrigel, significant error can occur due to free oscillations (creep ringing). In fact, there appears to be a relationship between the accuracy of the interconversion method and the ratio of the viscous to elastic mechanical response of the material, tanδ (Fig. 15). Predictions of

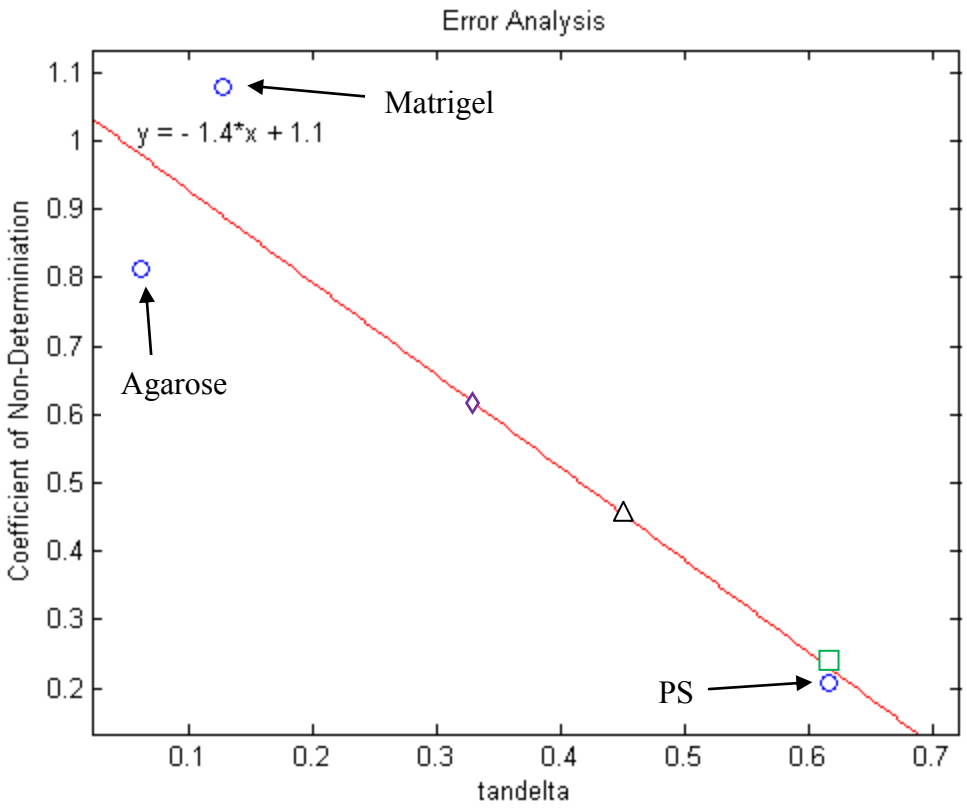

Figure 15: Analysis of the increased G" error associated with a lower tanδ value. The tanδ associated with the 3- to 5-day-old (◊ tanδ=0.33), 4-week-old (Δ tanδ=0.45), and 2-month-old (□ tanδ=0.62) corresponds to a coefficient of non-determination of 0.64, 0.47, and 0.23, respectively.

G″ for PS, which has an average tanδ of 0.61, were accurate over a wide range of frequencies (0.01Hz-10Hz). However, Matrigel and agarose, which have a much smaller tanδ (0.13 and 0.06, respectively) had significantly more error in the G″ data (Fig. 15). Creep ringing of the material is a significant contribution to error and our averaging technique may have been unable to eliminate it completely.[1] A low signal-to-noise ratio may also contribute to the problem. When G′ is larger than G″, the subdominant signal

[1] The averaging technique takes a single peak and average it with a single neighboring valley. Averaging each peak with the neighboring valley on each side of the peak would result in additional data points and could potentially improve the accuracy of the interconversion.

(e.g., G″) can be less accurate and may be noisy [15]. Both of these sources for error are predisposed to elastic materials, so the interconversion technique is much more accurate for predominantly viscous materials. Porcine vitreous has a tanδ more comparable to PS, but it changes with age (Fig. 15). We conclude that the interconverted G′ and G″ porcine data provides reliable results for frequencies up to 1Hz, but it is slightly more accurate in calculating G" in eyes from older children than for infants. Additional verification of the validity of this technique for the infant age group should be performed using materials with $\tan\delta \approx 0.3$.

The actual error in G″ when using the interconversion method on vitreous cannot be directly measured as it was with the synthetic materials due to continual water loss of vitreous during testing [4]. In a preliminary examination, we found that G′ and G″ values dropped 20%-60% depending on the age of the animal within 90 seconds after the start of testing. More variation occurred after 90 seconds. Each forced oscillation test took 390 seconds to complete a frequency sweep (0.1-100rad/s). This means that the properties of vitreous changed throughout the sweep and any subsequent creep testing on the same sample would be incomparable. Similarly, each creep test lasted 90 seconds and any subsequent oscillation testing was bound to result in different dynamic moduli. One benefit of the interconversion technique is that high frequency rate information is gleamed within the first second of testing. In this regard, using the interconversion technique on vitreous can result in much more accurate measurements of dynamic viscoelastic moduli at high frequencies. Post-hoc oscillation tests were conducted on 5-day-old vitreous (n=1) and 4-week-old vitreous (n=1) to compare the error between the two testing methods. The G′ values of the 5-day-old vitreous fell within the error bars

over the frequency spectrum where the oscillation testing is valid (Fig. 16). The 4-week-old vitreous oscillation data showed worse correlation (Fig. 17), but at both ages the G′ values were reduced for the oscillation test which is what we expect with longer test times. The G″ values for both the 5-day and 4-week-old porcine vitreous were similarly reduced for the oscillation testing (Fig. 18, 19). As expected from the tanδ analysis, the G″ for the younger age eye showed more error.

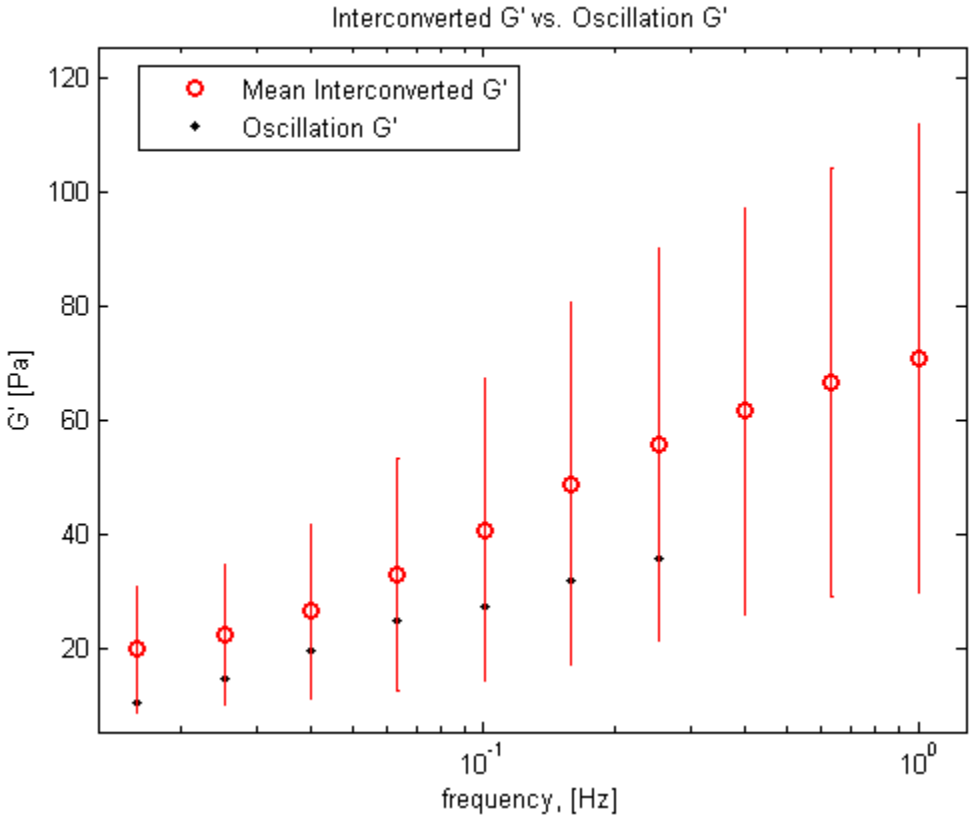

Figure 16: 5-day-old porcine vitreous comparison of the G' values calculated using the interconversion technique (○) versus using a frequency sweep (●).

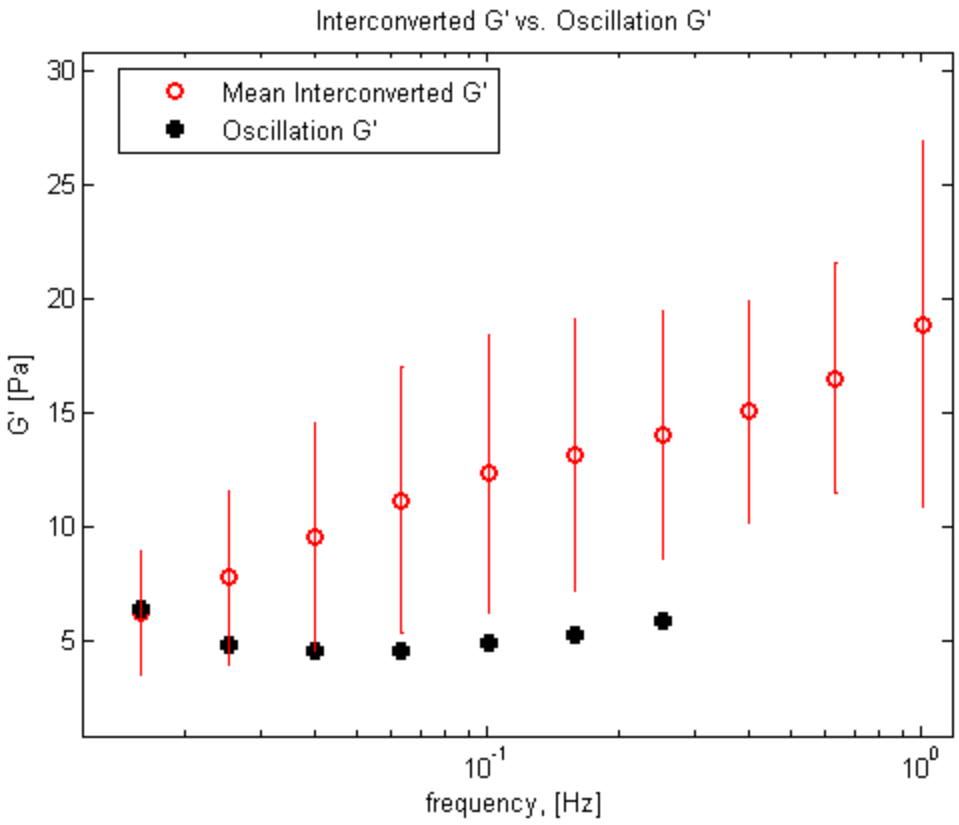

Figure 17: 4-week-old porcine vitreous comparison of the G' values calculated using the interconversion technique (○) versus using a frequency sweep (●).

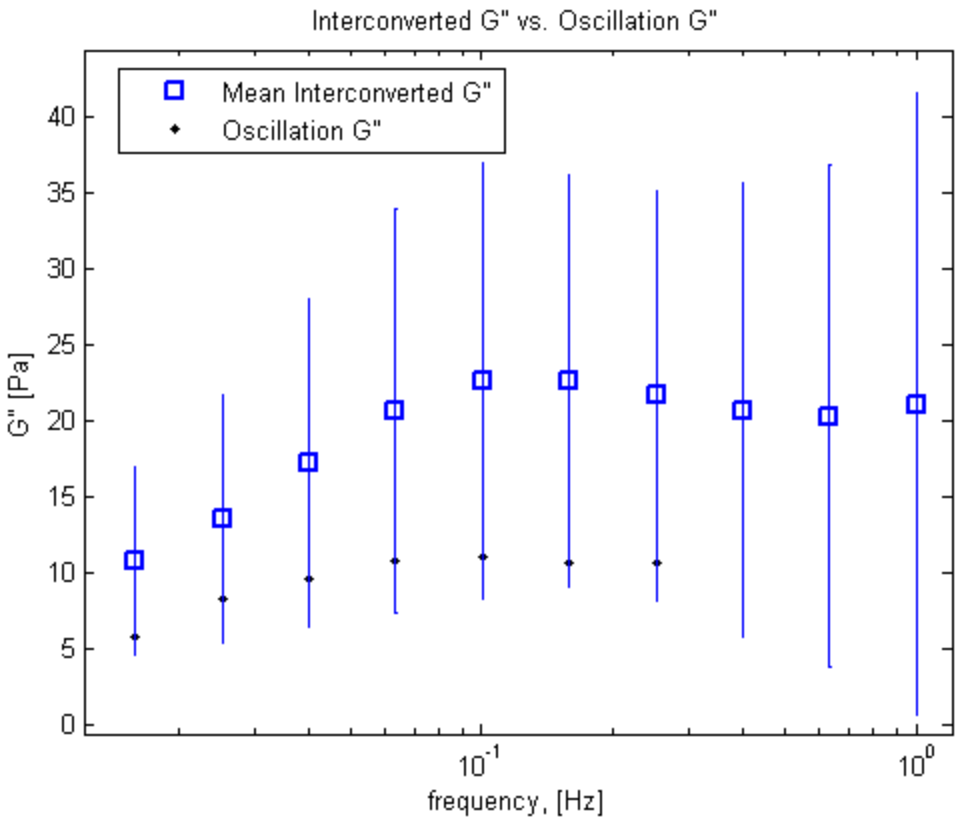

Figure 18: 5-day-old porcine vitreous comparison of the G″ values calculated using the interconversion technique (□) versus using a frequency sweep (●).

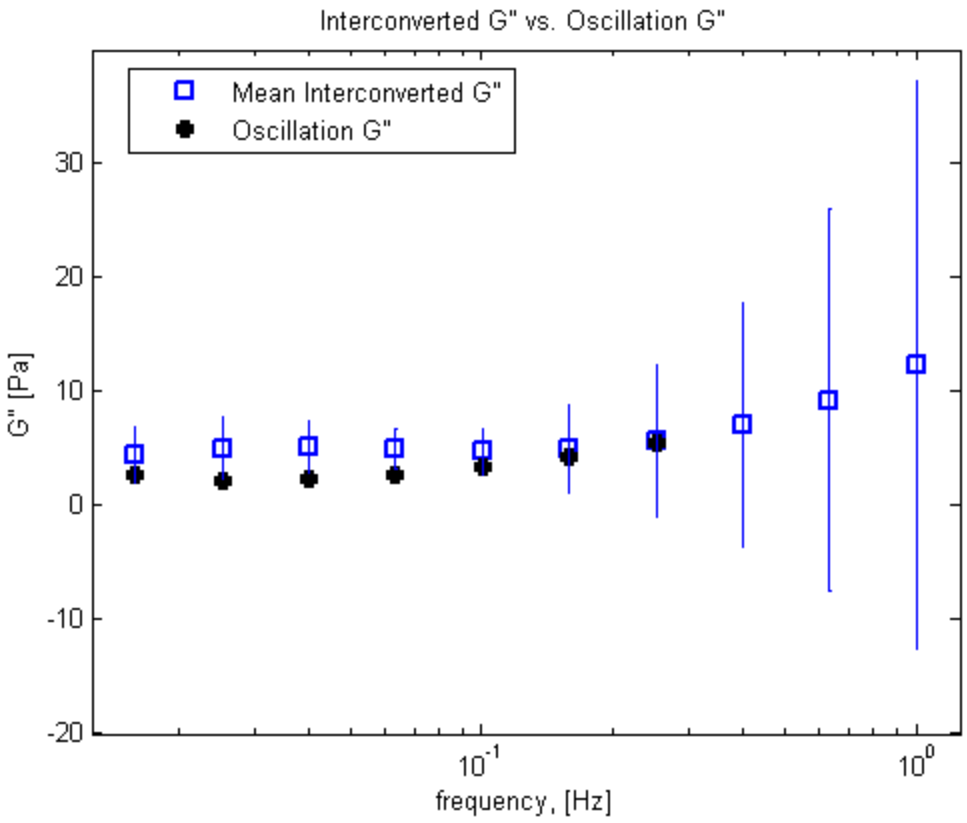

Figure 19: 4-week-old porcine vitreous comparison of the G″ values calculated using the interconversion technique (□) versus using a frequency sweep (●).

Other disadvantages of the standard oscillation testing over the interconversion technique are the effects of resonant frequencies [15] and tool inertia [16]. Tool inertia effects occur when the loss angle (phase angle between strain input and stress response) rapidly increases to 180 degrees. At this point, the signal is largely dominated by inertia and it becomes difficult to determine the true sample loss angle thus resulting in errors [17]. In our case, instrument inertia (~19 $\mu Nm/s^2$) significantly affected the ability to measure agarose, Matrigel, and vitreous properties at high frequencies. Creep tests are not susceptible to such inertial issues because the stress response is supplied by the rotational inertia (~2 $\mu Nm/s^2$) rather than the instrument's motor inertia (~19 $\mu Nm/s^2$)

[15] [18]. Resonance effects amplify a material's response which leads to erroneous G′ and G″ values. These effects can occur during both creep and stress-controlled forced oscillation experiments, but the advantage of the creep test is that only one perturbative stress state is used. Oscillation tests go through multiple stress states, increasing resonance and potentially leading to strain hardening of the material [16]. Therefore, given a predominantly viscous material that is susceptible to significant material property changes with time, the benefits of the interconversion method using a creep test appear to significantly outweigh any limitations, and will result in much more accurate high frequency moduli compared to properties derived from forced oscillation testing.

Statistical tests on the pediatric porcine vitreous indicate that the storage modulus and loss modulus decrease with developmental age. Significant differences were strongest comparing the storage modulus of the 5-day porcine vitreous to the two older age groups. Large variations within the age groups due to vitreous orientation, precision of dissection, and pre-loading[2] could have confounded the statistical analysis. As a result, the statistical power of our experiment was relatively low at some of the higher frequencies where larger variance occurred ($\beta = 0.45$). This may be resolved by increasing the sample size. A decrease in moduli with age is consistent with the age-related structural changes of vitreous reported in the literature [19]. Vitreous is largely composed of collagen fibers that traverse the eye. These fibers are thought to provide structure to the vitreous and dictate the elastic response of the eye. Research has shown that these collagen fibers degrade with age [20], reducing the structural integrity of the vitreous and lowering the elastic response [21] [10].

[2] Pre-loading occurs as a result of lowering the plate geometries onto the sample and therefore changes from sample to sample. This may be significant as vertical displacement is controlled manually.

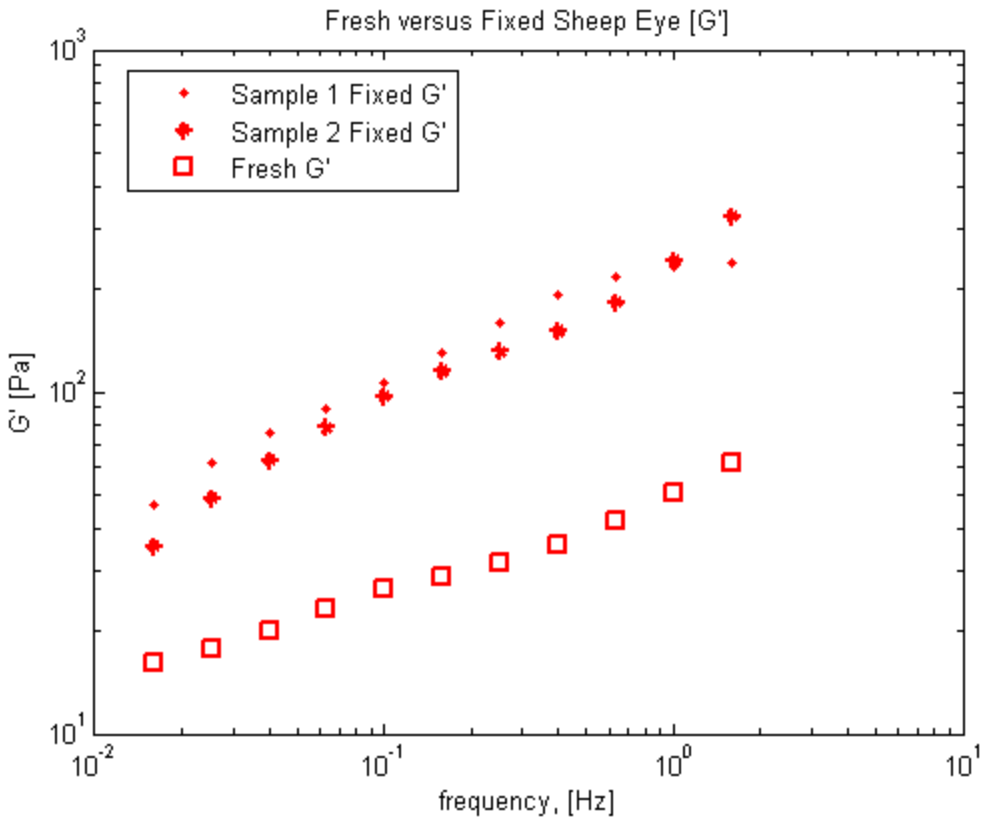

Figure 20: Comparison of the interconverted storage modulus for fixed and fresh sheep eyes.

Eyes used in the analysis were fixed in formalin and likely had altered properties compared to *in vivo* vitreous. However, the comparative differences with age are likely still valid. To estimate the effects of formalin fixation on the absolute measurement of G′ and G″, 132 day old fetal sheep eyes were either fixed in formalin (n=2) or unfixed (n=1). The unfixed eye was tested within 2 hours post-mortem. Eyes were creep tested and interconverted to a frequency spectrum. The storage modulus of the fixed sheep eye was anywhere from 2.5 to 5 times larger than the fresh sheep eye depending on frequency (Fig. 20), and the sheep eye that was fixed had a loss modulus that was anywhere from 1.5 to 5.5 times larger depending on frequency (Fig. 21). The statistical significance of

these results cannot be evaluated due to the sample size (n=1) for the fresh sheep eye, but it is clear that performing mechanical tests on fixed eyes results in an overestimation of the *in vivo* dynamic moduli. Future work will characterize the dynamic mechanical response of vitreous in fresh tissue.

1.7 Conclusion

Interconversion of time-dependent data to obtain frequency-dependent data appears to be a viable technique to obtain dynamic properties of viscoelastic materials

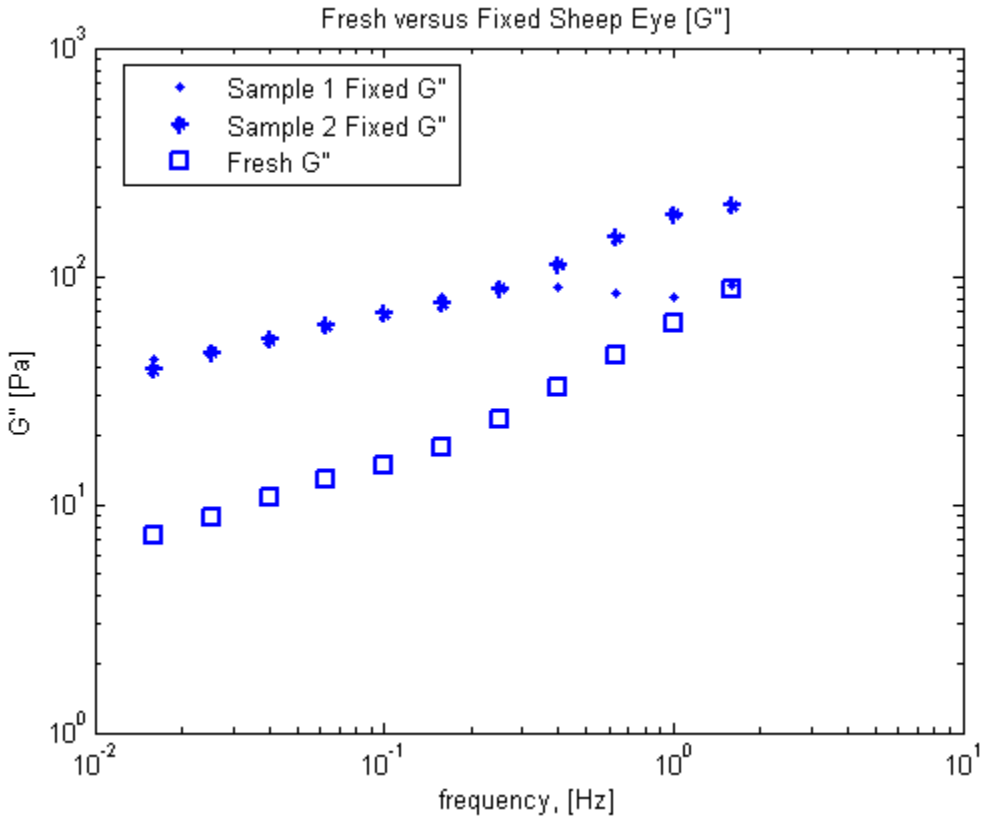

Figure 21: Comparison of the interconverted loss modulus for fixed and unfixed sheep eyes.

when oscillation testing is unavailable. The technique has certain limitations. Small differences in creep data can result in large errors in the resulting interconverted FD data due to the nature of the interconversion technique, so care needs to be taken when obtaining creep compliance data. Elastic dominant materials result in creep ringing which can invalidate the technique. This can be improved by using a peak-to-valley averaging technique, but it may not eliminate all of the errors. Future investigations should refine the averaging technique to lead to a more accurate G″ over a wider range of frequencies.

Interconversion effectively extended the reliable G′ and G″ of vitreous by 0.7 Hz. As expected, the elastic and viscous response of porcine vitreous decreased with age. This trend, however, was only significant between the 3-to 5-day-old and 2-month-old eyes. Other comparisons had large variances resulting in a low statistical power. These comparisons can be improved with more consistent dissection techniques, controlling specimen orientation during testing, and increasing the sample size. The formalin fixation of the eyes increased both the G′ and G″ resulting in an overestimation of the *in vivo* moduli values. Future work should repeat testing on unfixed tissue to verify changes of shear moduli with age are similar to those reported in this study.

CHAPTER 2

BIOLOGICAL SAMPLE PREPARATION FOR SEM IMAGING OF PORCINE RETINA

* Moran P., Coats B., "Biological Sample Preparation for SEM Imaging of Porcine Retina," *Microscopy Today,* vol. 20, no. 2, pp. 28-31, March 2012.

2.1 Abstract

Vitreous is a clear, gel-like material, composed predominantly of water. Biological tissues such as vitreous (i.e., composed mainly of fluids) present difficulties for SEM analysis-both for sample preparation and subsequent imaging. Standard SEM imaging generally requires a high vacuum environment in order to maximize the mean free path of air and improve image resolution. Biological specimens immediately dehydrate in such harsh conditions. In order to successfully image the surface of the retina, a controlled dehydration of the vitreous is required. The unique composition of vitreous makes this process difficult to achieve without creating artificial changes to the sample. To minimize drying artifacts, and optimize image resolution of the vitreoretinal interface, three sample preparation protocols were investigated (ESEM, HMDS, and critical point drying). ESEM was not able to achieve the desired resolution requirements to image collagen *in vitro*. HMDS and critical point drying (CPD) of the porcine vitreous

both resulted in similar image quality, but HMDS was significantly less time consuming. Gradual ethanol drying prior to HMDS or CPD affected the propensity for drying artifacts and thus is an important consideration.

2.2 Introduction

Sample preparation is a critical step in SEM imaging. This is especially true for biological samples because of charge build-up and sensitivity to vacuum and electron beam damage. In terms of ultrastructure imaging, a variety of advancements in detectors and approaches have improved biological imaging such that fewer steps are required for sample preparation. However, the conventional approach incorporating osmium tetroxide fixing, ethanol dehydrating, critical point drying, and coating still finds useful application. Three biological sample preparation methodologies for imaging the ultrastructure of immature porcine retina were compared. The three preparation methods examined are critical point drying (CPD), hexamethyldisilazane (HMDS) dehydration, and direct imaging by environmental scanning electron microscopy (ESEM). Preparation methodologies were evaluated based on resulting image quality and reduced potential for artifacts.

2.3 Scanning Electron Microscopy Methods and Materials

2.3.1 Specimen en bloc dissection

Porcine eyes were fixed for 5 days in a 10% formalin solution and then transferred to phosphate buffered saline (PBS). Extraocular tissue was dissected away, and globes were hemisected anteroposteriorly along the sagittal plane with a scalpel. A

core through the retinal layers, choroid, and sclera was made with a 4 mm diameter trephine and placed on an aluminum stub using carbon dots or an aluminum crucible (for direct examination in ESEM).

2.3.2 Critical Point Drying (CPD)

The first step in the CPD process was to dehydrate the specimen with ethanol. In general, more gradual dehydration minimizes surface tension effects, but there is some ambiguity as to the duration and incrementation of this important step for fragile biological tissues. We selected a dehydration procedure that is standard at our facility for liver and kidney specimens: samples were dried in 70% ethanol for 12 hours and increased to 95% ethanol for two changes lasting 1 hour each. To ensure complete ethanol saturation, the dehydration solution was increased to 100% ethanol for three changes lasting 1 hour each. All samples were critical-point dried using a PELCO CPD2 Critical Point Dryer (Ted Pella Inc., Redding, CA). Temperature and pressure were closely monitored to ensure the samples were not prematurely dried or thermally damaged. Six samples were prepared with 2% osmium tetroxide, and six samples were prepared without osmium tetroxide to determine if post fixation improved imaging and minimized charging artifacts and thermal damage. Additionally, all samples were sputter-coated with ~10 nm of gold-palladium and imaged using a Helix detector in low vacuum on the FEI NovaNano 630. The Helix detector is an FEI NovaNano detector that allows imaging of nonconductive samples in low vacuum mode. Pressures were varied from 0.25-0.4 Torr, but the accelerating voltage remained at 7kV.

2.3.3 Hexamethyldisilazane (HMDS)

Ethanol dehydration was implemented, as described above, followed by three changes of 100% HMDS (Ted Pella, Inc.) for 30 minute durations. After the third change, specimens remained in HMDS until all of the solution evaporated. Samples were sputter coated with gold-palladium and imaged on an FEI Quanta 600 FEG in high vacuum with an Everhart-Thornley detector and also an FEI NovaNano 630 in low vacuum with a Helix detector.

2.3.4 Environmental Scanning Electron Microscopy (ESEM)

ESEM imaging captures specimens in their natural hydrated state and can augment information obtained in other SEMs using extensive sample preparation. Unfortunately, examining the ultrastructure of the retina in its natural state is hindered by the vitreous of the eye. Vitreous is a viscous substance (composed of 99% water by volume) that sits atop the retina surface. Therefore, retina was dissected as described previously, but the specimens were dehydrated slightly in 70% ethanol for 1 hour, and vitreous was physically removed by gently suctioning with a medicine dropper. ESEM was performed on a FEI Quanta 600 FEG with a Peltier stage and gaseous secondary electron detector.

2.4 Results

All SEM imaging methods, except the ESEM, allowed resolution of the filament-like collagen matrix. Initially, the CPD and HMDS samples were found to have peculiar spherical artifacts in the collagen matrix (Fig. 22). By adjusting the accelerating voltage,

chamber pressure, and ethanol procedure individually (not shown), we determined that these artifacts were the result of the ethanol dehydration protocol. Accordingly, a modified dehydration protocol was implemented to incorporate more gradual ethanol increases. The ethanol concentration in the dehydrating solution was increased from 30% to 50% and incrementally increased by 10% up to 100%. The duration of each iteration was 10 minutes. Two additional increments at 100% for 30 minutes ensured complete ethanol saturation throughout the tissue. By modifying the ethanol dehydration protocol to slow the dehydrating process, the artifacts were significantly decreased (Fig. 23). Subtle changes were made to chamber pressure and working distance to analyze the resulting images qualitatively.

Samples without osmium tetroxide from the CPD preparation yielded crisp images of the collagen matrix on the retina surface using the Helix detector at low vacuum (Fig. 24). Specimens subsequently treated with osmium tetroxide, also imaged at low vacuum with a Helix detector, yielded indistinguishable results (Fig. 25).

A comparison of the HMDS image (Fig. 26) with the CPD images (Fig.. 24-25) showed no distinct difference between the two preparation methods. No charging or drying artifacts were observed. The ESEM was unable to resolve collagen fibers on the retinal surface (Fig. 27). Multiple attempts with varying temperature and pressure parameters yielded no progress in the imaging results. Furthermore, air drying during imaging posed a significant problem because of the curling of the thin layers of the retina.

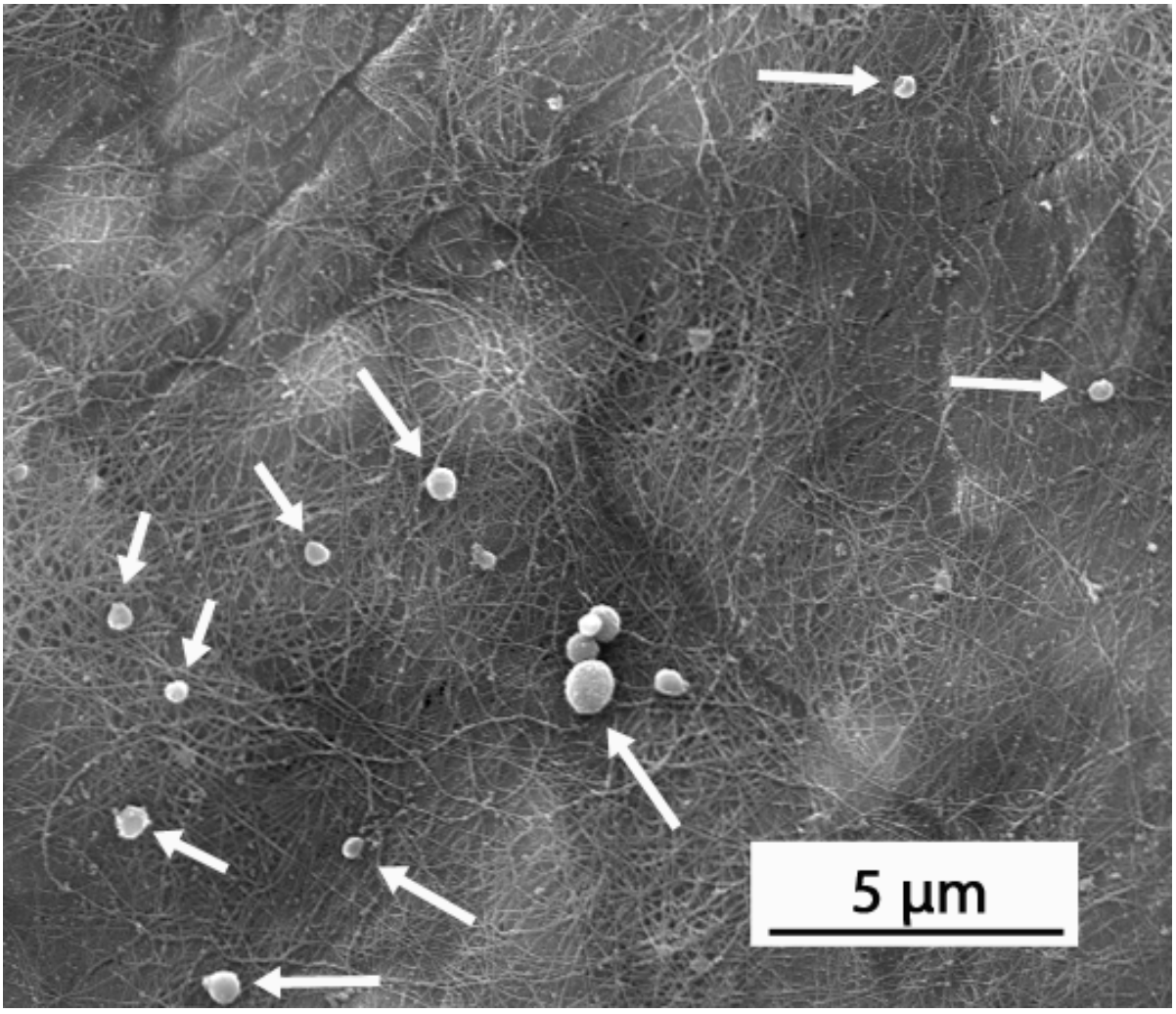

Figure 22: Spherical artifacts (arrows) found in the collagen matrix of the porcine retina. The dehydration procedure was thought to be the cause of the artifact and was changed for subsequent specimens. Imaged using the Everhart-Thornley detector in high vacuum with a magnification of 8000x and 20kV accelerating voltage.

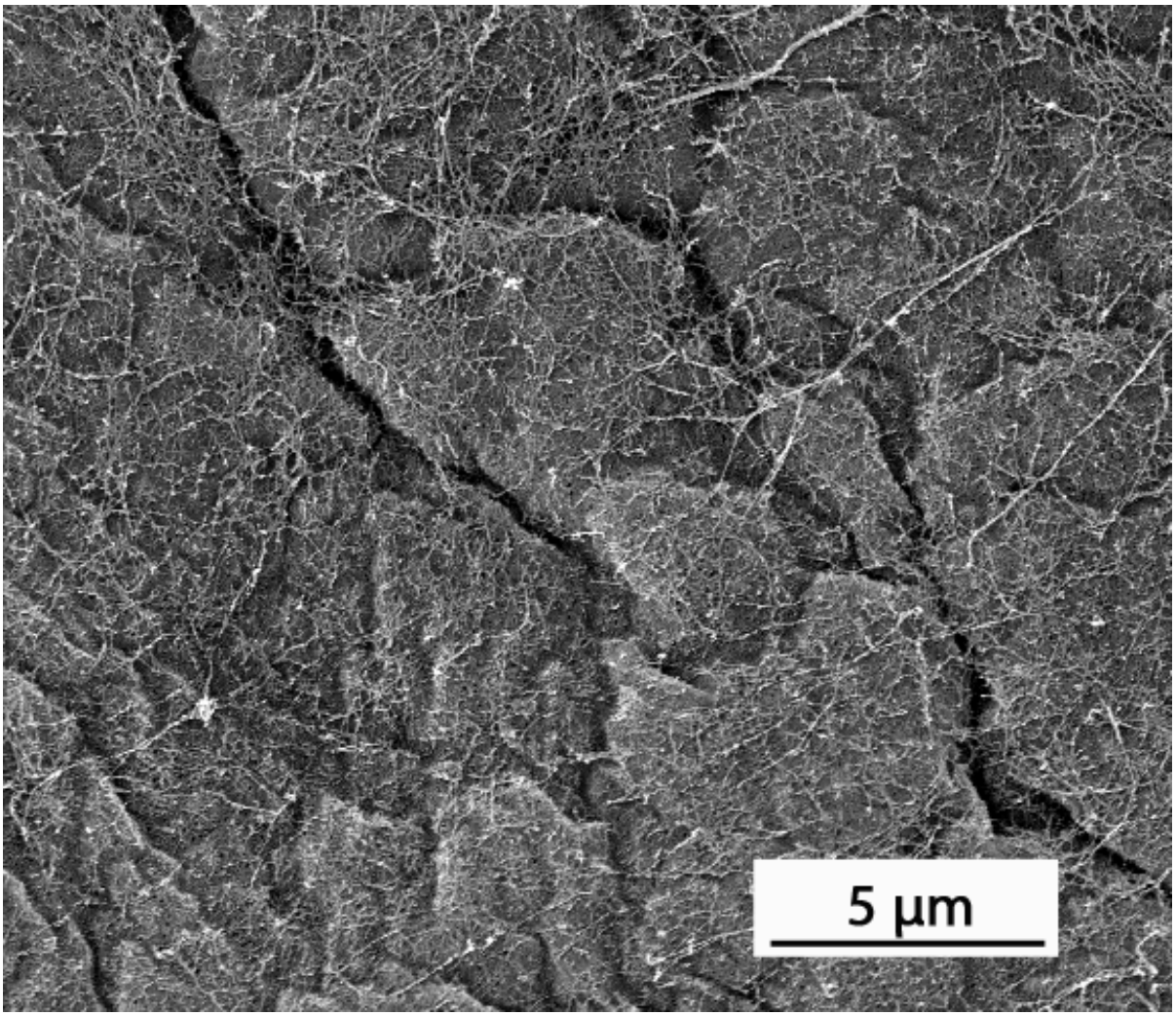

Figure 23: Retina sample that was critical-point dried using a more gradual dehydration protocol to mitigate the spherical artifacts of Fig. 1. Imaged using Helix (SE) detector in low vacuum with a magnification of 8000x, 0.298 Torr chamber pressure, and accelerating voltage of 7kV.

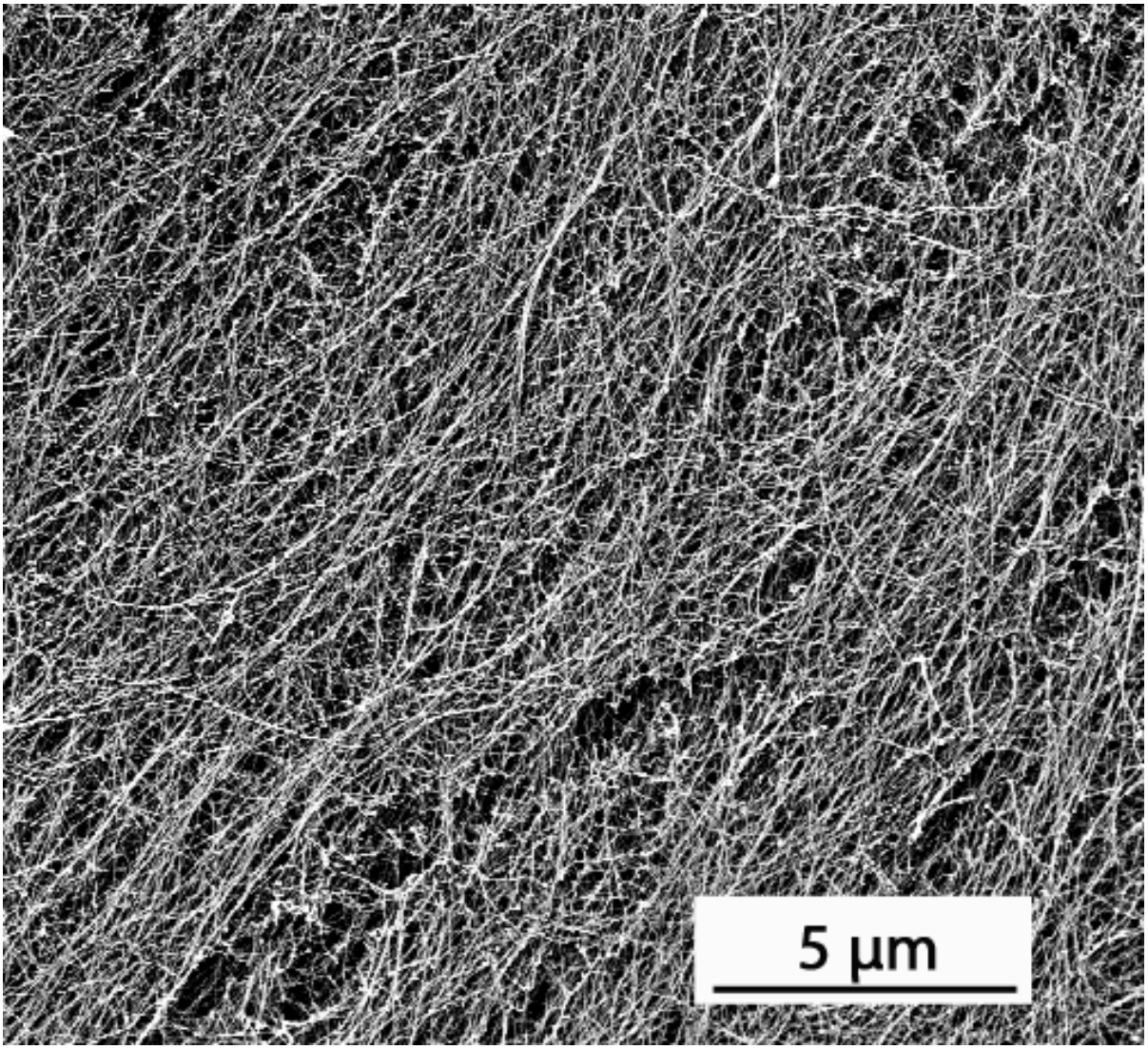

Figure 24: Retina sample critical-point dried without osmium fixation using Helix detector in low vacuum. Image taken at a magnification of 8000x, 0.261 Torr chamber pressure, and accelerating voltage of 7kV.

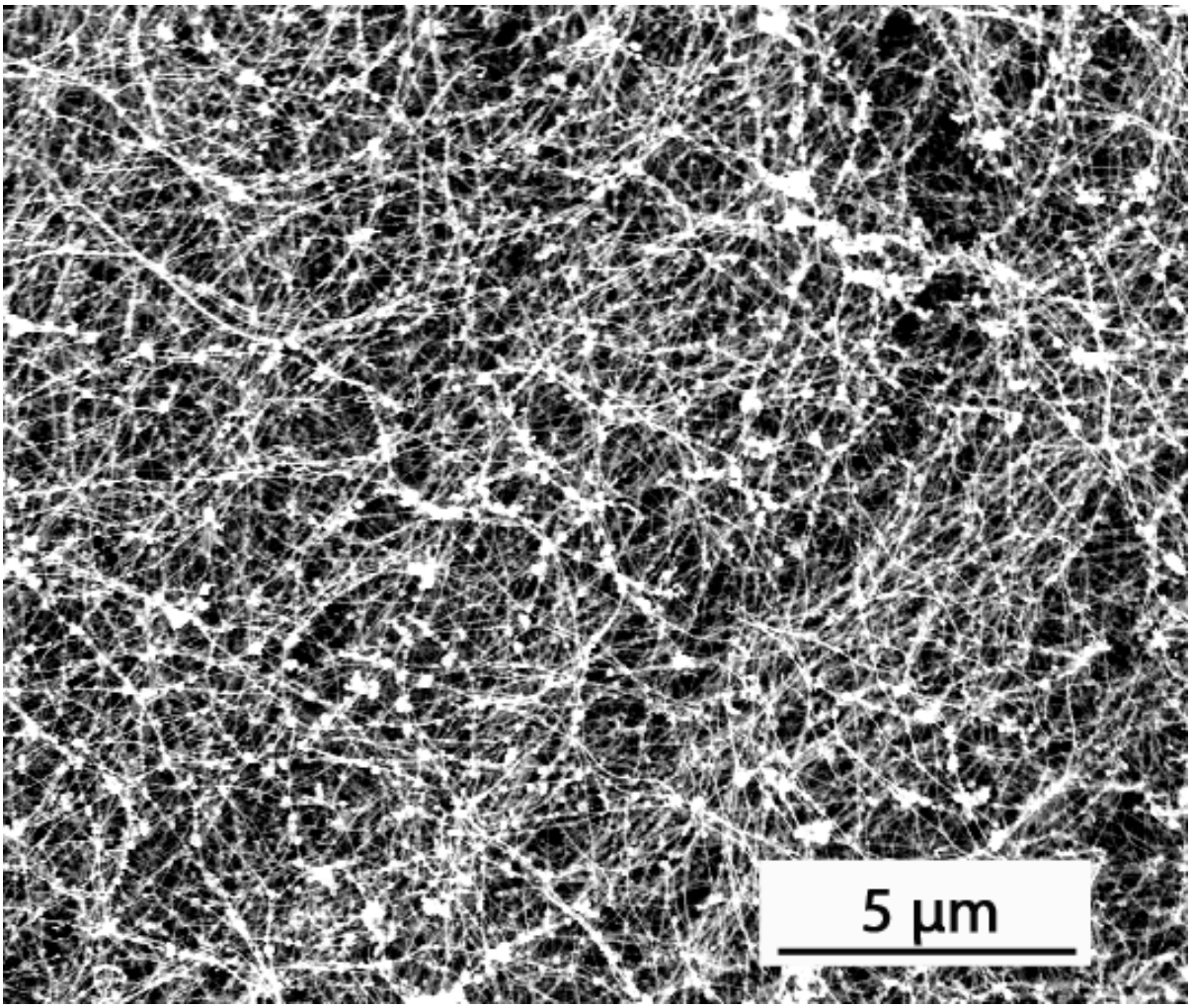

Figure 25: Retina sample critical-point dried with osmium fixation using Helix detector in low vacuum. Image taken at 8000x magnification, 0.376 Torr chamber pressure, and 7 kV accelerating voltage.

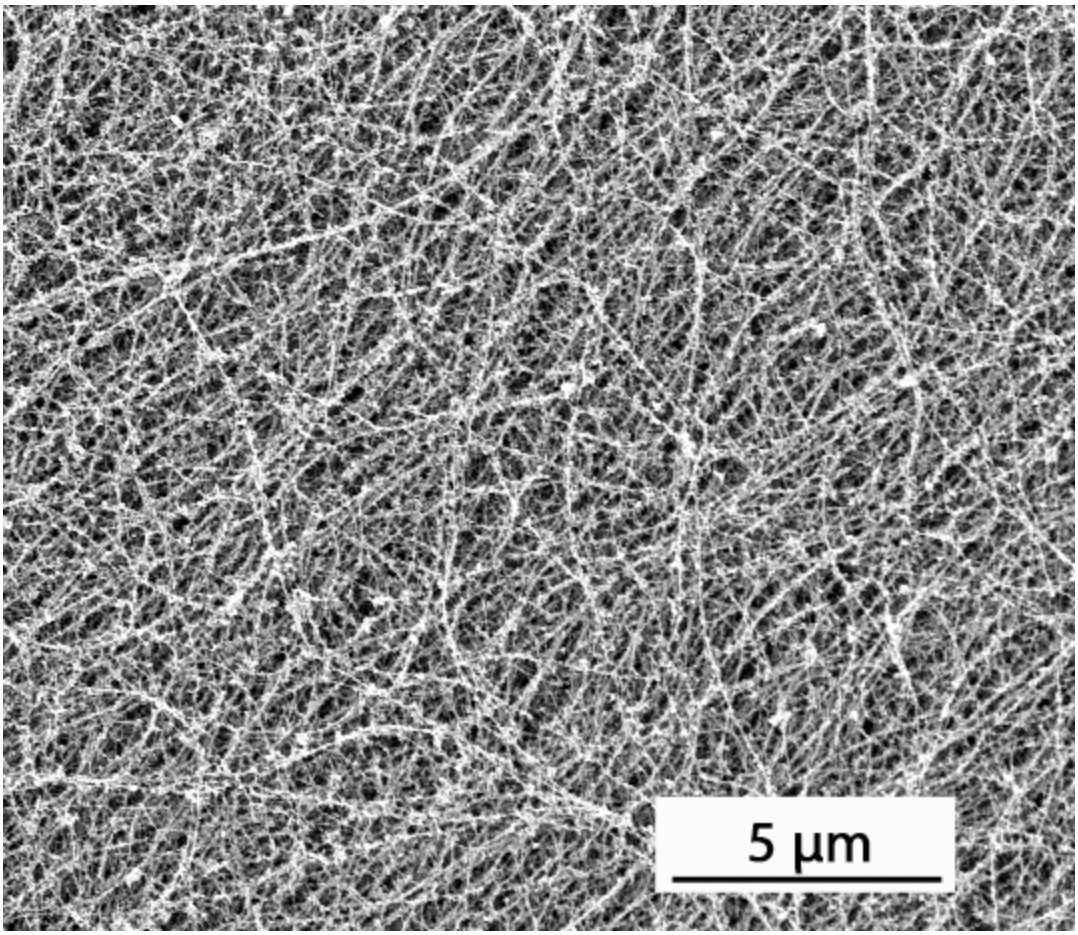

Figure 26: Retina sample prepared with HMDS dehydration and imaged using Helix detector in low vacuum. Magnification of 8000x was used with a 7kV accelerating voltage and 0.301 Torr chamber pressure.

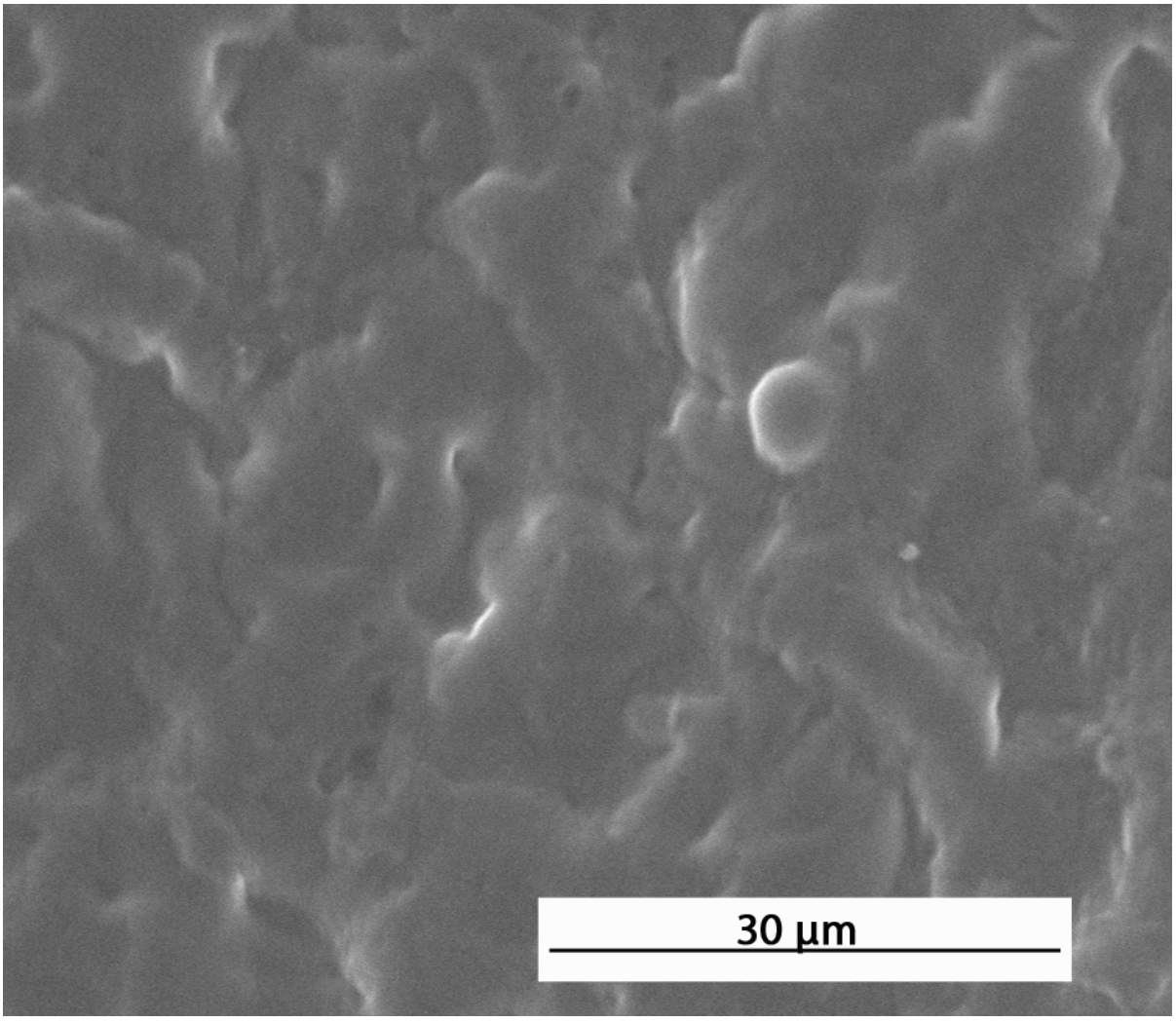

Figure 27: ESEM image taken of retinal surface at 6.499 Torr of water vapor with a magnification of 4000x and 7kV accelerating voltage. The presence of vitreous (99% water) impedes visualization of the collagen matrix on the retina. Attempts to minimize vitreous were unsuccessful, and specimen became thermally damaged (i.e. retina layers curling) within 20 minutes of application of the beam.

2.5 Discussion

In our study, CPD and HMDS preparation methods both provided acceptable image quality and minimal artifacts. While CPD is the most common preparation method, HMDS requires no specialized equipment or precise monitoring of the samples, resulting in lower time and cost commitments than CPD. For immature porcine retina, we found that the HMDS images were indistinguishable from CPD images, and therefore conclude that HMDS is suitable for delicate tissues as long as imaging is conducted in low vacuum. This agrees with other studies that have shown the efficacy of HMDS [22] [23] on non-retina animal tissues. However, CPD still appears to be the preferable method for plant specimens [23].

The ESEM approach was by far the least time consuming of all the methods tested, and the costs were minimal. Unfortunately, imaging the retina surface using this technique proved difficult because of the thickness of the vitreous fluid layer, the poorer image resolution, and the finite duration of the specimen in the ESEM chamber before it became thermally damaged by the electron beam. ESEM has been used to resolve features on the nanometer scale, but this can be difficult with a wet sample [24]. Collagen fibers on the retinal surface are on the order of 10 nm in diameter. The small size of the collagen matrix and the presence of vitreous on the retina surface make ESEM imaging a poor choice for investigating retina ultrastructure.

Another challenge with ESEM imaging is the limited time for imaging of the biological specimen inside the chamber. Despite having some control over pressure and temperature, biological specimens are very susceptible to beam damage and deterioration, and samples may only be imaged once. Typically, biological specimens can be imaged

for 30-60 minutes before significant drying artifacts damage the sample [25] [26]. In our study, the retina lasted 20 minutes, perhaps because of the thin (~200 μm) and multilayered structure.

2.6 Conclusion

Scanning electron microscopy of biological specimens is such that subtle changes in sample preparation can alter image quality as well as introduce artifacts. From our investigation of preparation methodologies for a delicate biological tissue (i.e., retina), we conclude that the CPD and HMDS preparation techniques both result in similar image quality, but HMDS clearly has the advantage of being less time consuming and less costly. If specimens come from previously fixed tissue, additional fixation with osmium tetroxide is unnecessary when using a Helix detector in low vacuum. Regardless of preparation method, gradual ethanol gradient steps should be used to reduce the potential for drying artifacts. ESEM was not found to be useful for imaging collagen in retina samples given the resolution requirements, the natural presence of vitreous on the surface, and the thin multi-layered structure that is extremely susceptible to thermal damage.

CHAPTER 3

QUANTIFICATION OF THE COLLAGEN CONTENT AT THE VITREORETINAL INTERFACE

3.1 Abstract

Collagen at the vitreoretinal interface is thought to play an important role in the adhesion of the vitreous to the retina resulting in retinal detachment or retinal hemorrhages when stressed. Qualitative studies have reported regional and age-related differences in collagen at the vitreoretinal interface, but these differences have never been quantified. In this chapter we created an image segmentation algorithm to quantify collagen at the vitreoretinal interface from scanning electron microscope images. Energy dispersive X-Ray spectroscopy (EDS) was also used to determine if there exist differences in chemical composition. Three age groups and three regions of the eye were investigated. Collagen content was significantly different for different ages as determined from both SEM and EDS image segmentation. No regional effects were observed using image segmentation algorithms; however, the EDS found significant differences by region in sulfur content. This suggests that collagen and retina do vary with age and region, and correlating chemical properties with ultrastructure information can provide a more complete quantification of the vitreoretinal interface. Future studies should investigate the region and age-related changes in chemical composition,

specifically of sulfur, in hydrated and unfixed porcine eyes to verify our EDS findings. Additional SEM image segmentation studies should also be conducted on unfixed eyes using a preparation protocol that limits the extraneous vitreous body included in the specimen extraction and analysis.

3.2 Introduction

As shown in Chapter 1, there is an age dependent change in dynamic viscoelastic material properties of porcine vitreous; however, little is known about the structure and function of the vitreous [27]. Previous studies have observed age-related changes in the vitreous as well as at the vitreoretinal interface [10] [26] using dark-field slit illumination. These studies suggest that adhesion at the vitreoretinal interface is a source of many traction related eye injuries such as posterior vitreous detachment (PVD). In addition, traction between the retina and vitreous has been suggested to cause retinal hemorrhages (RH) in traumatic (SBS or AHT) and nontraumatic events [1]. For improved diagnosis and prevention of these diseases, it is important to understand the age and region dependent characteristics of the vitreoretinal interface. Of particular interest is collagen because it is thought to be responsible for adhesion between the vitreous and retina.

Several scanning electron microscopy (SEM) studies [19] [28] [10] have visually investigated collagen ultrastructure at the vitreoretinal interface and evaluated the regional distribution of collagen qualitatively within the eye [11]. However, to our knowledge, no studies have attempted to quantify the age and region-related changes in collagen content at the interface. We have expanded upon previous analysis methods to incorporate image segmentation algorithms and EDS to quantify collagen content at the

vitreoretinal interface and identify changes with age (3- to 5-days, 4 weeks, 2 months) and region (vitreous base, equator, posterior pole).

3.3 Methods and Materials

3.3.1 Sample Extraction and Preparation

The methods for preparing eyes and creating SEM specimens were previously described in Chapter 2. The left and right eye from two animals for each age group (3-to 5-days, 4-weeks, and 2-month) were dissected for analysis. Two samples (one nasal, one temporal) were removed from three regions (vitreous base, equator, posterior pole) for a

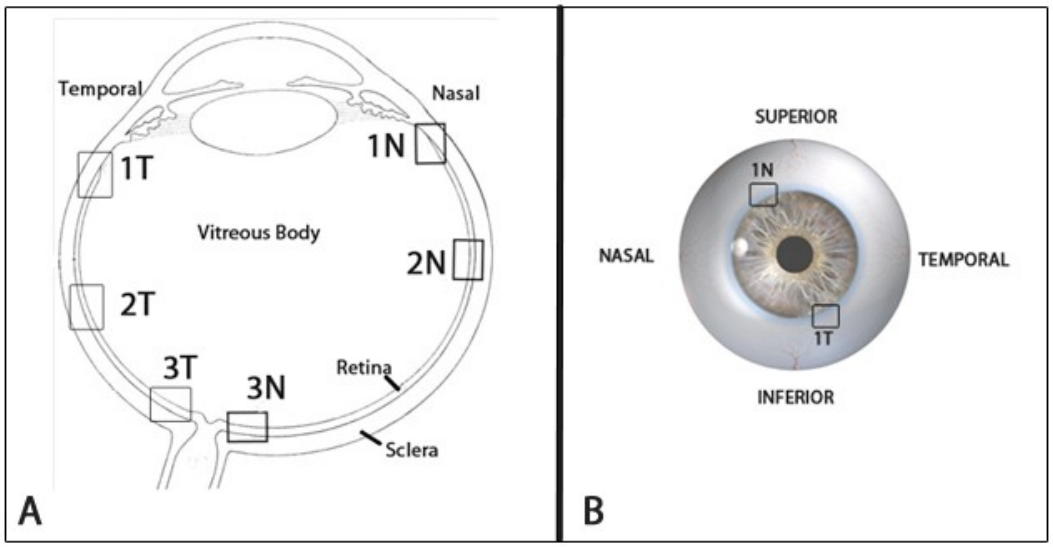

Figure 28: Sample collection from each eye. **A)** Boxes 1N, 2N, and 3N indicate the nasal orientation of the vitreous base region, equator region, and posterior pole region, respectively. Boxes 1T, 2T, and 3T indicate the temporal orientation of the vitreous base, equator, and posterior pole, respectively. **B)** Boxes 1N and 1T signify the nasal and temporal locations, respectively, of the trephine cut through the vitreous base region.

total of six samples taken from each eye (Fig. 28). For consistency, samples extracted from the nasal orientation were also located on the superior surface of the eye, and those from the temporal orientation were located on the inferior surface of the eye. This was applied to both left and right eyes.

3.3.2 SEM Imaging and EDS

All imaging was conducted using the FEI NovaNano 630 (Hillsboro, OR) with a Helix detector. The operating conditions were maintained with the parameters provided in Table 4. Immersion mode was used to improve resolution capabilities in low vacuum. In Chapter 2, gold-palladium was used to coat SEM specimens, but carbon was used for the current experiments because of its better capability with EDS analysis [29]. This change is minor and did not damage the sample. Carbon coating was done using the Denton Vacuum Desk II (Moorestown, NJ). A final carbon coating thickness between 10nm and 30nm was achieved.

EDS was performed on all six specimens taken from a single 5-day-old (n=1) and 2-month-old (n=1) eye. For each specimen, a regular SEM image was taken first and then the EDS was performed. Seven different elements were determined relevant for the EDS

Table 4: Operating parameters used in the SEM studies of collagen content.

PARAMETER	VALUE
Pressure	0.25-0.40 Torr
Vacuum	Low
Voltage	7 kV
Magnification	8000 x
Current	~0.25 nano-Amperes (nA)

analysis: carbon, nitrogen, oxygen, sodium, silicon, phosphorus, and sulfur. The EDAX detector (EDAX Inc., Mahwah, NJ) attached to the FEI NovaNano 630 was adjusted such that the detector was located ~49mm from the sample. Each spectrum was collected for 2 minutes.

3.4 Data Analysis

3.4.1 SEM Analysis

An image segmentation program to quantitatively evaluate the collagen content at the vitreoretinal interface was developed using MATLAB. The code (Appendix C) exploits the inherent contrast differences between the retina and collagen that result from SEM. Each image is pre-adjusted to filter the 10 percent darkest and 10 percent lightest pixels. This reduces the effects of charging, which saturates the pixels, and dark regions where the contrast is poor. The pixels were then normalized to a 0-255 grayscale range. An absolute threshold of 153 was selected as the optimal grayscale threshold for all images based on preliminary examination of several images. This threshold was not changed throughout analysis. Pixels above the threshold were considered collagen fibers and pixels below the threshold were considered retina. The total percent collagen was defined by Equation [1].

$$\left(\frac{Collagen\ \ Pixels}{Total\ \ Pixels}\right) \times 100 \qquad [1]$$

3.4.2 EDS Analysis

EDS quantification of the elemental components at the vitreoretinal interface was computed within the NovaNano 630 EDAX detector and software. Briefly, the software

counts the atomic particles of various elemental components and normalizes them from background noise (Fig. 29). The resulting counts are reported and identifiable peaks are given as weight and atomic percent values of the selected elements. Elemental quantification uses the ZAF method which accounts for the interactions between the specimen and elements' characteristic x-ray that reduce the signal: z-number effects, absorbance effects, and fluorescent affects. For our analysis, we compared the atomic percent (At %) values for statistically significant differences between ages and regions.

3.4.3 Statistics

A two-way ANOVA was used to determine if the collagen quantity determined from the image segmentation program was significantly different among age groups (3-to 5-day, 4-week, 2-month) and regions (vitreous base, equator, posterior pole). A multivariate two-way ANOVA was used to analyze significant differences in the seven chemical components resulting from EDS analysis of specimens from two of the animal ages (3-to 5-day, 2-month) and the three eye regions examined. A level of $p<0.05$ was defined as significant.

3.5 Results

3.5.1 Image Segmentation Analysis

No significant differences in collagen content were found among the three regions ($p=0.248$), but age did significantly affect collagen content ($p=0.002$) (Fig. 30). The interaction between the two independent variables (age and region) was also statistically significant ($p\leq0.001$). Occasionally, collagen fibers were easy to distinguish from the

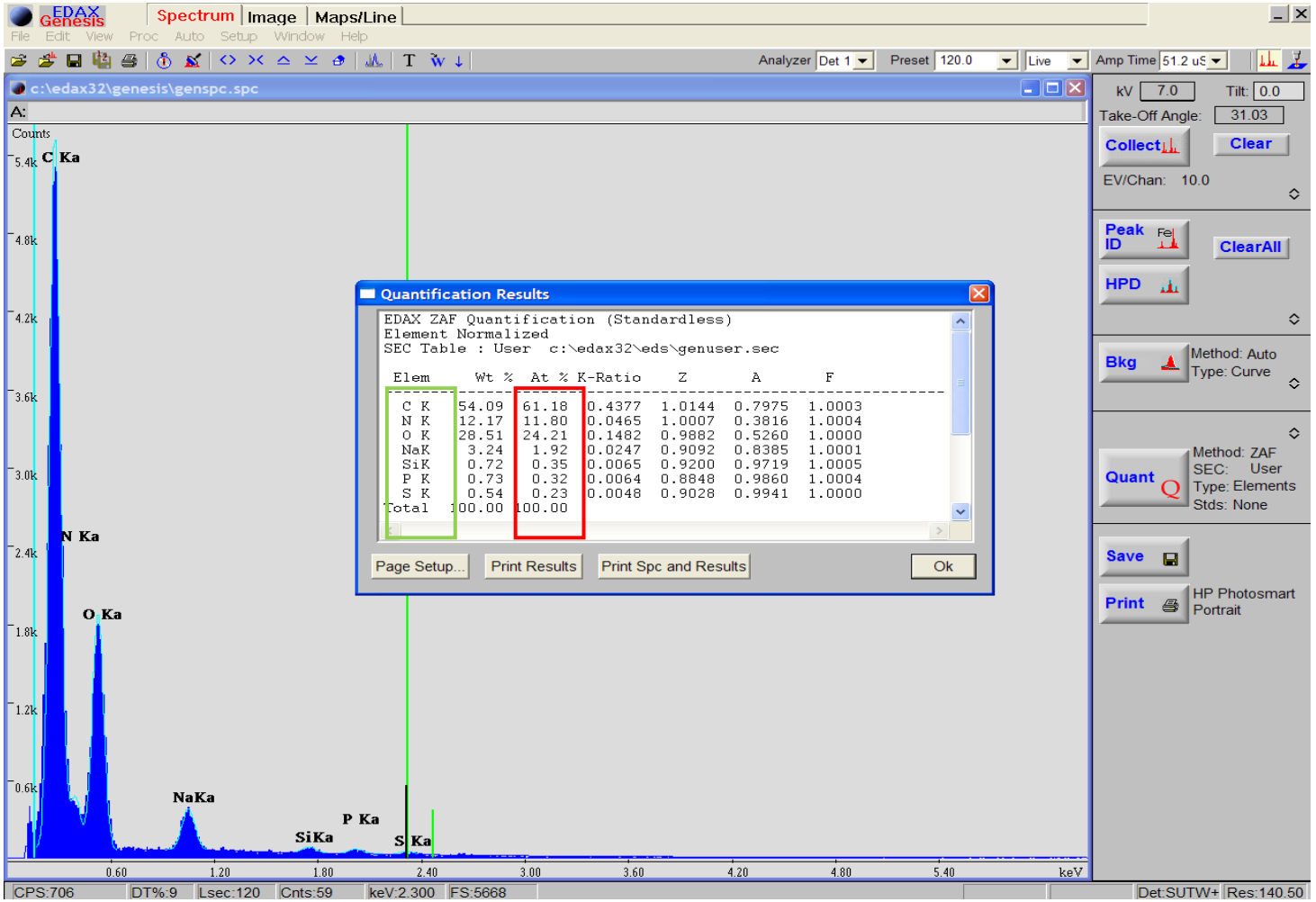

Figure 29: Representative EDAX spectrum for the seven elements (green box) investigated. Statistical analysis was performed on the corresponding atomic percent values (red box). The "Ka" values after the elemental name indicates which orbital shell the signal originated.

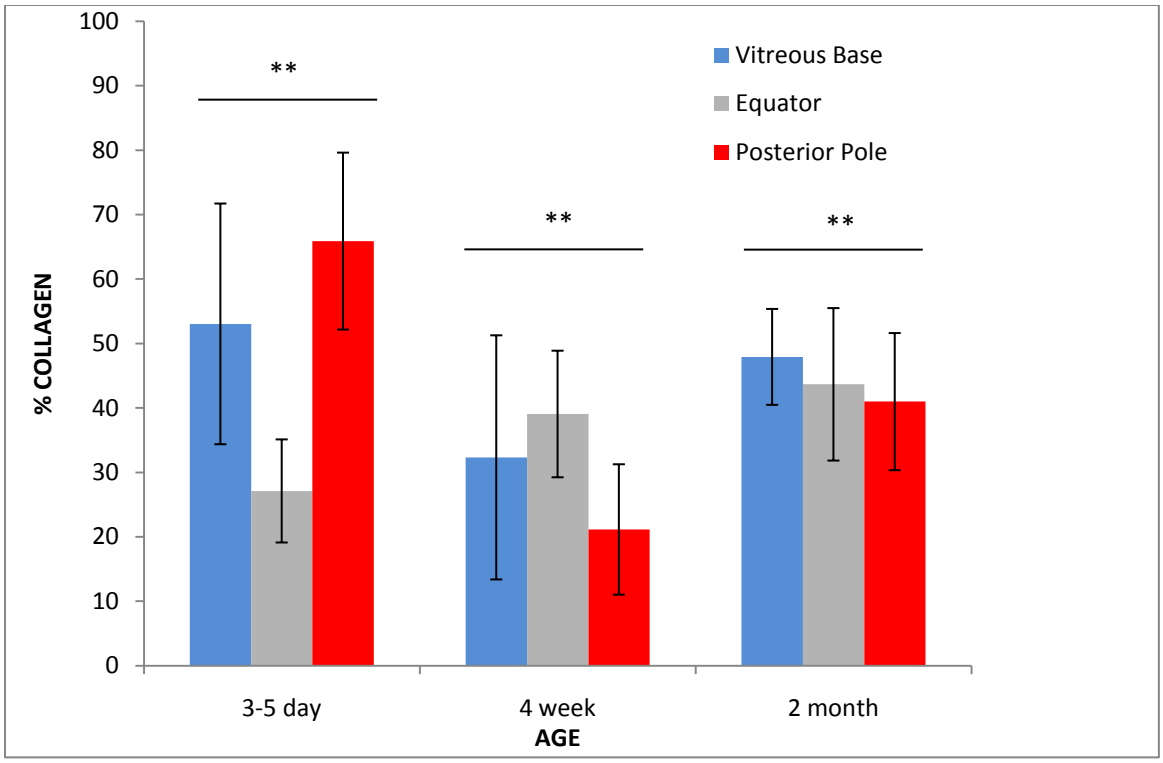

Figure 30: Age and region statistics (Mean ± SD). Significant differences ($p<0.005$) in age (**) were identified, but no regional differences were found.

background retina (Fig. 31- 32), but the majority of the SEM images were dominated by collagen from the vitreous and made identifying retina difficult (Fig. 34). In some images there were charging artifacts which affected quantification of collagen. Significant interaction effects between age and region were identified.

3.5.2 EDS Analysis

The achievable signal count, measured in counts per second (CPS), was between 500 and 900 during the EDS testing. There were significant differences between the two ages for four of the chemical components. As shown in Table 5, carbon ($p=0.009$), nitrogen ($p=0.025$), silicon ($p\leq0.001$), and sulfur ($p=0.007$) had significant age

differences (bold) with carbon, silicon, and sulfur being higher in older animals, and nitrogen being smaller. There were also significant regional differences in the presence of sulfur ($p=0.002$) (Table 5) with significantly lower amounts of sulfur in the vitreous base compared to the equator or posterior pole. No significant interaction effects between age and region were found.

3.6 Discussion

To quantify collagen at the vitreoretinal interface, image segmentation of SEM images and EDS analysis were performed. Image segmentation of images resulted in significant differences with age, but not with region. This is contradictory to observed levels of collagen in different regions of the eye. Previous literature has identified a significant increase in the collagen fibers of the vitreoretinal interface of the vitreous base relative to the equator and posterior pole, while the differences between the equator and posterior pole were comparable [19]. One reason for the discrepancy is likely that the SEM images in our analysis had copious amounts of collagen from the vitreous body. Our protocol used a trephine to create the specimens for SEM. The trephine cut through the vitreous of the eye before cutting through the retinal layers. This resulted in vitreous being incorporated into the retina samples. Vitreous naturally has a large amount of collagen which is fairly uniform throughout the vitreous. Once dried, the vitreous collagen stacked on top of the collagen at the vitreoretinal interface and made identifying regional variations difficult. Collagen in the vitreous does decrease with age [10] [27], which explains why the data were significantly affected by age, but not region. Carbon was chosen over gold-palladium coating due EDS analysis. Carbon has a lower

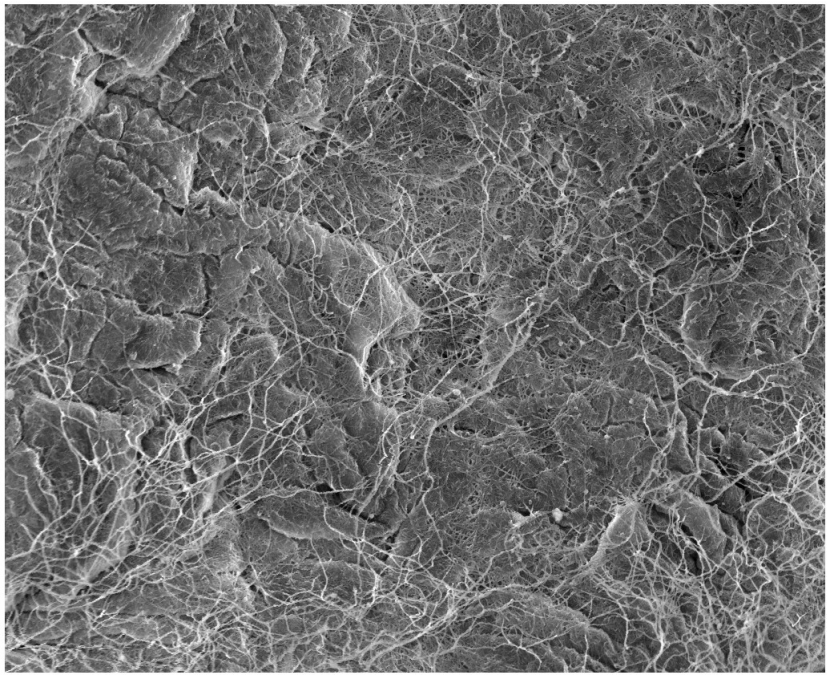

Figure 31: Representative SEM image of collagen with retina visible in background. Image of 4-week-old retina taken from the posterior pole. 8000x magnification.

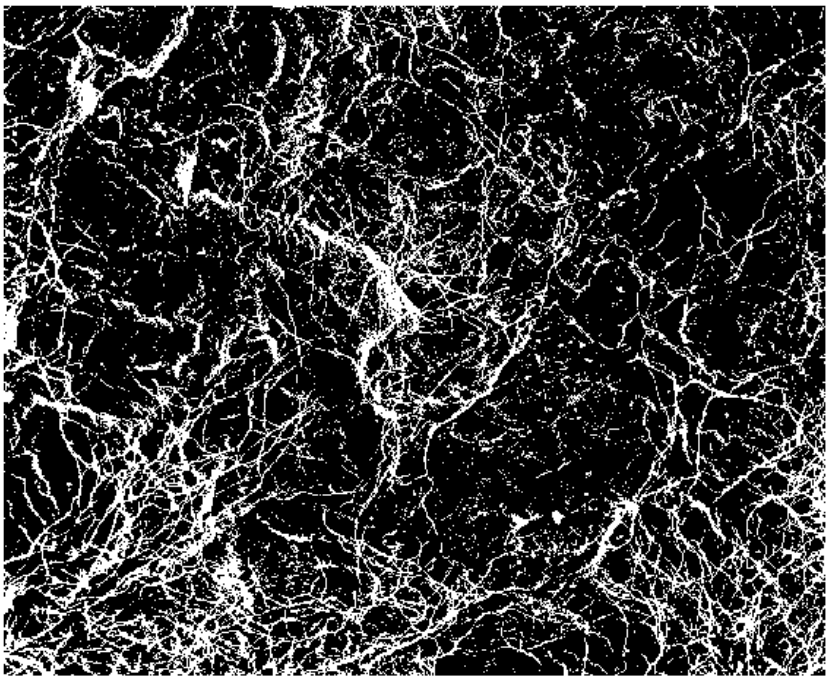

Figure 32: Image segmentation results of contrasted collagen (white) and retina (black). The corresponding collagen content was 20.85%.

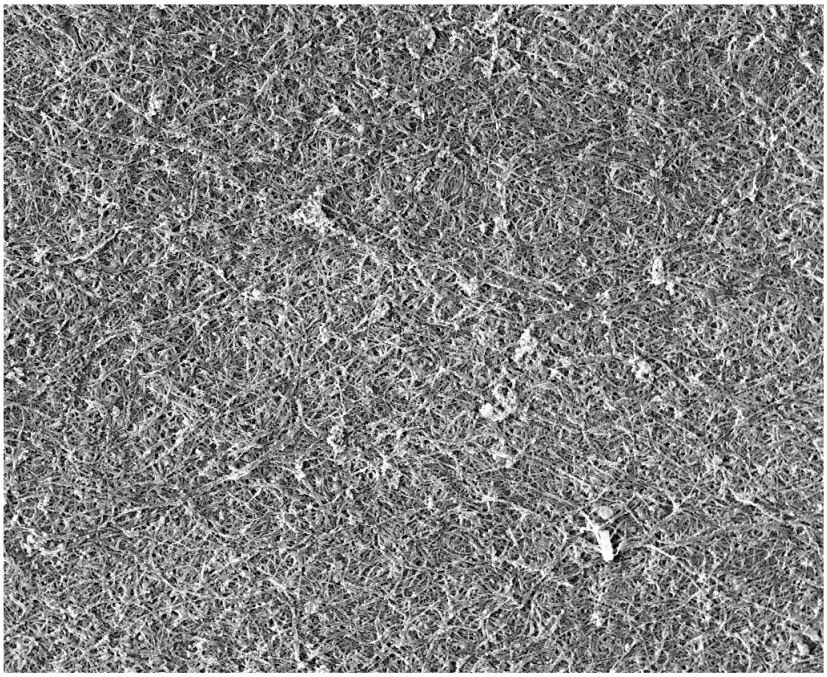

Figure 33: Representative SEM image of collagen without visible retina. Image of 2-month-old retina taken from the equator. 8000x magnification.

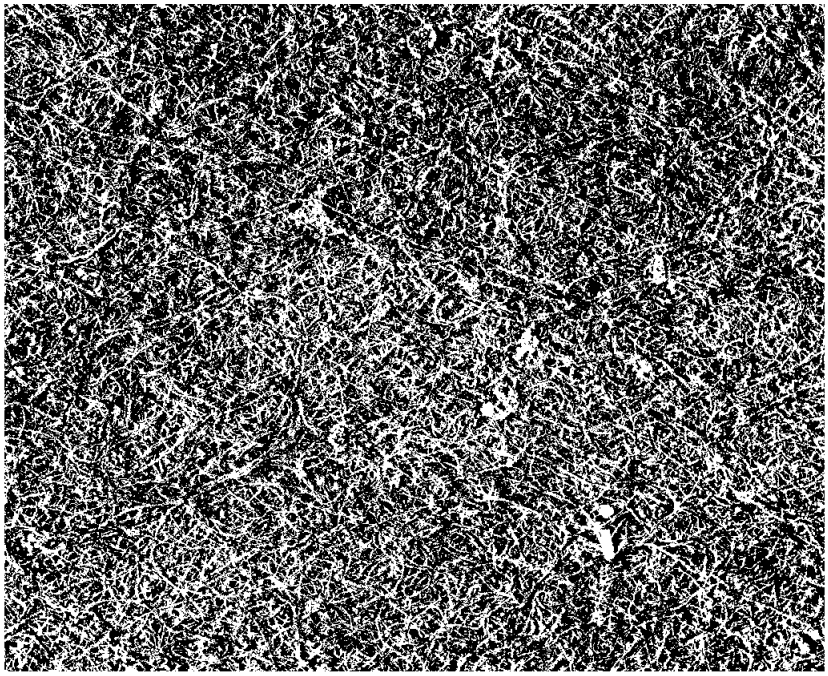

Figure 34: Image segmentation results of contrasted collagen (white) and retina (black). The corresponding collagen content was 38.68%.

Table 5: Chemical composition statistical analysis results for the four chemical components of interest (Mean ±SD). Significance in age (**bold**) found for all four elements, but only sulfur showed regional difference effects (*italics**).

Element	Group	Age	Mean	Std. Deviation
Carbon	Total	5-day	**62.8733**	1.91538
		2-month	**66.0433**	1.67382
Nitrogen	Total	5-day	**13.125**	1.28777
		2-month	**11.145**	0.65613
Silicon	Total	5-day	**0.3283**	0.04309
		2-month	**1.0933**	0.18694
Sulfur	Vitreous Base	5-day	*0.14**	0.01414
		2-month	*0.18**	0.02828
	Equator	5-day	*0.205**	0.00707
		2-month	*0.24**	0.01414
	Posterior Pole	5-day	*0.205**	0.00707
		2-month	*0.235**	0.00707
	Total	5-day	**0.1833**	0.03445
		2-month	**0.2183**	0.03312

absorbance than the gold-palladium meaning that more of the elements are analyzed resulting in better accuracy. Unfortunately, biological specimens can still manifest charge build-up on the imaging surface. Charging causes regions of intense saturation on SEM images and can hinder the image segmentation algorithms which rely heavily on the contrast between collagen and retina. From sample to sample, the charging varied from being very prominent to none at all, possibly due to the nonuniformity of the deposition of the carbon. Large variations in the standard deviation (SD) likely resulted from the variation in charging.

Utilizing EDS to qualitatively analyze the amount of a collagen can be advantageous especially if used effectively in conjunction with using ultrastructure imaging [30] [31]. EDS provides information about subsurface details of the samples by analyzing energy levels of the electrons ejected from the element's electron shell. In this way, chemical information from the surface and deeper (~1 μm based on Monte Carlo simulations) can be analyzed and quantified. It is difficult, however, to identify the exact depth of the analysis. According to a previous study, the x-rays may analyze within 5μm of the sample [31]. The retinal thickness is on the order of 300μm thick, so the chemical components from our analysis were likely on the surface of the retina or within the top layer of the retina.

Absolute quantification of the chemical composition of collagen or retina is impractical given the chemical fixatives and desiccants used to dry the sample. As such, this study only sought to qualitatively compare how elemental constituents of the vitreous and retina varied with age and region. Four elemental components significantly differed between the two age groups: Silicon, nitrogen, carbon, and sulfur. Silicon is not native to

the eye, but is found in HMDS. Therefore, the presence of this chemical is likely an artifact of the HMDS drying protocol. Nitrogen is an element found in the eye, but it is also found in HMDS. Therefore, it is unclear if the significance is real or an artifact of the drying protocol. Carbon is a known element of both collagen and retina, so we cannot determine if a significant difference in carbon means an increase in the collagen-retina ratio or vice versa. HMDS and ethanol also contain carbon so the significance may also be a drying artifact. To our knowledge, the collagen fibers within the vitreous are not known to contain sulfur, but sulfur has been identified as a constituent of melanosomes found in the retinal pigment epithelium (RPE) [30] [32]. The RPE is located within 200μm of the retina, so it is uncertain if the measured sulfur is from the RPE or a retinal layer closer to the vitreoretinal interface. Regardless, the reported sulfur content could indicate that a higher ratio of retina to collagen is present (Fig. 35). Sulfur in the vitreous base (0.16 ± 0.029) was significantly lower than that in the posterior pole (0.22 ± 0.018) or equator (0.223 ± 0.022). This is consistent with previous observations of collagen at the vitreoretinal interface [19].

3.7 Conclusion

Careful preparations were made to ensure the repeatability and reliability of our image segmentation results; however, the eye preparation method extracted extraneous vitreous body, and therefore collagen fibers, at the vitreoretinal interface which artificially increased the reported collagen fiber content. In addition, charging artifacts, inherent to biological specimens, created large sample to sample variability. As such, the image segmentation of SEM images alone did not allow for meaningful conclusions

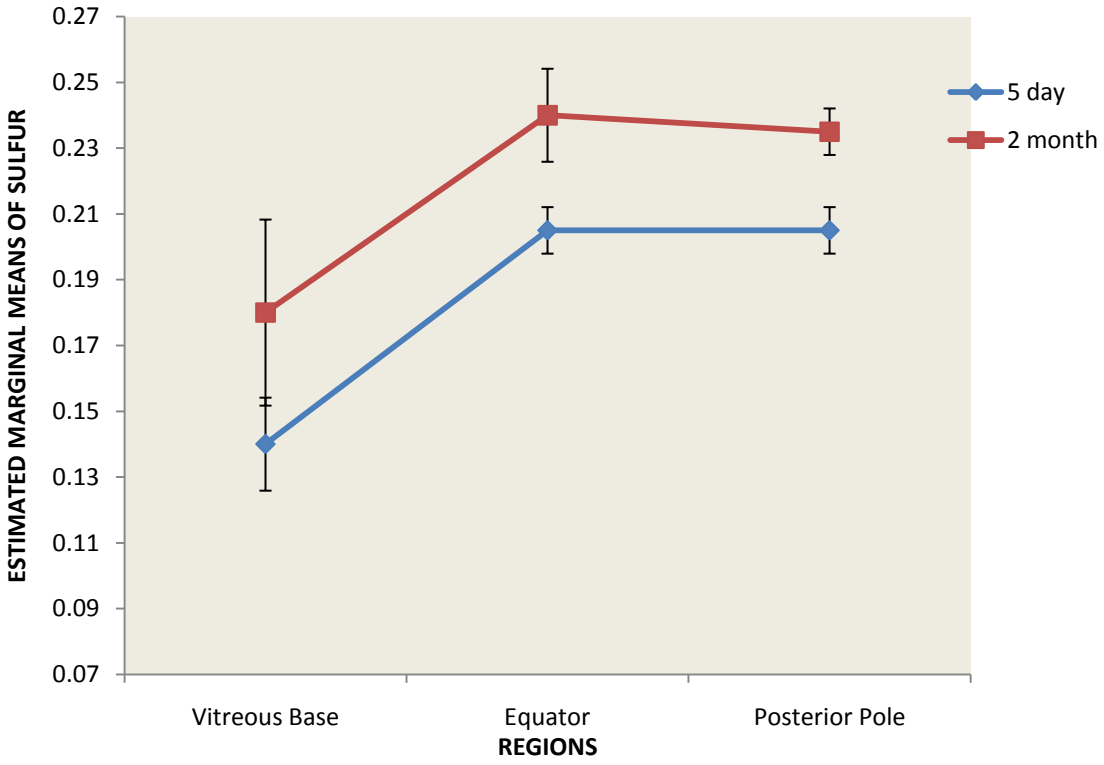

Figure 35: Comparison of the mean sulfur differences with age in the three regions (vitreous base, equator, posterior pole).

about the age and region dependent quantity of collagen fibers.

EDS identified significant differences in sulfur across three regions of the eye, and significant differences in carbon, nitrogen, silicon, and sulfur for two ages. The results of nitrogen and silicon are likely not meaningful due to their presence in HMDS. A comprehensive analysis of the effect of chemical fixation with formalin and chemical dehydration with HMDS should be evaluated. Carbon, being present in both collagen and retina, limits the conclusions that can be gleaned regarding collagen content. Sulfur showed an increase with age which may be indicative of more amounts of retina relative to collagen. Sulfur content was lower in the vitreous base, suggesting amounts of collagen in that region compared to the equator and posterior pole. These findings are

supported by previous studies that have reported collagen content being highest in the vitreous base [11] [19]. However, these results provide only a qualitative description of the age dependent changes in collagen fiber. To quantify these changes in a more meaningful way (i.e., image segmentation analysis) a change in the methodology for extracting the samples for SEM imaging would be necessary such that only collagen fibers at the vitreoretinal interface are evaluated.

CONCLUSIONS AND FUTURE WORK

Interconversion of time-dependent data to obtain frequency-dependent data has been shown to be a viable technique to obtain dynamic properties of viscoelastic materials when oscillation testing is unavailable. This technique is most effective for materials whose response is more viscous (i.e., polymer-melts such as PS) as certain limitations have been identified when the inertia-elastic coupling between the sample and the rheometer result in creep-ringing. These elastic dominant effects must be removed before using the technique. We have shown that by using an averaging technique over the region where the ringing occurs, we can reduce these errors such that the storage modulus (G′) of the material is accurate over the entire interconverted frequency spectrum. However, the interconverted loss modulus (G″) continues to be inaccurate. To improve the accuracy of G″ over a wider range of frequencies in elastic dominant materials, future investigations should refine the averaging technique. One suggestion is to find the midpoint between each peak and valley of the oscillation and use that as a data point. This will result in twice the amount of data that is currently used to create the creep compliance curve.

Interconversion effectively calculated G′ and G″ of porcine vitreous over a broader frequency range compared to forced oscillation data. Using the interconversion technique, G′ was calculated from 0.01Hz-1.0Hz and G″ from 0.01Hz-1.0 Hz while only 0.01Hz- 0.3Hz were able to be trusted from oscillation data. The dynamic shear moduli

of porcine vitreous decreased with age, but this was only significant between 3-to 5-day-old and 2-month-old eyes. Other comparisons (3-to 5-day to 4-week; 4-week to 2-month) had large variances that could be improved with more consistent dissection techniques, controlling specimen orientation during testing, and increasing the sample size. Due to the overestimation of G′ and G″ resulting from formalin fixation, future work should repeat the testing on unfixed tissue to verify changes of shear moduli with age. In addition, regional shear moduli should be investigated, using the interconversion technique, to determine significant differences between anterior and posterior vitreous.

Our investigation of preparation methodologies indicated that for delicate biological tissue, such as the retina, CPD or HMDS preparation techniques are both appropriate. HMDS is clearly more advantageous as it is less costly and time consuming. Regardless of preparation method, gradual ethanol gradient steps are critical to reducing drying artifacts.

Isolating the vitreoretinal interface at different regions and developmental ages was achieved. However, the eye preparation method also extracted extraneous vitreous body, and therefore collagen fibers, at the vitreoretinal interface. Significant age differences were found using the image segmentation algorithm, but the excess collagen at the vitreoretinal interface was a confounding variable. In addition, charging artifacts saturated the contrast in certain images. This caused difficulties for quantifying collagen using image segmentation methods and resulted in large regional and age standard deviations. Future studies should investigate appropriate methods to remove the extraneous vitreous body at the vitreoretinal interface. This may included repeated flushing of the surface or potentially using CPD as it is inherently more abrasive to the

samples[3]. Quantifying the collagen at the vitreoretinal interface may also be more reliable using transmission electron microscopy (TEM). This circumvents the issues of extraneous collagen fibers because TEM generates cross-sectional images that show insertion points for the individual collagen fibers. Additionally, adhesion testing of the vitreoretinal interface could be incorporated into future studies to test for regional and age dependent, in addition to direction (anisotropy), force measurements. Preliminary vitreoretinal adhesion studies in our lab have demonstrated the ability to measure adhesion between the retina and vitreous.

EDS was used to identify qualitative changes in the seven elements measured by the EDAX detector. Significant regional differences in sulfur were identified while age differences included four of the seven elements: carbon, nitrogen, silicon, and sulfur. Chemical fixatives and desiccants likely contributed to the age differences associated with carbon, nitrogen, and silicon. Sulfur, being a known constituent in the melanosomes of RPE, may be indicative of actual differences in the collagen content, where an increase in sulfur content indicates an increase in retina and associated decrease in collagen. In our study, sulfur increased with age and was higher in the posterior pole and equator than the vitreous base which is comparable to observations reported in the literature. In addition to the SEM image segmentation analysis on unfixed eyes, future EDS analysis should validate the qualitative findings of this study with eyes that are unfixed and hydrated.

[3] As liquid carbon dioxide in the CPD chamber passes the critical point, a turbulent environment (boiling) is created. This may be assist in removing the extra vitreous body in a consistent manner.

APPENDIX A

CUSTOM PARALLEL PLATE CLEAT DESIGN

Previous research [33] has shown that certain materials, specifically vitreous, are prone to wall slip phenomena. Preliminary investigation in our lab confirmed that pediatric vitreous also suffers from wall slip [34]. To eliminate these effects we created four custom cleat designs and optimized for slip prevention by varying both the height and cross-sectional area parameters. Two cleat heights (0.6mm and 0.9mm) and two, square cross-sectional areas (0.45 x0.45mm and 0.6 x0.6mm) were used in our investigation of mitigating wall slip. The design parameters were evaluated on porcine vitreous and the 0.6 x0.6x0.9mm (LxWxH) geometry was the most successful at suppressing slip [34].

Three cleats (Fig. 36) were used to mitigate slip for the vitreous and materials used for verification: a commercial geometry (C1) and two custom parallel plate geometries (C2, C3) that had the same cleat design, but different overall diameters. The custom cleat designs, C2 and C3, were used to mitigate the apparent slip in vitreous and Matrigel, while the commercial cleat design, C1, was used to mitigate the slip in PS and agarose. The cleat geometries were successful in suppressing the slip, but to accurately interpret data gathered while using these modified geometries, an 'effective gap height' had to be determined because the no-slip boundary layer was different with each geometry.

Following the same techniques used by Nickerson and Kornfield [33], effective gap heights for the new geometries were derived by performing experiments on well-characterized fluids such as a low viscosity standard Newtonian oil (Cannon Oils, State College, PA) and polydimethylsiloxane (PDMS) putty. Briefly, stepped flow tests with

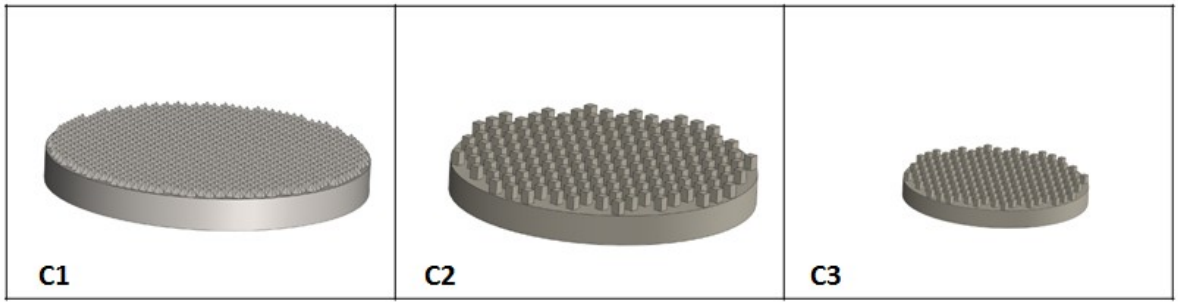

Figure 36: Various plate geometries were used to reduce wall slip between sample and rheometer. C1) Cleat geometry sold commercially by TA Instruments: 90^{o} x 0.5mm deep, apex to apex, steel. C2) Custom built geometry for large samples: 0.6 x0.6 x0.9mm (LxWxH) 20 mm and 24 mm diameter ABS. C3) Custom built geometry for small samples; 0.6 x0.6 x0.9mm (LxWxH) 13.70mm diameter ABS.

shear rates sweeping from 1-80 s^{-1} were conducted on the standard oil to determine the viscosity. Four gap heights (500 µm, 1000 µm, 1500 µm, and 2000 µm) were tested on three geometries (smooth, C1, and C2) at 22 ^{o}C. The C3 geometry had identical cleat dimensions as C2 thus calculation of the effective gap height was not repeated for C3.

Standard oil is not prone to wall slip effects, so viscosity measured with the smooth parallel plate geometry established was identified as the true viscosity (η_{true}) and viscosity measured with the cleated geometries was defined as the measured viscosity (η_{meas}). The effective gap correction factor, δ, was found by performing a nonlinear least-squares fitting of Eq. [2] for each geometry.

$$\frac{\eta_{meas}}{\eta_{true}} = \frac{gap_{meas}}{(gap_{meas} + \delta)} \qquad [2]$$

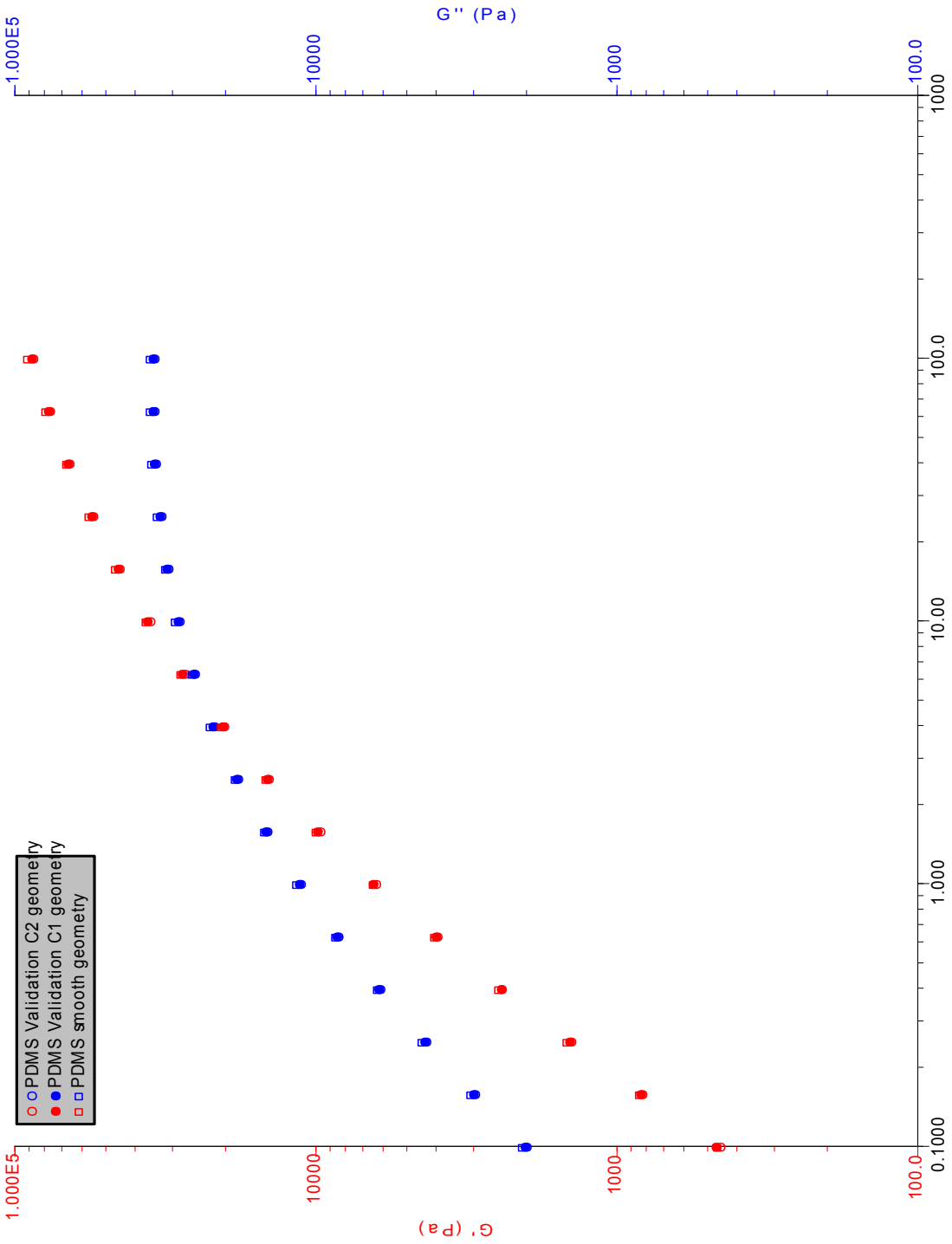

Figure 37: PDMS validation with cleat geometries C1, C2, and smooth. Gap correction factors: C1=325µm, C2=393 µm.

Gap correction values are independent of the materials tested [33], so the gap correction factors and effective gap heights ($gap_{meas} + \delta$) were validated by performing frequency tests from 0.1-100 rad/s of PDMS putty in the linear viscoelastic region (1% strain).

The true viscoelastic moduli (smooth geometry) of the PDMS were higher than the measured uncorrected viscoelastic moduli (slip suppressing geometries). By applying the gap correction factor post-hoc the viscoelastic moduli showed very good agreement (Fig. 37).

The depth of the no-slip boundary layer (δ) for our custom cleat design was 390 μm. This is much larger than the 157 μm depth of the no-slip boundary layer for the custom cleat design developed by Nickerson et al. for testing the dynamic properties of adult porcine vitreous [33]. Their optimal cleat design was 0.45 x 0.45 x 0.6 mm, and is much smaller than the dimensions of our cleat design. Their smaller design is likely due to differences in the manufacturing processes. They machined their cleat out of aluminum, while our custom cleat design was made from ABS plastic using 3-D printing (University of Utah BioDesign Lab). This resulted in a quick and inexpensive way to develop and test cleat geometries, but the actual dimensions of the cleat varied from what was specified for 3-D printing. As verified using a Contour K1 optical interferometer (Bruker, Tuscan, AZ), the geometries were circular (diameter = 0.75mm) rather than square (0.6mm x 0.6mm) in shape and the height for the 0.9mm design was actually 0.85mm (Fig. 38). Nickerson et al. did not perform optical measurements on their finalized cleat design, but it is likely that their tolerances may have been tighter because it

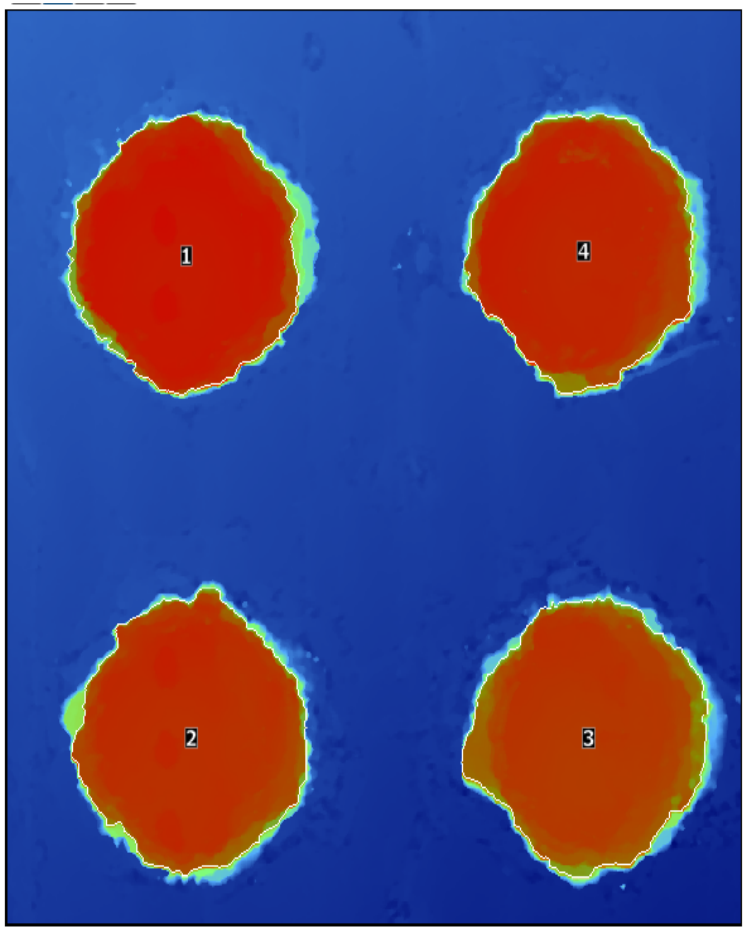

No	Region	Mean mm	Rp mm	X Diameter mm	Y Diameter mm	
1		0.77241	0.82859	0.78589	0.76794	
2		0.76314	0.82120	0.80024	0.78589	
3		0.75219	0.80620	0.83971	0.76435	
4		0.76325	0.81125	0.77871	0.76435	
Avg:		0.76275	0.81681	0.80114	0.77063	
Std:		0.00716	0.00868	0.02358	0.00893	
Skewness:		-0.18607	0.13512	0.81159	1.06595	
Max:		0.77241	0.82859	0.83971	0.78589	
Min:		0.75219	0.80620	0.77871	0.76435	
Range:		0.02022	0.02239	0.06100	0.02153	

Figure 38: Bruker Contour K1 optical interferometry data report.

was machined rather than printed. Despite these differences, the ABS cleat geometries were successful in preventing slip for immature vitreous [34].

Frequency-dependent sweeps from 0.1-100 rad/s without the cleat profile resulted in noisy data at low frequencies (0.1-1 rad/s). Wall slip was associated with these low frequency limitations and was mitigated using the new cleat designs.

APPENDIX B

INTERCONVERSION

Interconversion is a mathematically intensive process whereby an experimentally inaccessible material function such as the retardation spectrum or relaxation spectrum is derived from an experimentally accessible material function (creep compliance or oscillation test, respectively). To complete the interconversion there are two approaches. The discrete interconversion approach analytically evaluates a Voigt or Kelvin (Fig. 39) element's characteristic compliance J_k and timescale λ_k by fitting the experimental creep compliance data to Equation [3]. Due to this being an ill-posed mathematical process, small differences in experimental data can lead to large differences in the spectral result. This is counteracted by using nonlinear regularization procedures resulting in the determination of a discrete retardation spectrum with a "strength" J_k and location λ_k, where the location corresponds to the time required for the extension of the spring to its equilibrium length during retardation by a dashpot [35]. Conversion to the relaxation spectrum is an exact integral transformation resulting in the element's characteristic modulus, G_i and timescale τ_i [36] [36]. As shown in Equation 4, the relaxation modulus is easily defined from the relaxation spectrum. The corresponding dynamic functions, G' and G", are obtained by the Fourier transforms of Equation 4, resulting in Equation 5 and Equation 6.

$$J(t) = J_0 + \sum_{k=1}^{m} J_k \left[1 - e^{\left(-t/\lambda_k\right)}\right] + t/\eta_0 \quad [3]$$

$$G(t) = G_e + \sum_{i=1}^{n} G_i e^{\left(-t/\tau_i\right)} \quad [4]$$

$$G'(\omega) = G_e + \omega \int_0^{\infty} [G(t) - G_e] sin\omega t \, dt \quad [5]$$

$$G"(\omega) = \omega \int_0^{\infty} [G(t) - G_e] cos\omega t \, dt \quad [6]$$

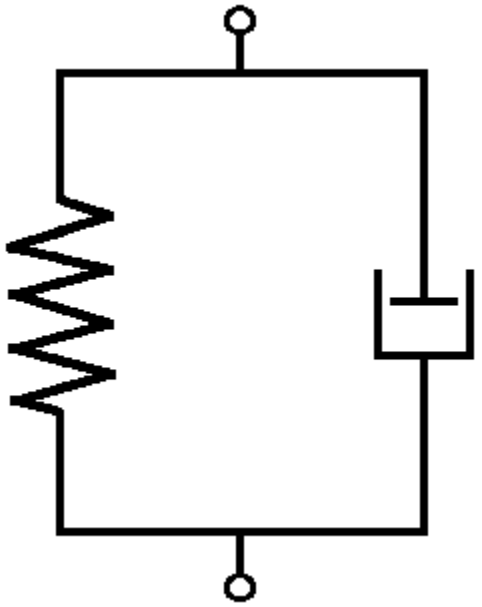

Figure 39: Voigt single element model.

An alternative approach is the continuous interconversion as shown in Equation 7, which uses numerical techniques to determine the spectra. This is a generalized discrete interconversion approach in that an infinite amount of elements instead of an exact integral are used to calculate the spectra. Once one spectrum is determined for the entire time scale, the corresponding spectra can be calculated. The interconversion between material spectral functions is not included, but a complete description can be found in [35].

$$J(t) = J_o + \int_{-\infty}^{\infty} L(\lambda)\left[1 - e^{-t/\lambda}\right] dln\lambda + \frac{t}{\eta_o} \quad [7]$$

$$G'(\omega) = \int_{-\infty}^{\infty} \frac{\omega^2\tau^2}{1+\omega^2\tau^2} H(\tau) dln\tau \quad [8]$$

$$G"(\omega) = \int_{-\infty}^{\infty} \frac{\omega\tau}{1+\omega^2\tau^2} H(\tau) dln\tau \quad [9]$$

For our analysis, we opted to use the discrete approach. The error associated with creep-ringing was reduced to make the interconversion more effective, but materials with an elastic dominant response still resulted in significant error for G″. This error was determined to be less pronounced when tanδ of the material was close to 1.

APPENDIX C

MATLAB CODE

ANALYZING INTERCONVERTED DATA

```
%Statistical Analysis of Porcine Eye
clear
clc
close all


%parameters
N = 6; df = 5; t = 2.571;
freq_interval = [0.01592; 0.02522; 0.03998; 0.06336; 0.1004; 0.1592; 0.2522;...
0.3998; 0.6336; 1.004];

%Load the creep data
creep10 =load('convert_eye_23_GA_discrete.txt'); creep11 =load('convert_eye_32_GA_discrete.txt');...
creep12 =load('convert_eye_39_GA_discrete_new.txt'); creep13
=load('convert_eye_47_GA_discrete_new.txt');...
creep14 =load('convert_eye_59_GA_discrete.txt'); creep15 =load('convert_eye_61_GA_discrete.txt');

freq1 = load('freq_eye_20_GA.txt'); freq2 = load('freq_eye_40_GA.txt');
%Organize G' and G" in terms of their discrete data points

%G' for creep data
c1 = [creep10(1,1), creep11(1,1), creep12(1,1), creep13(1,1), creep14(1,1), creep15(1,1)];
c2 = [creep10(2,1), creep11(2,1), creep12(2,1), creep13(2,1), creep14(2,1), creep15(2,1)];
c3 = [creep10(3,1), creep11(3,1), creep12(3,1), creep13(3,1), creep14(3,1), creep15(3,1)];
c4 = [creep10(4,1), creep11(4,1), creep12(4,1), creep13(4,1), creep14(4,1), creep15(4,1)];
c5 = [creep10(5,1), creep11(5,1), creep12(5,1), creep13(5,1), creep14(5,1), creep15(5,1)];
c6 = [creep10(6,1), creep11(6,1), creep12(6,1), creep13(6,1), creep14(6,1), creep15(6,1)];
c7 = [creep10(7,1), creep11(7,1), creep12(7,1), creep13(7,1), creep14(7,1), creep15(7,1)];
c8 = [creep10(8,1), creep11(8,1), creep12(8,1), creep13(8,1), creep14(8,1), creep15(8,1)];
c9 = [creep10(9,1), creep11(9,1), creep12(9,1), creep13(9,1), creep14(9,1), creep15(9,1)];
c10 = [creep10(10,1), creep11(10,1), creep12(10,1), creep13(10,1), creep14(10,1), creep15(10,1)];

%G" for creep data
c_1 = [creep10(1,2), creep11(1,2), creep12(1,2), creep13(1,2), creep14(1,2), creep15(1,2)];
c_2 = [creep10(2,2), creep11(2,2), creep12(2,2), creep13(2,2), creep14(2,2), creep15(2,2)];
c_3 = [creep10(3,2), creep11(3,2), creep12(3,2), creep13(3,2), creep14(3,2), creep15(3,2)];
c_4 = [creep10(4,2), creep11(4,2), creep12(4,2), creep13(4,2), creep14(4,2), creep15(4,2)];
c_5 = [creep10(5,2), creep11(5,2), creep12(5,2), creep13(5,2), creep14(5,2), creep15(5,2)];
c_6 = [creep10(6,2), creep11(6,2), creep12(6,2), creep13(6,2), creep14(6,2), creep15(6,2)];
c_7 = [creep10(7,2), creep11(7,2), creep12(7,2), creep13(7,2), creep14(7,2), creep15(7,2)];
c_8 = [creep10(8,2), creep11(8,2), creep12(8,2), creep13(8,2), creep14(8,2), creep15(8,2)];
c_9 = [creep10(9,2), creep11(9,2), creep12(9,2), creep13(9,2), creep14(9,2), creep15(9,2)];
c_10 = [creep10(10,2), creep11(10,2), creep12(10,2), creep13(10,2), creep14(10,2), creep15(10,2)];

%Find the Mean of each data point for G' and G"

%Mean of Creep G'
MGc = [mean(c1); mean(c2); mean(c3); mean(c4); mean(c5); mean(c6); mean(c7); ...
mean(c8); mean(c9); mean(c10)];
```

```
%Mean of Creep G"
MGGc = [mean(c_1); mean(c_2); mean(c_3); mean(c_4); mean(c_5); mean(c_6); ...
mean(c_7); mean(c_8); mean(c_9); mean(c_10)];


% %%

%est std. dev Y creep G'
stdY_Gc = [std(c1); std(c2); std(c3); std(c4); std(c5); std(c6); std(c7); ...
std(c8); std(c9); std(c10)];
%est std. dev Y creep G"
stdY_GGc = [std(c_1); std(c_2); std(c_3); std(c_4); std(c_5); std(c_6); std(c_7); ...
std(c_8); std(c_9); std(c_10)];

%est std. dev M creep G'
stdM_Gc = [stdY_Gc(1,1)/sqrt(N); stdY_Gc(2,1)/sqrt(N); stdY_Gc(3,1)/sqrt(N); stdY_Gc(4,1)/sqrt(N);
stdY_Gc(5,1)/sqrt(N); stdY_Gc(6,1)/sqrt(N); stdY_Gc(7,1)/sqrt(N); stdY_Gc(8,1)/sqrt(N);
stdY_Gc(9,1)/sqrt(N);...
stdY_Gc(10,1)/sqrt(N)];
%est std. dev M creep G"
stdM_GGc = [stdY_GGc(1,1)/sqrt(N); stdY_GGc(2,1)/sqrt(N); stdY_GGc(3,1)/sqrt(N);
stdY_GGc(4,1)/sqrt(N);
stdY_GGc(5,1)/sqrt(N); stdY_GGc(6,1)/sqrt(N); stdY_GGc(7,1)/sqrt(N); stdY_GGc(8,1)/sqrt(N);
stdY_GGc(9,1)/sqrt(N);...
stdY_GGc(10,1)/sqrt(N)];

%Plot the mean plus 2 std dev. (95% CI) from the mean for creep G' and G" data

size = 7;
e = stdY_Gc;
figure(1)
%Plot of 95% CI mean creep with oscillation data
loglog(freq_interval, MGc,'or',  'linewidth', 2)
hold on
plot(freq_interval(1:size), freq2(1:size,1), '*k','linewidth',4)
errorbar(freq_interval,MGc, e, 'r')
xlabel('frequency, [Hz]')
ylabel('G" [Pa]')
legend('Mean Interconverted G"', 'Oscillation G"')
title('Interconverted G" vs. Oscillation G"')

e = stdY_GGc;
figure(2)
%Plot of 95% CI mean creep with oscillation data
loglog(freq_interval, MGGc,'sqb', 'linewidth', 2)
hold on
plot(freq_interval(1:size), freq2(1:size,2), '*k','linewidth',4)
h = errorbar(freq_interval,MGGc, e, 'b')
xlabel('frequency, [Hz]')
ylabel('G" [Pa]')
legend('Mean Interconverted G"', 'Oscillation G"')
title('Interconverted G" vs. Oscillation G"')
```

IMAGE SEGMENTATION

```
clear
clc
close all

%Open the SEM image file;
image=imread('Helix_4week_Post_Temp_004.tif');

%Initialize the variables
col_count=0;
ret_count=0;
max=0;
min=255;
b=size(image,2);

%Crop the parameter bar from the bottom of images
image1(:,:)=image(1:833,1:b);
figure(1)
imshow(image1);
title('original image');

%Adjust the image to remove 10% of the brightest pixels
image1 =imadjust (image1, [0.0 0.9],[]);

%Determine max and min gray in image
for row = 1:size(image1,1)
   for col = 1:size(image1,2)
      if image1(row,col)>max
         max=image1(row,col);
      end
      if image1(row,col)<min
         min=image1(row,col);
      end
   end
end

%Set absolute threshold value
threshold=0.6*max;

%fully contrast the image
diff=double(max-min);
for row = 1:size(image1,1)
   for col = 1:size(image1,2)
      %normalize all pixels in image to 0-255 grayscale range
      image2(row,col)=(255/diff)*(image1(row,col)-min);
   end
end

%create all black and all white image, the white representing collagen
for row = 1:size(image2,1)
   for col = 1:size(image2,2)
      if image2(row,col)>threshold
```

```
            contrast_image(row,col)=255;
            col_count=col_count+1;
        else
            contrast_image(row,col)=0;
            ret_count=ret_count+1;
        end
    end
end

%Calculate the percent collagen
percent_col=(col_count/(col_count + ret_count))*100

%Plot images
figure(2)
imshow(image1);
title('adjusted image');

figure(3)
imshow(contrast_image);
title('cologen contrast');
```

CREEP RINGING AVERAGING

```
%Averaging Creep data Method for Vitreous

clear
clc
close all

%Load creep data with ringing included
creep62= load('creep_eye_62_GA.txt');

%Show the creep ringing
figure(1)
plot(creep62(:,2), creep62(:,1), 'ok')

%Access the structure. Specifically the DataIndex of all the Peaks and
%valleys of the ringing
k = 0;
for i = 1: 4 %Index changes depending on the number of peaks/valleys
   k = k + 1;
   y(k,1) = creep_peak(i).DataIndex;
   z(k,1) = creep_valley(i).DataIndex;
end

%Find the compliance values and respective times for the peaks "x" and
%valleys "z"
x = creep62(y,:);
w = creep62(z,:);

%Average the peaks and valley compliance values and times
u = 0;
for j = 1: 4 % the data index "4" indicates there were 4 peaks & 4 valleys
   u = u + 1;
   c_t_avg(u,1) = (x(j,1) + w(j,1))./2;
   c_t_avg(u,2) = (x(j,2) + w(j,2))./2;
end

%Plot the resulting non-ringing data region
figure(2)
plot(c_t_avg(:,2), c_t_avg(:,1), 'k')
```

GAP CORRECTIONS

```
%Curve fitting the viscosity data to find delta
%09/29/11

close
clc
clear

%Average viscosities of the 3 different geometry types at 4 different gaps
cross = [0.677; 0.733; 0.765; 0.818]; %cross-hatch geometry
cleat6 = [0.671; 0.719; 0.806; 0.768]; %cleat geometry (0.6 x0.45 x 0.45)
cleat9 = [0.707; 0.659; 0.728; 0.733]; %cleat geometry (0.9 x0.6 x 0.6)
cleat6_1 = [0.653; 0.758; 0.812; 0.93]; %cleat geometry (0.6 x0.6 x0.6)

%Measured gap separation for each test
gap = [500; 1000; 1500; 2000];

%Initial guess
delta0 = [0.1];
options = optimset('Display','iter','MaxFunEvals',2000,'MaxIter',500,'LargeScale','off');

%Solve for the variable...delta = gap heigth adjustment
delta(1) = lsqcurvefit(@myfun,delta0,gap,cross) %delta for x-hatch
delta(2) = lsqcurvefit(@myfun,delta0,gap,cleat6)%delta for 0.6mm cleat
delta(3) = lsqcurvefit(@myfun,delta0,gap,cleat9)%delta for 0.9mm cleat
delta(4) = lsqcurvefit(@myfun,delta0,gap,cleat6_1)%delta for the 0.6 x 0.6 mm cleat

%Plot the viscosity ratio vs. the gap measured
figure(1)
x_hatch_geom = myfun(delta(1),gap);
cleat_geom1 = myfun(delta(2),gap);
cleat_geom2 = myfun(delta(3),gap);
cleat_geom3 = myfun(delta(4),gap);
hold on
grid on

%Plot the relation between gap and the output of the myfun function (i.e.
%n_meas/n_true)
plot(gap,x_hatch_geom,'bl','linewidth',1)
%plot(gap,cleat_geom1,'r','linewidth',2)
plot(gap,cleat_geom2,'g','linewidth',3)
%plot(gap,cleat_geom3,'k','linewidth',2)
legend('C1 geometry','C2 geometry')
xlabel('gap [µm]')
ylabel('\eta_m_e_a_s / \eta_t_r_u_e')
title('Gap correction factors')
```

CALCULATING AND COMPARING TANδ

```
%Tandelta Analysis of Porcine Eyes

close
clear
clc

%parameters
N = 6; df = 5; t = 2.571;
freq_interval = [0.01592; 0.02522; 0.03998; 0.06336; 0.1004; 0.1592; 0.2522];

%Load the creep data
%5-day
creep10 =load('freq_eye_37_GA.txt'); creep11 =load('freq_eye_44_GA.txt');...
creep12 =load('freq_eye_46_GA.txt'); creep13 =load('freq_eye_62_GA.txt');...
creep14 =load('freq_eye_63_GA.txt'); creep15 =load('freq_eye_65_GA.txt');

%4-week
creep16 =load('freq_eye_23_GA.txt'); creep17 =load('freq_eye_32_GA.txt');...
creep18 =load('freq_eye_39_GA.txt'); creep19 =load('freq_eye_47_GA.txt');...
creep20 =load('freq_eye_59_GA.txt'); creep21 =load('freq_eye_61_GA.txt');

%2-month
creep22 =load('freq_eye_50_GA.txt'); creep23 =load('freq_eye_51_GA.txt');...
creep24 =load('freq_eye_52_GA.txt'); creep25 =load('freq_eye_55_GA.txt');...
creep26 =load('freq_eye_56_GA.txt');
%Organize G' and G" in terms of their discrete data points

%G' for creep data
%5-day
c1 = [creep10(1,1), creep11(1,1), creep12(1,1), creep13(1,1), creep14(1,1), creep15(1,1)];
c2 = [creep10(2,1), creep11(2,1), creep12(2,1), creep13(2,1), creep14(2,1), creep15(2,1)];
c3 = [creep10(3,1), creep11(3,1), creep12(3,1), creep13(3,1), creep14(3,1), creep15(3,1)];
c4 = [creep10(4,1), creep11(4,1), creep12(4,1), creep13(4,1), creep14(4,1), creep15(4,1)];
c5 = [creep10(5,1), creep11(5,1), creep12(5,1), creep13(5,1), creep14(5,1), creep15(5,1)];
c6 = [creep10(6,1), creep11(6,1), creep12(6,1), creep13(6,1), creep14(6,1), creep15(6,1)];
c7 = [creep10(7,1), creep11(7,1), creep12(7,1), creep13(7,1), creep14(7,1), creep15(7,1)];


%4-week
c01 = [creep16(1,1), creep17(1,1), creep18(1,1), creep19(1,1), creep20(1,1), creep21(1,1)];
c02 = [creep16(2,1), creep17(2,1), creep18(2,1), creep19(2,1), creep20(2,1), creep21(2,1)];
c03 = [creep16(3,1), creep17(3,1), creep18(3,1), creep19(3,1), creep20(3,1), creep21(3,1)];
c04 = [creep16(4,1), creep17(4,1), creep18(4,1), creep19(4,1), creep20(4,1), creep21(4,1)];
c05 = [creep16(5,1), creep17(5,1), creep18(5,1), creep19(5,1), creep20(5,1), creep21(5,1)];
c06 = [creep16(6,1), creep17(6,1), creep18(6,1), creep19(6,1), creep20(6,1), creep21(6,1)];
c07 = [creep16(7,1), creep17(7,1), creep18(7,1), creep19(7,1), creep20(7,1), creep21(7,1)];

%2-month
c001 = [creep22(1,1), creep23(1,1), creep24(1,1), creep25(1,1), creep26(1,1)];
c002 = [creep22(2,1), creep23(2,1), creep24(2,1), creep25(2,1), creep26(2,1)];
c003 = [creep22(3,1), creep23(3,1), creep24(3,1), creep25(3,1), creep26(3,1)];
c004 = [creep22(4,1), creep23(4,1), creep24(4,1), creep25(4,1), creep26(4,1)];
```

```
c005 = [creep22(5,1), creep23(5,1), creep24(5,1), creep25(5,1), creep26(5,1)];
c006 = [creep22(6,1), creep23(6,1), creep24(6,1), creep25(6,1), creep26(6,1)];
c007 = [creep22(7,1), creep23(7,1), creep24(7,1), creep25(7,1), creep26(7,1)];


%G" for creep data
%5-day
c_1 = [creep10(1,2), creep11(1,2), creep12(1,2), creep13(1,2), creep14(1,2), creep15(1,2)];
c_2 = [creep10(2,2), creep11(2,2), creep12(2,2), creep13(2,2), creep14(2,2), creep15(2,2)];
c_3 = [creep10(3,2), creep11(3,2), creep12(3,2), creep13(3,2), creep14(3,2), creep15(3,2)];
c_4 = [creep10(4,2), creep11(4,2), creep12(4,2), creep13(4,2), creep14(4,2), creep15(4,2)];
c_5 = [creep10(5,2), creep11(5,2), creep12(5,2), creep13(5,2), creep14(5,2), creep15(5,2)];
c_6 = [creep10(6,2), creep11(6,2), creep12(6,2), creep13(6,2), creep14(6,2), creep15(6,2)];
c_7 = [creep10(7,2), creep11(7,2), creep12(7,2), creep13(7,2), creep14(7,2), creep15(7,2)];


%4week
c_01 = [creep16(1,2), creep17(1,2), creep18(1,2), creep19(1,2), creep20(1,2), creep21(1,2)];
c_02 = [creep16(2,2), creep17(2,2), creep18(2,2), creep19(2,2), creep20(2,2), creep21(2,2)];
c_03 = [creep16(3,2), creep17(3,2), creep18(3,2), creep19(3,2), creep20(3,2), creep21(3,2)];
c_04 = [creep16(4,2), creep17(4,2), creep18(4,2), creep19(4,2), creep20(4,2), creep21(4,2)];
c_05 = [creep16(5,2), creep17(5,2), creep18(5,2), creep19(5,2), creep20(5,2), creep21(5,2)];
c_06 = [creep16(6,2), creep17(6,2), creep18(6,2), creep19(6,2), creep20(6,2), creep21(6,2)];
c_07 = [creep16(7,2), creep17(7,2), creep18(7,2), creep19(7,2), creep20(7,2), creep21(7,2)];


%2-month
c_001 = [creep22(1,2), creep23(1,2), creep24(1,2), creep25(1,2), creep26(1,2)];
c_002 = [creep22(2,2), creep23(2,2), creep24(2,2), creep25(2,2), creep26(2,2)];
c_003 = [creep22(3,2), creep23(3,2), creep24(3,2), creep25(3,2), creep26(3,2)];
c_004 = [creep22(4,2), creep23(4,2), creep24(4,2), creep25(4,2), creep26(4,2)];
c_005 = [creep22(5,2), creep23(5,2), creep24(5,2), creep25(5,2), creep26(5,2)];
c_006 = [creep22(6,2), creep23(6,2), creep24(6,2), creep25(6,2), creep26(6,2)];
c_007 = [creep22(7,2), creep23(7,2), creep24(7,2), creep25(7,2), creep26(7,2)];


%Find the Mean of each data point for G' and G"

%Mean of Creep G' 5-day
MGc = [mean(c1); mean(c2); mean(c3); mean(c4); mean(c5); mean(c6); mean(c7)];
%Mean of Creep G' 4-week
MGc0 = [mean(c01); mean(c02); mean(c03); mean(c04); mean(c05); mean(c06); mean(c07)];
%Mean of Creep G' 2-month
MGc00 = [mean(c001); mean(c002); mean(c003); mean(c004); mean(c005); mean(c006); mean(c007)];

%Mean of Creep G" 5-day
MGGc = [mean(c_1); mean(c_2); mean(c_3); mean(c_4); mean(c_5); mean(c_6); ...
mean(c_7)];
%Mean of Creep G" 4-week
MGGc0 = [mean(c_01); mean(c_02); mean(c_03); mean(c_04); mean(c_05); mean(c_06); ...
mean(c_07)];
%Mean of Creep G" 4-week
MGGc00 = [mean(c_001); mean(c_002); mean(c_003); mean(c_004); mean(c_005); mean(c_006); ...
mean(c_007)];
```

```
%Calculate the Tandelta at each frequency
tandelt_5day = MGGc./MGc;
tandelt_4week = MGGc0./MGc0;
tandelt_2month = MGGc00./MGc00;

%Average the Tandeltas
avg_tandelt_5d = mean(tandelt_5day)
avg_tandelt_4wk = mean (tandelt_4week)
avg_tandelt_2mo = mean (tandelt_2month)
```

APPENDIX D

DATA FOR CHAPTER 1

Table 6: Interconverted creep data for porcine vitreous

Porcine Eye Data						
	3-5-day		**4-week**		**2-month**	
freq	**G' [Pa]**	**G" [Pa]**	**G' [Pa]**	**G" [Pa]**	**G' [Pa]**	**G" [Pa]**
1	11.5	5.411	10.73	8.23	2.378	1.742
2	12.54	6.694	14.15	9.024	2.905	2.01
3	13.7	8.681	17.91	8.457	3.445	2.229
4	15.04	11.82	20.8	6.735	3.854	2.538
5	17.07	16.87	22.44	4.825	4.142	3.197
6	21.08	24.52	23.21	3.335	4.454	4.457
7	29.47	34.44	23.55	2.375	5.03	6.577
8	44.65	43.57	23.71	1.874	6.3	9.818
9	65.19	46.16	23.83	1.758	8.99	14.24
10	84.12	39.98	24	1.988	13.93	19.34
1	16.42	8.672	4.715	3.288	2.434	0.9788
2	17.85	10.49	5.548	3.567	2.497	1.187
3	20.4	13.85	6.151	4.049	2.58	1.641
4	25.36	18.1	6.579	5.131	2.752	2.424
5	33.44	21.16	7.062	7.201	3.146	3.642
6	42.84	20.6	7.992	10.69	3.998	5.362
7	50.27	16.79	10.12	16.08	5.6	7.452
8	54.57	12.27	14.9	23.54	7.966	9.582
9	56.68	8.734	24.45	31.75	10.73	11.78
10	57.8	6.519	39.45	36.8	13.97	14.66
1	42.16	20.6	3.245	1.451	2.155	1.018
2	46.16	27.2	3.448	1.601	2.559	1.105
3	54.32	36.87	3.642	2.037	3.008	1.034
4	69.27	46.64	3.974	2.847	3.35	0.8302
5	90.02	50.82	4.684	4.084	3.542	0.6138
6	109.8	46.85	6.147	5.629	3.634	0.4586
7	123.5	39.39	8.681	6.915	3.678	0.3804
8	131.9	33.99	11.9	7.064	3.71	0.3761
9	139	32.53	14.67	5.927	3.753	0.4428
10	148.3	33.51	16.36	4.307	3.835	0.5765
1	15	8.979	4.735	2.504	2.095	1.552
2	17.97	10.8	5.326	2.843	2.692	1.903
3	22.32	12.03	5.806	3.322	3.543	2.048
4	27.07	11.76	6.105	4.236	4.389	1.83
5	31.11	10.38	6.293	5.952	4.969	1.395
6	34.27	8.583	6.489	8.911	5.273	0.9736
7	36.59	6.592	6.86	13.76	5.411	0.6631

Table 6: Continued

Porcine Eye Data						
	3-5-day		**4-week**		**2-month**	
freq	**G' [Pa]**	**G" [Pa]**	**G' [Pa]**	**G" [Pa]**	**G' [Pa]**	**G" [Pa]**
8	38.03	4.688	7.723	21.47	5.474	0.4667
9	38.79	3.155	9.763	33.42	5.511	0.361
10	39.14	2.055	14.31	51.3	5.551	0.3227
1	14.95	5.042	7.793	4.612	1.782	1.571
2	15.31	6.295	9.066	5.07	2.121	1.623
3	15.94	8.822	10.21	5.545	2.329	1.867
4	17.35	12.99	10.98	6.478	2.498	2.439
5	20.48	19.07	11.49	8.482	2.727	3.474
6	26.8	26.76	12.02	12.19	3.155	5.157
7	37.84	34.34	13.02	18.41	4.058	7.732
8	53.56	38.22	15.34	28.28	5.977	11.35
9	69.95	35.39	20.75	43.03	9.627	15.72
10	81.89	27.73	32.54	63.01	15.28	20.03
1	20.13	15.6	6.602	5.953		
2	25.48	19.4	9.036	6.774		
3	33.85	22.09	11.95	6.654		
4	43.46	21.16	14.4	5.505		
5	50.98	16.99	15.89	4.016		
6	55.28	12.14	16.62	2.759		
7	57.3	8.255	16.94	1.895		
8	58.18	5.657	17.07	1.383		
9	58.57	4.141	17.14	1.153		
10	58.81	3.474	17.2	1.166		

Table 7: Force oscillation data from porcine vitreous

Porcine Eye Data				
	3-5-day		**4-week**	
freq	**G' [Pa]**	**G" [Pa]**	**G' [Pa]**	**G" [Pa]**
1	10.56	5.676	6.463	2.62
2	14.76	8.175	4.883	2.03
3	19.68	9.595	4.565	2.218
4	25.09	10.7	4.623	2.615
5	27.64	10.93	4.913	3.297
6	32.24	10.62	5.318	4.13
7	35.92	10.56	5.926	5.421
1			20.01	7.713
2			21.04	5.477
3			16.11	5.491
4			18.01	5.151
5			19.55	5.926
6			20.82	6.367
7			21.87	7.218

Table 8: Fresh vs. fixed interconversion comparison for sheep eyes

Sheep Eye Data				
	Fixed		Fresh	
freq	G' [Pa]	G" [Pa]	G' [Pa]	G" [Pa]
1	47.02	43.28	16.16	7.287
2	61.91	48	17.65	8.721
3	75.51	52.24	20.05	10.77
4	89.34	59.25	23.25	12.77
5	106.4	69.34	26.38	14.72
6	129.2	81	28.95	17.84
7	159.2	89.91	31.63	23.51
8	191.9	90.19	35.66	32.52
9	217.3	84.02	41.92	45.13
10	232.1	81.31	50.47	62.39
11	239.5	90.43	62.38	87.51
1	35.41	38.8		
2	48.82	46.08		
3	62.96	52.65		
4	78.63	60.37		
5	96.85	68.16		
6	114.9	75.73		
7	131.2	88.11		
8	150.4	111.5		
9	183	147.1		
10	241.5	185.6		
11	326.5	203.5		

Table 9: Forced oscillaiton and interconverted agarose data

Agarose				
	Forced Oscillation		Interconverted	
freq	G' [Pa]	G" [Pa]	G' [Pa]	G" [Pa]
1	1197	122.7	1218	100.6
2	1241	105.8	1244	99.41
3	1276	97.25	1270	103.9
4	1308	90.94	1304	111
5	1335	85.37	1344	111.1
6	1358	85.32	1381	101.6
7	1386	84.17	1408	90.38
8	1403	75.54	1431	83.72

Table 9: Continued

Agarose				
	Forced Oscillation		**Interconverted**	
freq	**G' [Pa]**	**G" [Pa]**	**G' [Pa]**	**G" [Pa]**
9	1431	74.45	1456	78.99
10	1450	75.57	1482	70.27
11	1470	77.82	1502	57.88
12	1493	78.39	1515	46.52
1	1103	84.02	1033	101.1
2	1133	80.08	1059	97.44
3	1159	77.56	1084	99.8
4	1184	75.03	1115	104.4
5	1206	73.26	1151	103.2
6	1228	71.1	1182	96.33
7	1247	68.99	1208	90.82
8	1267	67.33	1234	88.98
9	1286	65.88	1263	86.58
10	1305	64.7	1293	77.83
11	1325	65.32	1318	61.79
12	1344	67.44	1333	43.98
1	962.3	86.6	1224	106.2
2	1001	77.95	1250	103.8
3	1028	73.97	1277	107.8
4	1053	70.61	1311	112.8
5	1075	67.12	1348	112.7
6	1094	65.09	1383	109.3
7	1114	63.25	1417	105.2
8	1131	59.46	1450	98.05
9	1150	57.95	1478	88.1
10	1165	57.2	1503	78.47
11	1181	58.2	1526	69.39
12	1199	59.1	1547	57.68
1	1176	96.54	989.8	95.38
2	1208	97.08	1016	94.23
3	1236	95.31	1041	97.23
4	1264	92.33	1072	101.9
5	1289	90.57	1107	101.4
6	1313	91.75	1138	95.67
7	1337	89.16	1164	90.76
8	1357	81.97	1190	88.04
9	1377	83.46	1217	83.14
10	1400	80.47	1239	74.83

Table 9: Continued

Agarose				
	Forced Oscillation		**Interconverted**	
freq	**G' [Pa]**	**G" [Pa]**	**G' [Pa]**	**G" [Pa]**
11	1420	78.2	1253	69.02
12	1441	76.11	1260	72.36
1	1258	90.25	1083	120.5
2	1290	87.51	1114	115
3	1319	84.57	1143	117.4
4	1347	81.19	1178	124.7
5	1370	77.62	1222	126.3
6	1392	78.31	1262	118.9
7	1417	77.6	1295	111.3
8	1434	70.36	1326	108.5
9	1458	68.71	1362	104.7
10	1477	69.6	1399	91.82
11	1496	70.93	1426	71.48
12	1517	71.55	1443	50.77
1	985	92.67	994.7	83.79
2	1019	86.28	1018	83.25
3	1049	82.15	1041	85.71
4	1076	77.64	1067	91.56
5	1101	74.29	1100	93.77
6	1122	72.72	1131	87.71
7	1142	69.95	1156	78.65
8	1164	67.04	1175	72.7
9	1181	65.93	1194	69.76
10	1197	62.52	1213	68.05
11	1216	65.25	1230	68.69
12	1230	62.22	1250	71.93

Table 10: Forced oscillation and interconversion data for PS

Polystyrene-Toluene				
	Forced Oscillation		**Interconverted**	
freq	**G' [Pa]**	**G" [Pa]**	**G' [Pa]**	**G" [Pa]**
1	3413	1863	2369	1348
2	4102	2124	2698	1421
3	4645	2350	3019	1631
4	5389	2719	3470	1977
5	6146	3125	4113	2333

Table 10: Continued

Polystyrene-Toluene				
	Forced Oscillation		**Interconverted**	
freq	**G' [Pa]**	**G" [Pa]**	**G' [Pa]**	**G" [Pa]**
6	6951	3595	4834	2604
7	7938	4181	5510	2911
8	9358	5135	6225	3418
9	10660	5991	7132	4109
10	12180	7081	8194	4905
11	13880	8522	9295	5967
12	16700	10790	10550	7593
13	18970	12960	12220	10010
14	22760	16570	14750	13510
15	26240	20480	19170	18120
16	31770	26250	26790	22560
1	3051	1740	3262	1762
2	3698	1973	3845	1829
3	4356	2312	4318	1874
4	4889	2538	4729	2064
5	5815	3060	5225	2444
6	6615	3463	5888	2939
7	7522	3939	6680	3522
8	8599	4638	7631	4282
9	9802	5417	8877	5187
10	11460	6632	10350	6076
11	13110	7777	11720	7061
12	14370	9173	12840	8587
13	16740	11450	13630	11240
14	19630	14340	14100	15880
15	23370	18190	14330	23760
16	28560	23380	14430	36710
1	2894	1660	3568	1872
2	3519	1923	4105	2028
3	4136	2213	4619	2271
4	4692	2466	5242	2666
5	5464	2933	6071	3099
6	6249	3366	6987	3462
7	7189	3889	7842	3918
8	8235	4560	8778	4714
9	9650	5535	10120	5828
10	11050	6481	11950	6913
11	12690	7862	13800	7784

Table 10: Continued

Polystyrene-Toluene				
	Forced Oscillation		**Interconverted**	
freq	**G' [Pa]**	**G" [Pa]**	**G' [Pa]**	**G" [Pa]**
12	14570	9438	15130	8956
13	16960	11770	15850	11370
14	19750	14560	16200	15980
15	23360	18270	16390	23970
16	28430	23200	16580	37110
1	2925	1673	3916	2040
2	3486	1899	4471	2170
3	4119	2164	5000	2439
4	4697	2424	5675	2877
5	5411	2763	6571	3334
6	6209	3245	7536	3730
7	7183	3790	8458	4261
8	8151	4358	9519	5131
9	9138	5042	10980	6259
10	10510	6095	12810	7408
11	12140	7427	14690	8556
12	14090	9045	16240	10080
13	16460	11290	17220	12790
14	19360	13980	17720	17830
15	23100	17770	17940	26560
16	27040	22220	18030	40980
1	2568	1500	3353	1911
2	3142	1720	3970	2089
3	3708	1967	4536	2238
4	4263	2245	5071	2534
5	4912	2636	5759	3033
6	5615	3046	6732	3578
7	6493	3551	7847	3993
8	7470	4240	8870	4428
9	8470	4985	9881	5194
10	9823	5993	11170	6348
11	11590	7433	12750	7678
12	13590	9037	14210	9267
13	15600	11110	15170	11880
14	18350	13790	15710	16600
15	21800	17410	16040	24700
16	26310	22160	16300	37990
1	1763	1160	1996	1297

Table 10: Continued

Polystyrene-Toluene				
	Forced Oscillation		**Interconverted**	
freq	**G' [Pa]**	**G" [Pa]**	**G' [Pa]**	**G" [Pa]**
2	1969	1268	2386	1443
3	2229	1415	2764	1622
4	2546	1603	3198	1906
5	2931	1836	3771	2244
6	3404	2160	4429	2557
7	3970	2543	5069	2936
8	4636	3016	5779	3555
9	5421	3622	6783	4404
10	6377	4359	8127	5245
11	7443	5285	9474	5987
12	8806	6458	10470	7031
13	10410	7982	11060	9040
14	12410	9979	11390	12760
15	14850	12480	11600	19150
16	17870	15630	11880	29650

Table 11: Forced oscillation and interconversion data for Matrigel

Matrigel				
	Forced Oscillation		**Interconverted**	
freq	**G' [Pa]**	**G" [Pa]**	**G' [Pa]**	**G" [Pa]**
1	118.6	20.25	92.55	16.19
2	120.4	19.09	97.08	15.33
3	124.1	19.14	100.6	14.26
4	128.6	19.92	102.9	14.31
5	133.7	20.89	104.7	16.58
6	139.3	21.74	107	21.63
7	145.5	21.86	111.1	29.59
8	151.1	21.11	117.4	40.26
1	75.87	9.663	107.3	18.13
2	77.29	8.708	111.1	18.52
3	79	8.499	115.5	20.3
4	81.17	8.905	120.8	22.53
5	83.79	9.451	125.7	24.99
6	86.69	9.845	129	29.51
7	90.09	9.839	130.9	38.86
8	93.41	9.257	132.1	56.03
1	108.1	14.83	112.3	20.44
2	110.1	13.37	116.6	20.55
3	112.7	13.07	121.7	22.44
4	115.9	13.58	128.4	25.05
5	119.8	14.37	136.6	27.32
6	124.2	14.98	145.9	28.96
7	129.2	14.81	156.4	29.45
8	134	14.04	167.5	27.37
1	101.1	12.06	84.96	13.98
2	96.12	10.27	88.03	14.1
3	95.31	9.822	91.75	14.93
4	96.17	10.1	95.84	15.71
5	98.1	10.75	99.46	16.81
6	101.1	11.21	102.8	19.55
7	104.7	11.16	107.2	24.7
8	108.3	10.45	114.5	31.97
1	81.63	10.76	107.3	20.33
2	84.85	9.838	112.9	18.79

Table 11: Continued

Matrigel				
	Forced Oscillation		**Interconverted**	
freq	**G' [Pa]**	**G" [Pa]**	**G' [Pa]**	**G" [Pa]**
3	87.93	9.744	117	17.11
4	91.13	10.11	119.3	16.95
5	94.65	10.7	120.4	19.67
6	98.48	11.1	121	26.37
7	102.5	10.92	121.7	38.64
8	106.5	10.18	122.9	59.03
1	118.2	19.37	127.9	21.46
2	124.7	18.88	132.5	20.77
3	129.8	19.24	137.8	21.37
4	135.3	20.11	143.9	21.92
5	141.4	21.24	149.3	22.21
6	147.8	22.06	153.2	24.04
7	154.4	22.08	156.8	29.39
8	160.5	21.45	162.2	39.5

REFERENCES

[1] A. V. Levin, "Retinal Hemorrhage in Abusive Head Trauma," *Pediatrics,* vol. 126, 2010.

[2] J. D. Kivlin, K. B. Simons, S. Lazoritz and M. S. Ruttum, "Shaken Baby Syndrome," *Ophthalmology,* vol. 107, pp. 1246-1254, 2000.

[3] Y. Morad, Y. M. Kim, D. C. Armstrong, D. Huyer, M. Mian and A. V. Levin, "Correlation Between Retinal Abnormalities and Intracranial Abnormalities in the Shaken Baby Syndrome," *American Journal of Ophthalmology,* vol. 134, no. 3, pp. 345-359, 2002.

[4] C. S. Nickerson, J. Park, J. A. Kornfield and H. Karageozian, "Rheological properties of the vitreous and the role of hyaluronic acid," *Journal of Biomechanics,* vol. 41, pp. 1840-1846, 2008.

[5] P. Kashani-Sharif, J.-P. Hubschman, D. Sassoon and H. P. Kavehpour, "Rheology of the vitreous gel: Effects of macromolecule organization on the viscoelastic properties," *Journal of Biomechanics,* vol. 44, pp. 419-423, 2011.

[6] S. E. Parks, S. R. Kegler, J. L. Annest and J. A. Mercy, "Characteristics of fatal abusive head trauma among children in the USA: 2003-2007: an application of the CDC operational case definition to national vital statistics data," Group.bmj.com, Atlanta, 2011.

[7] B. Lee, M. Litt and G. Buchsbaum, "Rheology of the vitreous body. Part I: Viscoelasticity of Human Vitreous," *Biorheology,* vol. 29, pp. 521-533, 1992.

[8] B. Lee and G. Buchsbaum, "Rheology of the Vitreous Body: Part 3. Concentration of Electrolytes, Collagen and Hyaluronic Acid," *Biorheology,* vol. 31, no. 4, pp. 339-351, 1994.

[9] J. L. Denlinger, G. Eisner and E. A. Balazs, "Age-related Changes in the Vitreous and Lens of Rhesus Monkeys (Macaca mulatta)," *Experimental Eye Research,* vol. 31, pp. 67-79, 1980.

[10] J. Sebag, "Age-Related Differences in the Human Vitreoretinal Interface," *Arch Ophthalmol,* vol. 109, 1991.

[11] T. L. Ponsioen, M. J. A. van Luyn, R. J. van der Worp, J. C. van Meurs, J. M. M. Hooymans and L. I. Los, "Collagen Distribution in the Human Vitreoretinal Interface," *Investigative Ophthalmology and Visual Science,* vol. 49, no. 9, 2008.

[12] J. Prince, C. Diesem, I. Eglitis and G. Ruskell, "Anatomy and histology of the eye and orbit in domestic animals.," in *Functional anatomy and physiology of domestic animals*, Springfield, Charles C Thomas, 1960.

[13] C. Friedrich, J. Honerkamp and J. Weese, "New ill-posed problems in rheology," *Rheologica Acta,* vol. 35, pp. 186-193, 1996.

[14] R. H. Ewoldt and G. H. McKinley, "Creep Ringing in Rheometry or How to Deal with Oft-discarded Data in Step Stress Tests," *Rheology Bulletin,* vol. 76, no. 1, 2007.

[15] N. Y. Yao, R. J. Larsen and D. A. Weitz, "Probing nonlinear rheology with inertio-elastic oscillations," *Journal of Rheology,* vol. 52, no. 4, pp. 1013-1025, 2008.

[16] C. Baravian and D. Quemada, "Using Instrument inertia in controlled stress rheometry," *Rheologica Acta,* vol. 37, pp. 223-233, 1998.

[17] "Bad Science: Locking the Phase Angle," TA Instruments, [Online]. Available: www.nobadscience.com/rheo3. [Accessed 24 March 2011].

[18] U. Zolzer and H. F. Eicke, "Free oscillatory shear measurements-an intersting application of constant stress rheometers in the creep mode," *Rheologica Acta,* vol. 30, pp. 104-107, 1993.

[19] A. Gandorfer, E. Putz, U. Welge-LuBen, M. Gruterich, M. Ulbig and A. Kampik, "Ultrastructure of the vitreoretinal interface following plasmin assisted vitrectomy," *British Journal of Ophthalmology,* vol. 85, pp. 6-10, 2001.

[20] P. N. Bishop, D. F. Holmes, K. E. Kadler, D. McLeod and K. J. Bos, "Age-Related Changes on the Surface of Vitreous Collagen Fibers," *Investigative Ophthalmology,* vol. 45, pp. 1041-1046, 2004.

[21] L. I. Los, R. J. van der Worp, M. J. van Luyn and J. M. M. Hooymans, "Age-Related Liquefaction of the Human Vitreous Body: LM and TEM Evaluation of the Role of Proteoglycans and Collagen," *Investigative Ophthalmology and Visual Science,* vol. 44, no. 7, pp. 2828-2833, 2003.

[22] L. Botes, B. Price, M. Waldron and G. Pitcher, "A simple and rapid scanning electron microscope preparation technique for delicate "gymnodinioid" dinoflagellates.," *Microsc Res Tech,* pp. 128-30, 2002.

[23] D. Bray, J. Bagu and P. Koegler, "Comparison of hexamethlydisilazane (HMDS), Peldri II, and critical-point drying methods for scanning electron microscopy of biological specimens," *Microsc Res Tech,* vol. 26, no. 6, pp. 489-95, 1993.

[24] L. Muscariello, F. Rosso, G. Marino, A. Giordano, M. Barbarisis, G. Cariero and A. Barbarisis, "A critical overiew of ESEM applications in the biological field," *J Cell Phys,* vol. 205, pp. 328-34, 2005.

[25] D. Stokes, "Recent advances in electron imaging, image interpretation and applications: environmental scanning electron microscopy," *Philos T Roy Soc A,* vol. 361, pp. 2771-87, 2003.

[26] J. Sebag and E. A. Balazs, "Morphology and Ultrastructure of Human Vitreous Fibers," *Investigative Ophthalmology and Visual Science,* vol. 30, no. 8, pp. 1867-1871, 1989.

[27] J. Sebag and K. M. Yee, "Vitreous: From Biochemistry to Clinical Relevance," in *Duane's Clinical Ophthalmology*, Lippincott Williams and Wilkins.

[28] A. Gandorfer, S. Priglinger, K. Schebitz, J. Hoops, M. Ulbig, J. Ruckhofer, G. Grabner and A. Karnpik, "Vitreoretinal Morphology of Plasmin-Treated Human Eyes," *American Journal of Ophthalmology,* vol. 133, no. 1, pp. 156-158, 2002.

[29] J. Goldstein, D. Newbury, D. Joy, C. Lyman, P. Echlin, E. Lifshin, L. Sawyer and J. Michael, Scanning Electron Microscopy and X-Ray Microanalysis, vol. 3rd Edition, Springer.

[30] A. Biesemeier, U. Schraermeyer and O. Eibl, "Quantitative chemical analysis of ocular melanosomes in stained and non-stained tissues," *Micron,* vol. 42, pp. 461-470, 2001.

[31] R. Wadley, B. Junghans, M. Dickson and H. Liang, "A Quantitative Cryo-Scanning X-Ray Microanalysis Protocol for the Examination of the Eye," *Scanning,* vol. 24, no. 1, pp. 34-38, 2002.

[32] A. Biesmeier, U. Schraermeyer and O. Eibl, "Chemical composition of melanosomes, lipofuscin and melanolipofuscin granules of human RPE tissues," *Experimental Eye Research,* vol. 93, pp. 29-39, 2011.

[33] C. S. Nickerson and J. A. Kornfield, "A "cleat" geometry for suppressing wall slip," *Joural of Rheology,* vol. 49, no. 4, pp. 865-874, 2005.

[34] P. Moran and B. Coats, "Development of Rheometry Tools for Preventing Wall Slip in Immature Porcine Vitreous," in *Utah Biomedical Engineering Conference*, Salt Lake City, 2011.

[35] J. D. Ferry, Viscoelastic properties of polymers, New York: John Wiley and Sons, Inc., 1980.

[36] "Spectral Analysis and The Interconversion of Linear Viscoelastic Functions," TA Instruments, New Castle.

[37] A. V. Levin, "National Center on Shaken Baby Syndrome," 25 May 2006. [Online]. Available: www.dontshake.org/sbs. [Accessed 5 May 2012].

[38] S. Margulies, B. Coats, C. Christian, B. Forbes and A.-C. Duhaime, "What can we learn from computational model studies of the eye?," *Journal of AAPOS,* vol. 13, p. 332, 2009.

[39] N. Rangarajan, S. B. Kamalakkannan, V. Hasija, T. Shams, C. Jenny, I. Serbanescu, J. Ho, M. Rusinek and A. V. Levin, "Finite element model of ocular injury in abusive head trauma," *Jouranl of AAPOS,* vol. 13, pp. 364-369, 2009.

[40] J. Ruiz-Ederra, M. Garcia, M. Hernandez, H. Urcola, E. Hernandez-Barbachano, J. Araiz and E. Vecino, "The pig eye as a novel model of glaucoma," *Experimental Eye Research,* vol. 81, no. 5, pp. 561-569, 2005.

[41] P. Moran and B. Coats, "Biological Sample Preparation for SEM Imaging of Porcine Retina," *Microscopy Today,* vol. 20, no. 2, pp. 28-31, March 2012.